

GEOMETRY, TOPOLOGY AND CONTROL OF SPIN-1 QUANTUM SYSTEMS

A Dissertation
Presented to
The Academic Faculty

By

Bharath H. M.

In Partial Fulfillment
of the Requirements for the Degree
Doctor of Philosophy in the
School of Physics

Georgia Institute of Technology

December 2018

Copyright © Bharath H. M. 2018

GEOMETRY, TOPOLOGY AND CONTROL OF SPIN-1 QUANTUM SYSTEMS

Approved by:

Prof. Michael Chapman, Advisor
School of Mathematics
Georgia Institute of Technology

Prof. Brian Kennedy
School of Physics
Georgia Institute of Technology

Prof. John Etnyre
School of Mathematics
Georgia Institute of Technology

Prof. C. A. R. Sá de Melo
School of Physics
Georgia Institute of Technology

Prof. Colin Parker
School of Physics
Georgia Institute of Technology

Date Approved: August 29, 2018

Philosophy [Physics] is written in that great book which ever lies before our eyes — I mean the universe — but we cannot understand it if we do not first learn the language and grasp the symbols, in which it is written. This book is written in the mathematical language, and the symbols are triangles, circles and other geometrical figures, without whose help it is impossible to comprehend a single word of it; without which one wanders in vain through a dark labyrinth.

Galileo Galilei, in "The Assayer", 1623

To my parents, H. N. Madhusudhana and H. M. Bharathi.

ACKNOWLEDGEMENTS

With absolutely no background in experimental physics, I approached Prof. Michael Chapman at the end of my first semester of my graduate school at Georgia Institute of technology. Despite my lack of experience in experiments, Prof. Chapman gave me the opportunity to work at his laboratory and has been very supportive to me and my scientific career. I started working in the lab around May 2014. My first assignment was to translate an existing set of simulation codes into MATLAB. The senior members of the lab, Dr. Thai Hoang and Dr. Martin Anquez guided me through the many-body theory of the system we use at our lab and helped me develop the MATLAB code. Starting from basic tasks such as mode-locking a laser, replacing a laser diode, Thai, Martin and Bryce Robbins trained me to be able to run the complex experiment in the lab. I am grateful to all of them.

In the following year, I started learning about the electronics of a laser lock box, current and temperature controllers. Meanwhile, we decided to vent the vacuum chamber in the lab to replace a couple of lenses in the chamber. That was my first exposure to building a vacuum chamber. My colleagues Matthew Boguslawski (Matt), Bryce and Martin helped me learn the process of building a vacuum chamber, bit by bit. The rebuilding of the chamber took much longer than we expected due to technical problems. I worked all along with Matt, who had an enormous knowledge and experience in building such experimental systems. I am thankful to him for helping me learn some of these techniques. I attended my first conference, DAMOP 2015 during this time. The conference exposed me to the wide range of active research topics in the field and it created an urge in me to conduct a serious literature survey of a few research areas before deciding my thesis problem. I started with quantum metrology and many-body entanglement.

By the end of 2015, as a part of my literature survey, I came across the interesting set of papers on mixed state geometric phase by A. Uhlmann [1, 2, 3] . After a detailed study of the theory of geometric phases, I decided to develop an analogue of geometric

phases for spin-1 systems and observe it in our lab, as a part of my thesis. Meanwhile, I was also working towards a secondary Masters (M.S) in mathematics, by completing the necessary classes in the School of Mathematics. In the spring of 2016, Zixin Jiang, an undergraduate student at our lab, who is now a graduate student in Mathematics, insisted that I sign up for an algebraic topology class in the School of Mathematics. This class turned out to be surprisingly useful for my study of spin-1 geometric phases. In this class, I learned about the topology of projective spaces, in particular, the complex projective plane ($\mathbb{C}\mathbb{P}^2$) and the real projective plane ($\mathbb{R}\mathbb{P}^2$), which largely shaped my understanding of spin-1 quantum systems. With a rough idea of developing a theory of geometric phases for spin-1 systems, I approached Prof. John Etnyre of the School of Mathematics, who is an expert on low dimensional topology, for further insights into the topology of $\mathbb{C}\mathbb{P}^2$. Prof. Etnyre was very welcoming and very helpful. I am grateful to him for the discussions with him through which I developed an intuition for the topology of spin-1 systems and constructed a rigorous theory out of my rough idea of geometric phases in spin-1 systems.

Another person who played a major role in the development of my thesis work was Prof. T. A. B. Kennedy. Around this time, I was also studying symmetry breaking phase transitions in a BEC at our lab. Whenever I got stuck with the theoretical model of this system, I would not hesitate to walk up one floor and knock Prof. Kennedy's door to have a discussion. Prof. Kennedy has always been approachable and has helped me develop an understanding of our system at the fundamental level. I discussed the theory of geometric phases that I developed with Prof. Kennedy, and I am thankful to him for helping me conceive a realizable experiment corresponding to this theory.

By this time, I was nearing my thesis proposal deadline. With Prof. Chapman, Prof. Kennedy and Prof. Etnyre in my committee, I completed my thesis proposal in August 2016. The consistent encouragement and unbounded academic freedom given to me by Prof. Chapman enabled me to integrate theoretical physics and even mathematics into my thesis work. During this time, I stumbled upon an exciting connection between the problem

of many-body entanglement in a BEC and the *truncated moment problem* in convex geometry. Pursuing this idea, I met with Prof. Greg Blekherman at the School of Mathematics, who was an expert on convex geometry. Our discussions would later turn into a project, which became my Math M.S. thesis [4].

Meanwhile, I started writing a theory paper presenting my results on spin-1 geometric phases. I wanted to get a condensed matter theorists' perspective on my results and therefore, I approached Prof. Carlos Sá de Melo, School of Physics. Prof. Sá de Melo had the unique ability and insights to see the connection between seemingly unrelated ideas in physics. He was also a very friendly person and always eager to discuss Physics. Often, he would stop by our lab around 9:00 PM in the evening and we would discuss exciting physics and the possible experiments that we could do in our lab, along with a freshly brewed pot full of tea. We would call it a day and go home only after we realized that it is 1:30 AM in the night!

Towards the end of 2016, my advisor, Prof. Chapman, encouraged me to participate in the three-minute-thesis competition (3MT), where the challenge was to communicate my thesis work in three minutes to a non-expert audience. While preparing for 3MT, I learned the art of oral communication, and it changed the way I presented my work at conferences thereafter. I was fortunate to win prize money in 3MT, which I used to attend a conference. Prof. Chapman had the foresight that a 3MT is possibly a very good step in my professional development. I am thankful to him for encouraging me to participate in 3MT.

I completed writing my theoretical paper on geometric phases in early 2017. I am thankful to Prof. Kennedy for his diligent reading of my long manuscript and extensive feedback that made me learn the art of writing a paper. I submitted the paper to Journal of Mathematical Physics (JMP). This paper was resubmitted four times to the same journal before it was accepted and the process took 14 months [5]. It was due to Prof. Kennedy's careful guidance and Prof. Chapman's encouragement that I was able to fight through the series of negative reviews that the paper received, to eventually get it published. I

can confidently say that I learned the art of responding to critical reviews because of the enormous guidance and support provided by Prof. Kennedy during this process.

Meanwhile, my discussions with Prof. Sá de Melo started bearing its fruits — we decided on writing two papers, one on staircase phenomena in BECs [6] and another on generalized Skyrmions. My broad understanding of condensed matter physics is largely shaped through the discussions I had with Prof. Carlos.

In the lab, working along with Matt, we had rebuilt the BEC chamber. The process was very educative to me. I learned from Matt the techniques of building a magneto optical trap (MOT), the careful alignment required to load the MOT into an optical trap, the control of the optical trap depth to evaporate the dipole trap into BEC, etc. By March 2017, I had started working on my my thesis experiment. With the help of Matt and my advisor Prof. Chapman, I was able to obtain a first set of data by May 2017. Later, during the fall of 2017, I worked with Lin Xin, a new talented graduate student to obtain the necessary data for an experimental paper on the geometric phase that was introduced earlier in my theory paper. Another bright young graduate student in the lab is Maryrose Barrios. She entered the lab with a lot of prior experience in handling lasers and building MOTs. She is also a talented swimmer and plays water polo for the institute. Undergraduates Thomas Dellaert and Deniz Kurdak have displayed enormous potential, building new small atom and ion traps from the scratch.

I am also thankful to my thesis committee members, Prof. Brian Kennedy, Prof. John Etnyre, Prof. C. A. R. Sá de Melo and Prof. Colin Parker for taking the time to review this work and proving their valuable feedback. I am grateful my parents, H. N. Madhusudhana and H. M. Bharathi and my sister, H. M. Madhuri for their endless support to my endeavors in Physics and Mathematics.

Finally, I acknowledge support from the National Science Foundation through grant no. NSF PHYS1506294.

POSSIBILITY AND REALITY

(A Preface)

This thesis is awkwardly spread out over experimental physics, theoretical physics and mathematics. Some chapters can be considered as mathematics while other chapters are located in the other end of the spectrum — experimental physics. There is a fundamental difference of perspective between the two ends of the spectrum, which makes it hard to write such a thesis. In this preface, we attempt to describe this difference in perspective and hope that it will help readers who are experts in one extreme of the spectrum to be able to easily follow the parts of the thesis that lie in the other extreme.

Possibility and reality is a well known puzzle in philosophy. It deals with the definitions and relations between the *possible* and the *real*. It has been, and is an active area of research in philosophy. Mathematics and experimental physics, in general, do not agree on the definition of *the possible* — this is the difference of perspective that we address here. In mathematics, possible is anything that can be conceived without logical contradictions. In experimental physics, possible is anything that can be conceived without logical contradictions, and conforming to the known laws of physics. In other words, a possibility is something that can be turned into a reality. Theoretical physics appears to be split between the two perspectives, although it tends to side with mathematics for the most part. Before identifying the deep consequences of this difference, we provide a simple example.

The classic example, that puts this difference in the spotlight is the notion of *virtual displacement* in Lagrangian dynamics, in classical mechanics. It has the reputation of being an elusive concept among students, for reasons that are perhaps related to the conflict of the two perspectives mentioned above. The Lagrangian is a functional defined over the phase space coordinates and its integral along a path in the phase space is known as the action corresponding to the path. The notion of virtual displacement appears when we minimize the action among all paths connecting two fixed endpoints in the phase space. In mathematics,

this is done by the stationary conditions — the path that minimizes the action has the property that when it is perturbed, keeping the Lagrangian the same, it results in no first order correction to the action. This perturbation, in physics, is known as a *virtual displacement*. It is a mathematical possibility, and under no circumstance can it be a physical reality — the path of a physical system in the phase space can not be changed without changing the Lagrangian. In other words, because this perturbed path violates Newton’s laws it is not a possibility according to experimental physics. The name ‘*virtual displacement*’ is perhaps a representation of this problem, and possibly a consequence of a debate when the term was coined. There is no physical interpretation for the concept of virtual displacement, which is often a characteristic of ideas from mathematics. Mathematics studies the possibilities; experimental physics studies the reality.

One of the profound implications of this difference appears in the construction of sets. A set is often constructed by a collection of possibilities. For instance, ‘the set of all curves connecting point A to point B ’, can be a very complex object from the experimentalists’ perspective. In particular, if some of these curves do not correspond to a physical reality, this set doesn’t exist.

It is easier to follow this thesis, if the appropriate perspective on possibility and reality is taken in each chapter. For instance, chapter 4 is perhaps furthest on the mathematical side and here, the objects/situations considered do not necessarily correspond to physical realities. They are mathematical possibilities, i.e., *thinkable objects*. This chapter is best understood taking the mathematical perspective on the notion of a possibility. Chapter 5 is furthest on the experimental side. Here, statements made correspond to certain physically real systems, and may not in apply to a large class of mathematical possibilities that are not physical realities. This chapter is best understood from the perspective of experimental physics on possibility and reality.

TABLE OF CONTENTS

Acknowledgments	v
Possibility and Reality	ix
List of Tables	xv
List of Figures	xvi
Summary and Thesis Contributionxxiii
Chapter 1: Geometry of Spin-1 Quantum States	1
1.1 Geometric Representation of Spin-1 Quantum States	1
1.2 Pure States.	3
1.3 Relation to Majorana Constellation	6
Chapter 2: History of Geometric Phase	7
2.1 Geometric Phase	7
2.1.1 Berry's phase	7
2.1.2 General definition of geometric phase	9
2.2 Previous experiments measuring geometric phase	14
2.3 Recent developments: Fault tolerant quantum computation	15

Chapter 3: Our Geometric Phase	16
3.1 The Minimum Distance Principle	16
3.2 Definition of Geometric Phase	20
3.3 Interpretation: The generalized solid angle	22
3.3.1 What is “Holonomy”?	24
3.3.2 Holonomy of loops on \mathbb{RP}^2	26
3.3.3 Holonomy of open paths in \mathbb{RP}^2	27
 Chapter 4: The Mathematical Theory of Our Geometric Phase	 29
4.1 The Complex Projective Plane	29
4.2 Ehresmann Connection	30
4.3 Definition of Horizontal Lift And Geometric Phase	33
4.4 Interpretation of this geometric phase	36
4.5 Proofs of Theorem 1 and 2	39
4.5.1 Proof of theorem 1	45
4.5.2 Proof of Theorem 2	50
4.6 Generalized Solid Angle	52
 Chapter 5: Experimental System	 54
5.1 Our System and Hamiltonian	54
5.2 State Preparation and Stern-Gerlach Measurements	56
5.3 Controlling the Spin of Rubidium Atoms	57
5.3.1 Rotating the Spin Vector	57
5.3.2 Resizing the Spin Vector	62

5.3.3	Measuring the Larmor Rotation	62
5.4	Magnetic Field Measurements	63
5.4.1	Microwave Spectroscopy	65
Chapter 6:	Our Experiment	69
6.1	The Loops Induced in the Lab	69
6.2	Geometric Phase Shift and Amplitude Shift	72
6.3	The Experiment and Data	73
6.3.1	Geometric Phase Shift	74
6.3.2	Geometric Amplitude Shift	80
Chapter 7:	Arbitrary Control and Projection Valued Measurements of Spin-1 Systems	84
7.1	Lambda Transitions	84
7.2	Tripod Transition	88
7.3	Arbitrary Projection Valued Measurements	90
7.4	Single Shot Tomography	91
7.4.1	Protocol -1 : single shot tomography of nematic states.	92
7.4.2	Protocol-2 : single shot tomography of arbitrary states.	93
Chapter 8:	Staircase in a BEC	95
8.1	The One-axis Twisting Hamiltonian	96
8.1.1	Staircase in Magnetization and Entanglement Entropy	96
8.1.2	Experimental Considerations	99
8.1.3	Computing the Entanglement Entropy	102

8.2	Staircase in a ferromagnetic spin-1 BEC.	104
8.3	Staircase in an anti-ferromagnetic spin-1 BEC.	107
8.3.1	Computing the Matrix Element q_s	108
Chapter 9: Entanglement in a BEC		116
9.1	Many Body Entanglement	116
9.2	Truncated K-Moment Problem	117
9.2.1	An Example	118
9.3	The Problem Statement	120
Chapter 10: Conclusions and Outlook		122
10.1	Geometric Phase	122
10.1.1	A Conjecture	123
10.2	Arbitrary Control and PVM	123
10.2.1	Dressed Hamiltonians	123
10.2.2	Single shot tomography of reduced density matrices	124
10.3	Staircase Phenomena in a BEC	124
10.4	Many Body Entanglement	124
Appendix A: Some Formulae for Spin-1 Systems		126
A.1	Hermitian Matrices	126
A.2	Unitaries Generated by the Spin Operators	128
A.3	RF Spectrum	129
References		140

LIST OF TABLES

3.1	The minimum distance principle: Table shows the path length, total, dynamical and geometrical phase for the three ways of inducing the latitude shown in Fig. 3.1. The path length is least in ψ_c and this corresponds to the parallel transport.	18
-----	--	----

LIST OF FIGURES

1.1	Geometrical Representation: A spin-1 quantum state is uniquely represented by a point inside the Bloch sphere surrounded by an ellipsoid. The former represents the spin vector, $\vec{S} = (\langle S_x \rangle, \langle S_y \rangle, \langle S_z \rangle)$ and the latter represents the spin fluctuation tensor T	2
1.2	Pure States: The lengths of the ellipsoid's axes are constrained by the length of the spin vector. Explicitly, they are given by $\sqrt{1 - \vec{S} ^2}$ and $\sqrt{\frac{1 \pm \sqrt{1 - \vec{S} ^2}}{2}}$. For the three examples labeled 1, 2 & 3, the spin vectors $\vec{S}_{1,2,3}$ satisfy $0 < \vec{S}_1 < 1$, $ \vec{S}_2 = 1$ and $ \vec{S}_3 = 0$. The ellipsoid degenerates to a disk for the last two cases.	5
1.3	Majorana constellation: Three example states represented by the pair (\vec{S}, T) and by a pair of points (endpoints of the chord) on the Bloch spheres.	6
2.1	Elementary examples of geometric phase. (a) (Image from Wikipedia) shows the path of a Foucault pendulum and the arrows on the path represent the plane of oscillation of the pendulum. The angle α between the initial and the final planes of oscillation at point A is equal to the steradian angle enclosed inside the path. (b) shows a sphere of quantum spin eigenstates $ \hat{n}; m\rangle$ for fixed m . The red orbit is the path traversed by the states due to an adiabatic change in the applied magnetic field. The over all phase picked up by the quantum state is $e^{im\Omega}$, where Ω is the steradian angle enclosed inside the path (shaded region).	8
2.2	Fiber bundles and holonomy. (a) shows an elementary example of a fiber bundle (see main text). (b) shows a closed path (red circle) on the base space and its lift into the fiber bundle. The two endpoints of its lift lie on the same fiber and the difference between them is the holonomy element or the geometric phase of the closed path.	10

2.3	<p>Hopf fibration. (Image from Wikipedia, https://en.wikipedia.org/wiki/Hopf_fibration) For half integer spins, Berry's phase is a holonomy of the Hopf fibration. The left side shows a torus obtained after attaching a circle at each point on the equator of a sphere. The right side shows successive nested tori obtained by attaching circles at each point on successive latitudes of the sphere. Latitudes to the north of the equator produce bigger tori and latitudes to the south of the equator produce smaller tori. The tori fill up \mathbb{R}^3 space, but they also identify infinity as a single point, because, at the north pole, the latitude reduces to a point. Thus, all the the tori together form a 3-sphere (S^3).</p>	11
3.1	<p>Dynamical Phase: (a), (b) and (c) show three different ways of inducing a latitude in a spin-1/2 system. The magnetic field in each case is indicated by \vec{B}. While the geometric phase is the same for all three of them, the dynamical phase is different (see text).</p>	19
3.2	<p>Geometric Phases Carried by the Ellipsoid: (a) and (b) show the geometric phase carried by the ellipsoid when parallel transported along a non-singular and a singular loop inside the Bloch sphere respectively. In either of these cases, the final orientation of the ellipsoid is different from the initial orientation, due to an $SO(3)$ geometric phase. For singular loops, this geometric phase is non-Abelian.</p>	21
3.3	<p>Interpretation of Geometric Phases: (a) and (b) contrast non-singular and singular loops under a radial projection. The former has a continuous projection and a well defined solid angle, while the latter doesn't. This problem is resolved by defining a generalized solid angle for singular loops using a diametric projection, as illustrated by (c) and (d). (c) shows a surface obtained by sweeping a diameter along the loop. The solid angle enclosed by this surface is the generalized solid angle of the singular loop. This surface is indeed a loop in the space of diameters of a sphere, i.e., in a real projective plane (\mathbb{RP}^2). (d) shows a Boy's surface, a representation of the real projective plane, together with the loop projected on it. The generalized solid angle is equal to the holonomy of this loop.</p>	25

4.1	Liftable and unliftable loops.	(a) and (b) show liftable loops and (c) shows an unliftable loop. In all three loops, the red point represents the starting and the ending point (i.e., $\gamma(0)$ and $\gamma(1)$). For the loop in (a), $\gamma^{-1}(\vec{0}) = \{t\}$ for some $t \in (0, 1)$ and the loop is differentiable at that point. The loop in (b) has a kink at zero, but with a suitable choice of the starting and ending points, it is liftable. In particular, when the starting and the ending points are chosen at the center, i.e., $\gamma^{-1}(\vec{0}) = \{0, 1\}$, $\dot{\gamma}(0)$ and $\dot{\gamma}(1)$ are both well-defined and therefore, the loop is liftable. The loop in (c) has multiple kinks at the center. Six intermediate points between 0 & 1, with the following ordering: $0 < t_1 < t_2 < t_3 < t_4 < t_5 < t_6 < 1$ are indicated to guide the reader through the loop. There is no choice of the starting and the ending points such that it is liftable. $\gamma^{-1}(\vec{0})$ has two points other than 0 & 1 and the loop is not differentiable at either of these points. Therefore, this loop is not liftable.	36
4.2	The lens spaces $L(4, 1)$ and $L(2, 1)$.	$L(4, 1)$ is the space of all tangent lines to a sphere and $L(2, 1)$ is the space of all unit tangent vectors to a sphere. (a) shows the tangent line $\ell = (\hat{z}, \pm\hat{x}) \in L(4, 1)$, parallel to \hat{x} and touching the sphere at \hat{z} . (b) shows a unit tangent vector to a sphere $(\hat{z}, \hat{x}) \in L(2, 1)$ at \hat{z} parallel to \hat{x}	42
4.3	Parallel transport.	Horizontal lifts (i.e., parallel transports) are defined by minimizing the Fubini-Study metric on $\mathbb{C}\mathbb{P}^2$, which turns out to be equivalent to the intuitive notion of parallel transport similar to tangent vectors. Quantum state vectors can be represented by chords inside \mathbb{B} . The spin vector is given by the center of the chord. Corresponding to a change $d\vec{S}$ in the spin vector, the chords can be parallel transported. (a) shows the parallel transport of the chord when $d\vec{S}$ is parallel to \vec{S} . (b) shows parallel transport of the chord when $d\vec{S}$ is perpendicular to the chord and \vec{S} . (c) shows the parallel transport when $d\vec{S}$ is parallel to the chord.	48
4.4	Generalized solid angle:	(a) shows a singular loop γ_a (in blue) and the segments of its projection to S^2 , β_1 and β_2 (in black). (b) shows the projection of γ_a to $\mathbb{R}\mathbb{P}^2$, α . Every point in $\mathbb{R}\mathbb{P}^2$ is a diameter of S^2 and therefore, α is obtained by mapping every point on γ_a to the respective diameter of \mathbb{B} . The resulting cone is a loop in the space of diameters to S^2 , i.e., in $\mathbb{R}\mathbb{P}^2$. Thus, the cone represents α and the generalized solid angle of γ_a is indeed equal to the solid angle of the cone.	53
5.1	Stern-Gerlach Measurement:	An example image of the atoms after a Stern-Gerlach separation. For a system of N atoms in a state ψ and $\xi_0 = \langle 0 \psi\rangle$, $\xi_{\pm 1} = \langle \pm 1 \psi\rangle$, the atoms numbers are expected to be $N \xi_{\pm 1} ^2$ and $N \xi_0 ^2$	56

5.2	Breakdown of RWA: Owing to the small bias field, the Larmor rate is comparable to the RF rabi rate. In the rotating wave approximation is not valid in such a regime [80]. The above data shows an RF rabi under a broken RWA. The solid curve is a fit of the data to the exact solution of the Schrödinger equation, without using the RWA.	58
5.3	The “OD” system of coils: The two coils arranged in an OD format driven out of phase can produce a rotating magnetic field. The “O” coil produces a field parallel to its axis, and the straight part of the “D” coil produces a field in the orthogonal direction. When they are driven out of phase and the current amplitude is adjusted so as to produce fields of equal magnitude, the set up produces a rotating magnetic field.	59
5.4	RF Rabi from the OD coils: The Rabi oscillations induced by a rotating magnetic field produced by the OD coils at 20 mG ambient field. The red data set shows the population in $m = 0$ Zeeman sub level. The green and the blue data sets are the populations in the $m = \pm 1$ Zeeman sub levels. The two coils were driven at 15 kHz out of phase, with peak-to-peak amplitudes 5V and 3V respectively, so as to balance the amplitudes of the produced fields. The scale on the x-axis is μs	60
5.5	RF Spectrum: An experimentally obtained data set of the RF spectrum using the OD coils at an ambient field of 40 mG. The solid curve is the best fit. The fit parameters are indicated in the inset. The parameters are ω_0 (kHz), Ω (kHz), a background offset and T ($1/\pi$ ms) respectively.	61
5.6	Larmor Rotation: Four data sets obtained through a Ramsey sequence discussed above. The amplitude of the oscillation of $\langle S_z \rangle$ is related to the initial tilt angle. The data sets in the four different colors corresponds to four different tilt angles, $\theta = \pi/16, \pi/12, \pi/6$ and $\pi/4$	64
5.7	Microwave Spectra: A typical set of microwave spectra taken during a measurement of the z - component of the magnetic field. The four data sets correspond to four different values of v_z . The data is fit to Eq. 5.10 and the resonance peak is obtained.	67
5.8	Measuring the magnetic field: A typical data set of the resonance peaks for various values of v_z , obtained from the fits shown in Fig. 5.7. The solid curve is fit function of the form Eq. 5.11. The fit parameters are shown in the inset. The four parameters are $\alpha_z, B_z, -B_z/\alpha_z$ and $\sqrt{B_x^2 + B_y^2}$ in that order.	68

6.1	Singular Loops Induced in the Lab: (a) shows a set of loops that start and end at the center of the Bloch sphere. These are the loops we induce in the lab. (b) shows the orientations of an ellipsoid at the center before and after parallel transport along one of these loops. Note that the ellipsoid degenerates into a disk at the center of the Bloch sphere.	70
6.2	Amplitude and Phase Shifts: The blue curve shows the Larmor oscillation of $\langle S_x^2 \rangle$ (see Eq. 6.4), for some orientation of the disk. The red curve shows the Larmor oscillation of $\langle S_x^2 \rangle$, for the same disk, after being parallel transported along one of the loops that we induce. The change in the orientation of the disk (see Fig. 6.1(b)) manifests as a phase shift and an amplitude shift.	73
6.3	The Experimental Sequence: The system is prepared in the state $ 0\rangle$, represented by a disk sitting flat at the center of the Bloch sphere (1 in the above figure). We use an RF pulse to tilt the disk by a desired angle. Images 2 through 6 illustrate the induction of a loop using a sequence of RF and microwave pulses. Finally a measurement of S_x^2 is made using a combination of RF and Stern-Gerlach separation.	75
6.4	Geometric Phase Shift: $\phi = 0$	76
6.5	Geometric Phase Shift: $\phi = \frac{\pi}{6}$	76
6.6	Geometric Phase Shift: $\phi = \frac{\pi}{3}$	77
6.7	Geometric Phase Shift: $\phi = \frac{\pi}{2}$	77
6.8	Geometric Phase Shift: $\phi = \frac{2\pi}{3}$	78
6.9	Geometric Phase Shift: $\phi = \frac{5\pi}{6}$	78
6.10	Geometric Phase Shift: The geometric phase shift for different values of the coverage angle (ϕ). The continuous line shows the theoretical geometric phase shift, i.e., 2ϕ . The inset shows the loops corresponding to the different values of ϕ used in the experiment.	79
6.11	Geometric Amplitude Shift: $\theta_{tilt} = \pi/12$	80
6.12	Geometric Amplitude Shift: $\theta_{tilt} = \pi/6$	81
6.13	Geometric Amplitude Shift: $\theta_{tilt} = \pi/4$	81
6.14	Geometric Amplitude Shift: $\theta_{tilt} = \pi/3$	82

6.15	Geometric Amplitude Shift: $\theta_{tilt} = 5\pi/12$	82
6.16	Geometric Amplitude Shift: A comparison with theory of the experimentally observed geometric amplitude shifts. The theoretical value of this amplitude shift is $\frac{1}{2} \cos 2\theta_{tilt}$ (continuous curve). The triangular markers show the experimentally observed amplitude shifts for different tilt angles. The inset shows the geometric phase shifts for these five tilt angles and the continuous line shows the corresponding theoretical value, i.e., π . The bottom inset shows the disks (magnified) at the starting point with different tilt angles used in the experiment.	83
7.1	Lambda and tripod transitions: (a) shows the setting in a Λ transition and (b) shows the setting in a tripod transition.	86
8.1	Staircase in the one-axis twisting Hamiltonian: (a) Shows the ground state magnetization as a function of the strength of the applied field p for constant interaction χ in the one-axis twisting Hamiltonian $H = \chi S_z^2 - p S_z$, with (blue curve) and without (black curve) the perturbation ϵS_x . (b) Shows the corresponding ground state and the first excited state energies around the level crossings between $m = -1$ and $m = 0$, as well as $m = 0$ and $m = +1$. In the absence of the perturbation, there are true level crossings, but when the perturbation is added, gaps open and thereby smooth the staircase. The term ϵS_x is also responsible for changing the system's magnetization, which is otherwise conserved. (c) Shows the entanglement entropy of the local ground state as a function of the control parameter p/χ . The black curve shows the entanglement without the perturbation as written in Eq.8.1, while the blue curve shows the entanglement with the perturbation for $\frac{\epsilon}{\chi} = 0.02$	97
8.2	Adiabatic ramps: (a) shows a numerical solution for the magnetization an optimal adiabatic ramp that takes a total time of $T = 38\chi^{-1}$ (red curve), compared with the ground state magnetization (blue curve). Here, $c\epsilon = 0.12\chi$ and $\Gamma = 6$. (b) shows a numerical solution for the magnetization with $\Gamma = 31$, $c\epsilon = 0.12\chi$ and the resulting time is $T = 200\chi^{-1}$	100
8.3	Convexity of the energy: The minimum energy eigenvalue E_m of the ferromagnetic Hamiltonian $H = cS^2 + qQ_{zz} - pS_z$ is a convex function of the magnetization m . For the purpose of this illustration, we have used $N = 10$. The minima of these curves correspond to the ground state magnetization. Because p is the coefficient of a linear term in m , changing it has the effect of shifting the minimum. The four values of $p/ c $ have their minima are different values of m , leading to a staircase response of the ground state magnetization as $p/ c $ is changed.	114

8.4 **Staircase in the magnetization direction:** (a) shows the ground state magnetization vector of an anti-ferromagnetic condensate with Hamiltonian $H = cS^2 + pS_x + \alpha Q_{xz}$, for three different values of c with $N = 100$. The last term in the Hamiltonian induces the tilting of the magnetization vector by specific angles, depending on where the system is on the staircase. (b) shows the tilt angle for $N = 20$ as a function of c/p , a staircase, but in contrast with the previous examples, this time it is not only in the magnitude of magnetization, but also in the direction. The blue curve shows the smoothed staircase after adding an ϵQ_{xx} perturbation, with $\epsilon = 0.02p$. The inset shows the ground state entanglement entropy as a function of the control parameter. In both (a) and (b), $\alpha = 0.1p$ 115

SUMMARY AND THESIS CONTRIBUTION

The object of study in this thesis is a spin-1 quantum mechanical system. The experimental system we use is an ^{87}Rb Bose-Einstein Condensate (BEC). The results presented in this thesis can be divided into two categories — one corresponding to the physics of non-interacting spin-1 atoms and the other corresponding to interacting spin-1 atoms. The former includes the study of certain geometric and topological aspects of the phase space of spin-1 atoms and the latter includes study of collective properties of an interacting spin-1 many-body system such as entanglement and staircase response phenomena. In the following, we provide an outline of these results.

Non-interacting spin-1 atoms

The physics of a non-interacting spin-1 BEC is effectively the same as the physics of any general spin-1 quantum system. The phase space of a general spin-1 quantum system is a four dimensional compact manifold known as the complex projective plane ($\mathbb{C}\mathbb{P}^2$) and has a non-trivial topology. We study some of the physically observable consequences of the topological and geometrical properties of $\mathbb{C}\mathbb{P}^2$. In particular, we develop a geometric representation of spin-1 quantum states and use it to define and experimentally observe a variant of Berry's geometric phase. We also develop a technique of arbitrary control and arbitrary projection values measurements (PVMs) of spin-1 quantum states. We provide a summary of these two projects in the next two sections.

Geometric Representation and Geometric Phase

A spin-1/2 quantum state is uniquely represented, up to a global phase factor, by a point on the Bloch sphere. We develop an analogous geometric representation for spin-1 quantum states. We show that a spin-1 quantum state is uniquely represented by a point on or inside the Bloch sphere that represents the expectation value of its spin vector together with an ellipsoid representing the spin fluctuations. Using this representation, we develop a variant of Berry's geometric phase, defined for all loops on or *inside* the Bloch sphere.

We formulate this geometric phase as an $SO(3)$ operator that is picked up by the spin fluctuation tensor, when the spin vector is transported along the loop. We generalize the standard notion of solid angles to *generalized solid angles* to interpret this geometric phase. Finally, we use a coherent control of spin-1 BEC to observe this geometric phase. The details are covered in Chapters 1 – 6.

Arbitrary Control and PVM of Spin-1 Systems

In this work, we theoretically develop a technique to perform a high fidelity, arbitrary control operation and to make an arbitrary PVM on a spin-1 system. The set of control operations on a spin-1 system is represented by the group $SU(3)$. We show how the action of an arbitrary element $U \in SU(3)$ can be induced in the lab. A PVM is represented by a 3×3 projection operator Π . The extreme points in the space of PVMs are the 1-dimensional projections; they are represented by rank-1 projection operators Π . The space of rank-1 projection operators is $\mathbb{C}P^2$. We show how the measurement corresponding to an arbitrary rank-1 projection operator can be done in the laboratory. This technique can also be used to perform a *single shot tomography* on a spin-1 ultracold atomic system. These results are presented in Chapter 7.

Interacting Spin-1 Systems

The interaction in a ^{87}Rb comes from the s-wave scattering between pairs of atoms. This interaction results in interesting features such as many-body entanglement and staircase response functions. In this thesis, we theoretically study both of these phenomena. The next two sections summarize these results.

Staircase Response Functions in a Spin-1 BEC

When an observable parameter of a physical system responds discretely to continuous tuning of a control parameter, the relevant response function takes a staircase structure. A classic example of this phenomena is the integer quantum Hall effect, where the Hall conductivity of a two dimensional electron gas changes discretely in response to a continuous tuning of the applied magnetic field. We show that a similar phenomena appears in a

spin-1 BEC, where, the magnetization of the atoms changes discretely, both in its magnitude and direction, in response to a continuous change in the applied magnetic field or the atom density. Chapter 8 provides the details of this result.

Entanglement in a Spin-1 BEC

Evolution of a spin-1 BEC under an interacting Hamiltonian results in the generation of many-body entanglement. Demonstrating this entanglement and quantifying it through experimentally measured observables has remained an active area of research. In this work, we use techniques from convex algebraic geometry to develop entanglement criteria and entanglement measures, using a set of experimentally accessible observables of a BEC. This material is covered in detail in a separate thesis [4]; however, the basic idea is developed in Chapter 9.

CHAPTER 1

GEOMETRY OF SPIN-1 QUANTUM STATES

1.1 Geometric Representation of Spin-1 Quantum States

It is well known that a pure spin-1/2 quantum state can be represented uniquely up to an arbitrary global phase, by a point on the Bloch sphere [7], whose coordinates are also the expectation values of the spin operators of the state. Spin-1 quantum states, however, differ in two ways — the expectation value of the spin vector can be anywhere on or *inside* the Bloch sphere and the quantum state is not uniquely represented by the expectation value of the spin vector. That is, there are multiple quantum states that all share the same spin vector. This ambiguity can be broken by considering the second order spin moments that represent the uncertainties in the spin components, described by a rank-2 tensor known as the spin fluctuation tensor:

$$T = \begin{pmatrix} \langle S_x^2 \rangle - \langle S_x \rangle^2 & \frac{1}{2}\langle \{S_x, S_y\} \rangle - \langle S_x \rangle \langle S_y \rangle & \frac{1}{2}\langle \{S_x, S_z\} \rangle - \langle S_x \rangle \langle S_z \rangle \\ \frac{1}{2}\langle \{S_x, S_y\} \rangle - \langle S_x \rangle \langle S_y \rangle & \langle S_y^2 \rangle - \langle S_y \rangle^2 & \frac{1}{2}\langle \{S_z, S_y\} \rangle - \langle S_z \rangle \langle S_y \rangle \\ \frac{1}{2}\langle \{S_x, S_z\} \rangle - \langle S_x \rangle \langle S_z \rangle & \frac{1}{2}\langle \{S_z, S_y\} \rangle - \langle S_z \rangle \langle S_y \rangle & \langle S_z^2 \rangle - \langle S_z \rangle^2 \end{pmatrix} \quad (1.1)$$

Here, $\langle \cdot \rangle$ represents an expectation value and is for instance, given by $\langle S_x \rangle = \text{Tr}(\rho S_x)$ for a general mixed state ρ . And $\{ \cdot, \cdot \}$ represents an anticommutator. Geometrically, this tensor represents an ellipsoidal region of uncertainty around the spin vector. The lengths of the semimajor axes of the ellipsoid are given by the square roots of the eigenvalues of T and their orientation is given by the corresponding eigenvectors Fig. 1.1.

The expectation value of the spin vector, $\vec{S} = (\langle S_x \rangle, \langle S_y \rangle, \langle S_z \rangle)$, which we shall hereafter refer to as the spin vector, together with the spin fluctuation tensor T uniquely represent a general mixed spin-1 quantum state. This follows from the observation that in the set

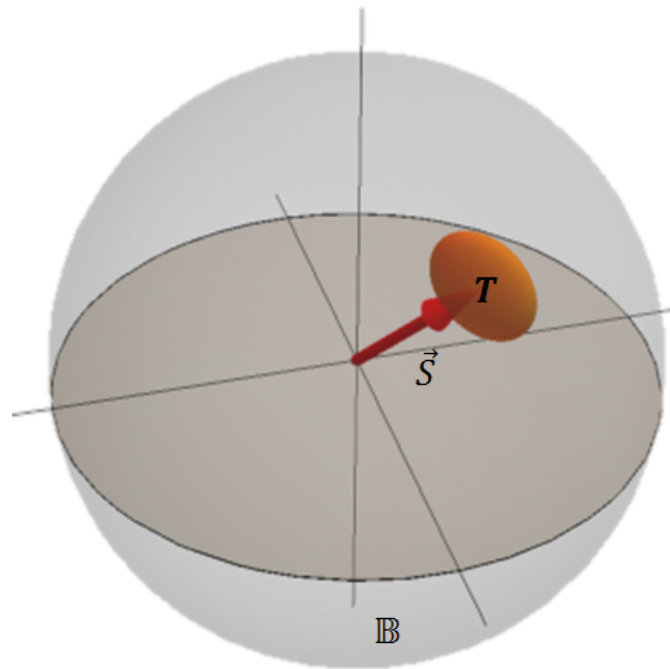


Figure 1.1: **Geometrical Representation:** A spin-1 quantum state is uniquely represented by a point inside the Bloch sphere surrounded by an ellipsoid. The former represents the spin vector, $\vec{S} = (\langle S_x \rangle, \langle S_y \rangle, \langle S_z \rangle)$ and the latter represents the spin fluctuation tensor T .

of ten operators $\{I, S_x, S_y, S_z, S_x^2, S_y^2, S_z^2, \{S_x, S_y\}, \{S_y, S_z\}, \{S_x, S_z\}\}$, nine are linearly independent and they span the nine dimensional vector space of 3×3 Hermitian matrices. Here, I is the identity matrix and $S_x^2 + S_y^2 + S_z^2 = 2I$. This is a convenient set of basis vectors, and an alternative to the Gell-Mann matrices. Therefore a general mixed state, represented by a 3×3 density matrix ρ , which is also Hermitian, can be represented by set of its inner products with these nine basis vectors, where, the innerproduct between two Hermitian matrices can be defined as the trace of their product. That is, ρ is represented by its coordinates $\{\text{Tr}(\rho), \text{Tr}(\rho S_x), \dots, \text{Tr}(\rho \{S_x, S_z\})\}$. The first component is normalized to unity, i.e., $\text{Tr}(\rho) = 1$ and the remaining eight are retrievable from the components of \vec{S} and T . Therefore, the pair (\vec{S}, T) uniquely represents a mixed spin-1 quantum state. Geometrically, spin-1 quantum states are uniquely represented up to an arbitrary global phase factor by a point inside the Bloch sphere surrounded by an ellipsoid. The former represents the spin vector and the latter represents the spin fluctuation tensor.

1.2 Pure States.

Hereafter, we restrict ourselves to pure spin-1 quantum states. The semimajor axes of the ellipsoid are constrained by the length of the spin vector, for pure states. In particular, the eigenvalues of T are given by $1 - |\vec{S}|^2$ and $\frac{1 \pm \sqrt{1 - |\vec{S}|^2}}{2}$. Therefore, the axes are given by $\sqrt{1 - |\vec{S}|^2}$ and $\sqrt{\frac{1 \pm \sqrt{1 - |\vec{S}|^2}}{2}}$.

It is straightforward to derive these expressions. The system has an $SO(3)$ symmetry, i.e., if $R \in SO(3)$ and $\mathcal{D}(R) \in SU(3)$ is its representation in $SU(3)$. Under the transformation of the quantum state vector ψ , $\psi \rightarrow \mathcal{D}(R)\psi$, the spin vector transforms as $\vec{S} \rightarrow R\vec{S}$ and the spin fluctuation tensor transforms as $T \rightarrow RTR^T$. Therefore, for the purpose of derivation of the eigenvalues of \mathbb{T} , without loss of generality we may assume that $\vec{S} = (0, 0, |\vec{S}|)^T$. Any normalized quantum state vector $\psi = (z_{-1}, z_0, z_{+1})^T$, (i.e.,

$\langle \psi, \psi \rangle = 1$) with this spin vector must satisfy:

$$\begin{aligned} z_{-1}z_0^* + z_0z_{+1}^* &= 0 \\ |z_{+1}|^2 - |z_{-1}|^2 &= |\vec{S}| \end{aligned} \quad (1.2)$$

When $0 < |\vec{S}| < 1$, the solutions to the above equation are

$$\psi = \begin{pmatrix} \sqrt{\frac{1-|\vec{S}|}{2}} e^{-i\theta} \\ 0 \\ \sqrt{\frac{1+|\vec{S}|}{2}} e^{i\theta} \end{pmatrix} \quad (1.3)$$

Each $\theta \in [0, \pi)$ produces a distinct quantum state with spin vector equal to \vec{S} . From Eq. 1.1, the corresponding spin fluctuation tensor can be computed:

$$T = \begin{pmatrix} \frac{1}{2} + \frac{\sqrt{1-|\vec{S}|^2}}{2} \cos 2\theta & \frac{\sqrt{1-|\vec{S}|^2}}{2} \sin 2\theta & 0 \\ \frac{\sqrt{1-|\vec{S}|^2}}{2} \sin 2\theta & \frac{1}{2} - \frac{\sqrt{1-|\vec{S}|^2}}{2} \cos 2\theta & 0 \\ 0 & 0 & 1 - |\vec{S}|^2 \end{pmatrix} \quad (1.4)$$

One of the eigenvectors of this matrix is $\vec{S} = (0, 0, |\vec{S}|)^T$ with an eigenvalue $1 - |\vec{S}|^2$. The other two eigenvalues are easily seen to be $\frac{1 \pm \sqrt{1-|\vec{S}|^2}}{2}$.

The eigenvector corresponding to $1 - |\vec{S}|^2$ is parallel to \vec{S} if $|\vec{S}| \neq 0$. Therefore, the ellipsoid has one degree of freedom — it can be rotated about \vec{S} , producing different quantum states with the same spin vector. There is a circle's worth of quantum states that all share a given spin vector. When $|\vec{S}| = 1$, i.e., for points on the surface of the Bloch sphere, the ellipsoid degenerates into a disk normal to \vec{S} , because the eigenvalue of T with eigenvector parallel to \vec{S} vanishes and the other two eigenvalues are equal. Therefore, there is a unique quantum state corresponding to every point on the surface of the Bloch sphere. Such states are the familiar *coherent states*. T is represented by a disk of radius $1/\sqrt{2}$ for such states. The set of all coherent states is a sphere.

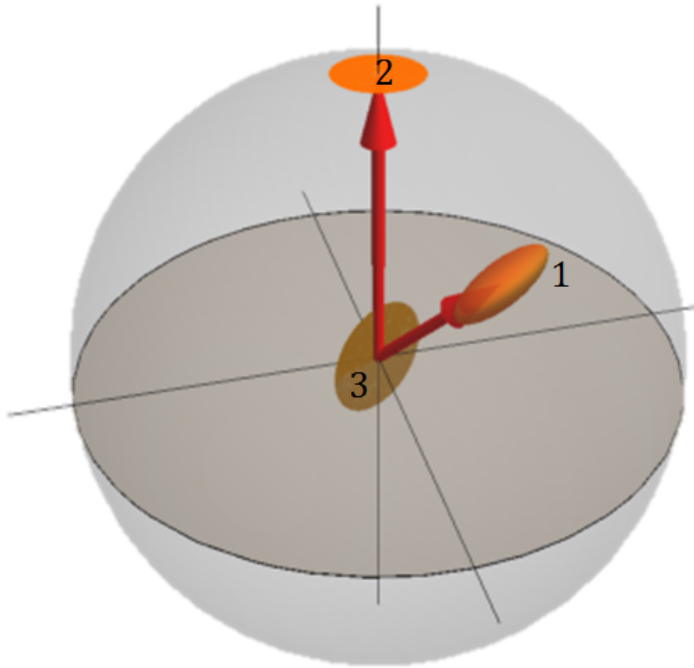


Figure 1.2: **Pure States:** The lengths of the ellipsoid's axes are constrained by the length of the spin vector. Explicitly, they are given by $\sqrt{1 - |\vec{S}|^2}$ and $\sqrt{\frac{1 \pm \sqrt{1 - |\vec{S}|^2}}{2}}$. For the three examples labeled 1, 2 & 3, the spin vectors $\vec{S}_{1,2,3}$ satisfy $0 < |\vec{S}_1| < 1$, $|\vec{S}_2| = 1$ and $|\vec{S}_3| = 0$. The ellipsoid degenerates to a disk for the last two cases.

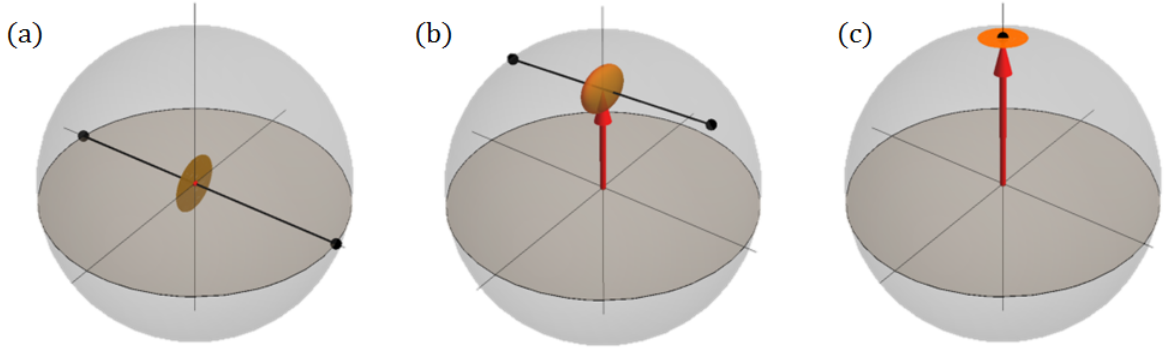


Figure 1.3: **Majorana constellation:** Three example states represented by the pair (\vec{S}, T) and by a pair of points (endpoints of the chord) on the Bloch spheres.

When $\vec{S} = 0$, again one of the eigenvalue of T is zero and the other two are equal to 1. Therefore, the ellipsoid degenerates into a disk of radius 1. Such states are known as *nematic states*, represented by a disk at the center of the Bloch sphere. The set of all nematic states is the so-called real projective plane ($\mathbb{R}\mathbb{P}^2$).

1.3 Relation to Majorana Constellation

An alternate geometric representation of spin-1 quantum systems is given by the Majorana constellation [8]. A spin-1 quantum state is uniquely represented by an unordered pair of points on the Bloch sphere. This comes from the observation that the symmetric (i.e., triplet) subspace of a pair of spin-1/2 systems is homomorphic to a spin-1 system.

A pair of points on the Bloch sphere is represented by a pair of unit vectors (\hat{r}_1, \hat{r}_2) . The corresponding spin vector is given by $\vec{S} = \frac{\hat{r}_1 + \hat{r}_2}{2}$. It is straightforward to check that the ellipsoid of quantum fluctuations is oriented such that its axes are parallel to $\hat{r}_1 + \hat{r}_2$, $\hat{r}_1 - \hat{r}_2$ and $\hat{r}_1 \times \hat{r}_2$. The smaller of the axes normal to the spin vector is parallel to $\hat{r}_1 - \hat{r}_2$ and we denote the corresponding unit vector by $\hat{u} = \frac{\hat{r}_1 - \hat{r}_2}{|\hat{r}_1 - \hat{r}_2|}$. While (\hat{r}_1, \hat{r}_2) can be considered as geometric coordinates for a spin-1 state, an equivalent set of coordinates are (\vec{S}, \hat{u}) . Note that (\vec{S}, \hat{u}) and $(\vec{S}, -\hat{u})$ represent the same state and therefore, we write $(\vec{S}, \pm\hat{u})$ (see Fig. 1.3).

CHAPTER 2

HISTORY OF GEOMETRIC PHASE

In this chapter, we provide an overview of the standard theory of geometric phases. This also includes some of the standard examples of geometric phases and previous experiments.

2.1 Geometric Phase

Consider a large Foucault pendulum transported adiabatically along a closed path on the surface of the earth. Although the final location of the pendulum is the same as the initial location, the corresponding planes of oscillations are found to be different (Figure 2.1(a)). The angle between these two planes is known as “geometric phase”, and is equal to the steradian angle enclosed by the path. Or, equivalently, it is the integrated curvature of the sphere inside the closed path. This is an example of a system retaining a memory of its past in a geometrical way.

An important observation is that the geometric phase depends on the gravitational field of the planet, which depends on the mass density of the planet’s interior. The steradian angle (or the integral of the curvature), however, is quite independent of the planet’s density. The equivalence of the geometric phase to the steradian angle holds only in a special case, where the density of the planet is spherically symmetric. In general, the geometric phase can be quite different from the steradian angle. This observation is crucial in giving a general definition to geometric phase. Let us consider a quantum mechanical example before taking up the general definition of geometric phase.

2.1.1 Berry’s phase

In this example, let us consider a quantum mechanical spin- S system. Let us denote the spin eigenstate with an eigenvalue m along a quantization axis \hat{n} by $|\hat{n}; m\rangle$. In this notation, the

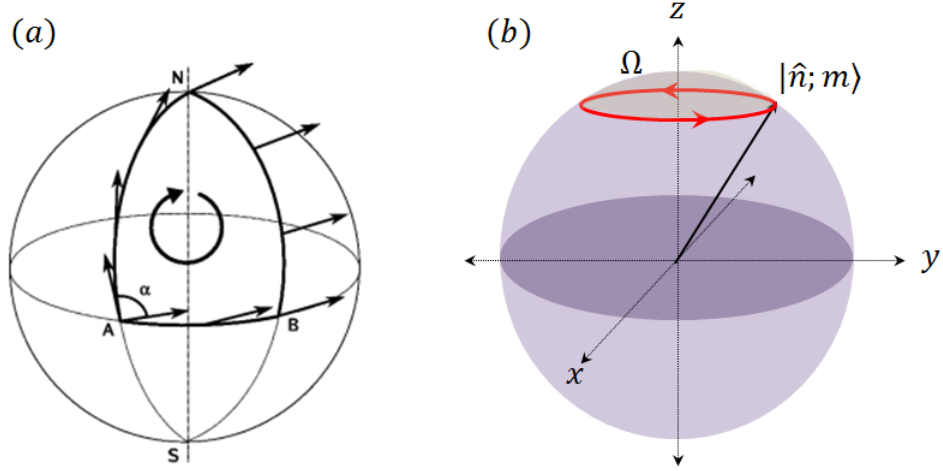


Figure 2.1: **Elementary examples of geometric phase.** (a) (Image from Wikipedia) shows the path of a Foucault pendulum and the arrows on the path represent the plane of oscillation of the pendulum. The angle α between the initial and the final planes of oscillation at point A is equal to the steradian angle enclosed inside the path. (b) shows a sphere of quantum spin eigenstates $|\hat{n}; m\rangle$ for fixed m . The red orbit is the path traversed by the states due to an adiabatic change in the applied magnetic field. The over all phase picked up by the quantum state is $e^{im\Omega}$, where Ω is the steradian angle enclosed inside the path (shaded region).

eigenstate of S_z with eigenvalue m will be written as $|\hat{z}; m\rangle$. m is in the range $-S \leq m \leq S$ and \hat{n} is a unit vector, represented by a point on the unit sphere. The space of all such states with a fixed eigenvalue $m (\neq 0)$ is also a sphere, if we ignore the overall phase factor of the quantum states. (That is, $e^{i\theta}|\hat{n}; m\rangle$ is same as $|\hat{n}; m\rangle$). The set of states with $m = 0$ is not a sphere; it has a more complicated topology and we discuss it in Section 3.

Such a system can be transported along a closed path on this sphere by adiabatically varying the direction of the applied magnetic field, B . The final state will be identical to the initial state, up to an overall phase factor (Figure 2.1(b)). That is, if the initial state is $|\hat{n}; m\rangle$, the final state will be $e^{i\theta}|\hat{n}; m\rangle$ where $\theta = \frac{m\mu_B BT}{\hbar} + m\Omega$ where T is the total time taken for the transport and Ω is the steradian angle enclosed by the path [9]. The first part of θ is the dynamical phase, which records the time taken for the adiabatic transport and the second part is the geometrical phase.

2.1.2 General definition of geometric phase

In the previous example, the equivalence of Berry's phase to the steradian angle is a coincidence; it owes to the fact that the dynamics of the phase factor, given by the Schrödinger equation, coincides exactly with the *connection form* on a sphere [10]. The general definition of geometric phase is based on this observation. We briefly discuss the notions of *fiber bundles* and connection forms before giving a general definition of geometric phase.

Let us consider a space \mathbf{B} of quantum states of a system. This could be the full Hilbert space or a relevant subspace of the Hilbert space, like the set of ground states of a family of Hamiltonians. Together with \mathbf{B} , let us also consider a group of gauge transformations acting on these states. A gauge transformation is a mathematical transformation of the quantum state which maintains all physical properties of the system invariant. Therefore, the group of gauge transformations generate a class of physically equivalent quantum states. For example, multiplying a quantum state by an overall phase factor is a gauge transformation with a gauge group $U(1)$.

A gauge transformation acting on the set \mathbf{B} generates a class of physically equivalent states starting from each state in \mathbf{B} . The class of physically equivalent states is called a *fiber*. The set \mathbf{B} itself is called the *base space*. One can imagine, for instance, the base space being a flat plane where each point represents a physically distinct quantum state and the gauge transformation applied to each point generating a vertical strand of physically equivalent states (Figure 2.2). The whole set, including \mathbf{B} and all fibers on it is called a *fiber bundle*, denoted by E .

In the example shown in Figure 2.2, the fiber bundle is a three dimensional space. A point in it is represented by three coordinates, out of which, the first two represent a point on the base \mathbf{B} and the third coordinate is a "gauge coordinate". Only the first two are physically relevant. In general, a point in the fiber bundle can be represented by coordinates which can be divided into two groups — the first group containing coordinates inside \mathbf{B} ("base coordinates") and a second group of fiber variables. A connection form describes

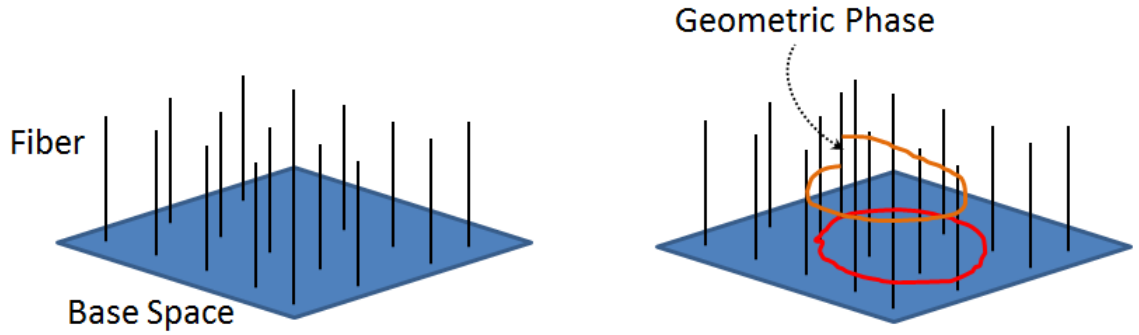


Figure 2.2: **Fiber bundles and holonomy.** (a) shows an elementary example of a fiber bundle (see main text). (b) shows a closed path (red circle) on the base space and its lift into the fiber bundle. The two endpoints of its lift lie on the same fiber and the difference between them is the holonomy element or the geometric phase of the closed path.

how the base space coordinates are *connected* to the fiber coordinates. If the base space is curved, then, any change in the base space coordinates will naturally change the fiber coordinates. Specifically, a connection form is a differential equation that tells how the fiber coordinates change in response to a change in the base coordinates. A connection form is defined by the dynamical equation of the quantum state, like the Schrödinger equation in the example of Berry’s phase.

Such a connection form assigns a “lift” to every path on the base space. If the coordinates of a point on the base are changed continuously in time, transporting the point along a loop, the connection form tells us how the fiber coordinates would change during the loop. Thus, they lift the path up in the fiber bundle (Figure 2.2). In general, although the base coordinates return back to what they were, the fiber coordinates do not return to what they were. Therefore, the lifted path is open, with its end points lying on the same fiber. The mismatch between the endpoints is represented by an element of the gauge group; since the fiber is generated by the action of a gauge group, we can “subtract” the two end points and obtain an element of the gauge group. In other words, the final point is obtained by multiplying the initial point by an element of the gauge group. This element is called the *holonomy* element of the connection form. A geometric phase, in general can be defined

as the holonomy element of the connection form defined by the dynamical equation of the physical system [1, 2]. Let us consider a few examples:

a. Berry's phase. In this example, the base space is the set of all eigenstates with eigenvalue m of the family of Hamiltonians: $H = \hat{n} \cdot \vec{S}$, with the overall phase ignored. The set of all unit vectors \hat{n} represents a sphere. Therefore, the base space \mathbf{B} is a sphere. The gauge transformation is a multiplication by a phase factor and therefore, the fiber is $U(1)$. The fiber bundle is obtained by attaching a circle at every point on a sphere. For half integer spins, the case of $m = \frac{1}{2}$ is described by the well known *Hopf fibration* (Figure 2.3). The fiber bundle in this case is a 3-sphere (*i.e.*, a sphere in 4 dimensional(4d) space). The connection form is defined by the Schrödinger equation [10].

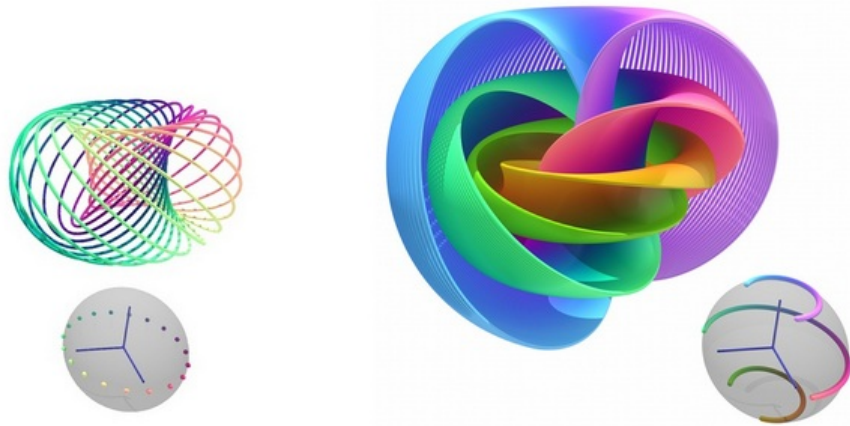


Figure 2.3: **Hopf fibration.** (Image from Wikipedia, https://en.wikipedia.org/wiki/Hopf_fibration) For half integer spins, Berry's phase is a holonomy of the Hopf fibration. The left side shows a torus obtained after attaching a circle at each point on the equator of a sphere. The right side shows successive nested tori obtained by attaching circles at each point on successive latitudes of the sphere. Latitudes to the north of the equator produce bigger tori and latitudes to the south of the equator produce smaller tori. The tori fill up \mathbb{R}^3 space, but they also identify infinity as a single point, because, at the north pole, the latitude reduces to a point. Thus, all the the tori together form a 3-sphere (S^3).

b. Uhlmann phase. Uhlmann [1] defined geometric phase for mixed states. The base space is the set of all mixed states of a quantum system. That is, \mathbf{B} is the set of all $n \times n$ matrices, ρ which are hermitian (*i.e.*, $\rho^\dagger = \rho$), positive semidefinite (*i.e.*, ρ has no negative

eigenvalue) and normalized (*i.e.*, $Tr(\rho) = 1$). That is:

$$\mathbf{B} = \{\rho : \rho^\dagger = \rho, \rho \geq 0, \& Tr(\rho) = 1\} \quad (2.1)$$

A pure state $|\psi\rangle$ is represented by a matrix $\rho = |\psi\rangle\langle\psi|$. The state vector $|\psi\rangle$ can be considered as an “amplitude” of its density matrix. In analogy, we may define an amplitude for a mixed state as a matrix W that satisfies $\rho = WW^\dagger$. Naturally, there are several amplitudes for any given mixed state. In particular, if W is an amplitude of ρ , then so is WU where U is any $n \times n$ unitary matrix (*i.e.*, $UU^\dagger = 1$). This is because, $(WU)(WU)^\dagger = WUU^\dagger W^\dagger = WW^\dagger = \rho$. The set of all amplitudes of a mixed state ρ are physically equivalent to ρ — they form the form the fiber strand at ρ .

Motivated by the above idea, we may define the gauge group as $U(n)$ — the set of all $n \times n$ unitary matrices. The fiber strand at any ρ is the set of order pairs — (W, U) where $U \in U(n)$ and $WU = \sqrt{\rho}$. The fiber bundle is $E = \mathbf{B} \times U(n)$ — there is a $U(n)$ fiber attached at each point of \mathbf{B} . (In general, not every fiber bundle is a product of the base space and the gauge group. For instance, the previous example(a), the base space was a sphere and the gauge group was $U(1)$, but the fiber bundle can’t be written as $\mathbf{B} \times U(1)$. However, in this example, \mathbf{B} is convex and hence *contractible*. And therefore the bundle is simply a product of the base and the gauge group.)

The connection form on this fiber bundle is defined by the differential equation [1].

$$W^\dagger \dot{W} = \dot{W}^\dagger W \quad (2.2)$$

This connection form does not come from a dynamical equation; instead, it is a natural generalization of the connection form in Berry’s phase [10]. For any path $\{\rho(t) : t \in [0, 1]\}$ in the base space, the above differential equation, together with the relation $WU = \sqrt{\rho}$ defines a lift — $\{(W(t), U(t)) : t \in [0, 1]\}$. The corresponding holonomy element $U(t = 1)U(t = 0)^\dagger$ is the geometric phase for the path. This formulation is quite general —

includes non-adiabatic evolution and open paths.

c. Sjöqvist phase. An alternate formulation of geometric phase for mixed states is provided by [11]. In this formulation, a density matrix is interpreted as a statistical average of pure states. Any $n \times n$ density matrix ρ , can be written as:

$$\rho = p_1|1\rangle\langle 1| + p_2|2\rangle\langle 2| + \dots + p_n|n\rangle\langle n| \quad (2.3)$$

$p_1, p_2 \dots p_n$ are the eigenvalues of ρ and $|1\rangle, |2\rangle \dots |n\rangle$ are the corresponding eigenstates. The eigenvalues are non-negative and their sum is 1 (because $Tr(\rho) = 1$). It is assumed that the matrix ρ has no degenerate eigenvalues (*i.e.*, no two of the eigenvalues are equal). Therefore, the set of eigenstates $|1\rangle, |2\rangle \dots |n\rangle$ are unique and the mixed state can be interpreted as a weighted average of pure states $|1\rangle, |2\rangle \dots |n\rangle$ with weights $p_1, p_2 \dots p_n$.

It is also assumed that the dynamics is a unitary evolution, *i.e.*, the density matrix at time t can be written as: $\rho(t) = U_t^\dagger \rho(0) U_t$ where U_t is a unitary propagator. One of the implications of a unitary evolution is that the eigenvalues of the density matrix do not change with time. Thus each density matrix $\rho(t)$ has the same set of eigenvalues $p_1, p_2 \dots p_n$, but the corresponding eigenstates change in time — $|1(t)\rangle, |2(t)\rangle \dots |n(t)\rangle$.

Thus, a closed loop in the space of density matrices is equivalent to n distinct closed loops of pure states, given by the eigenstates — $|1(t)\rangle, |2(t)\rangle \dots |n(t)\rangle$. Each of these loops has an associated Berry's phase — $\phi_1, \phi_2 \dots \phi_n$. The geometric phase of the loop of density matrices is defined as a statistical average of these n Berry's phases:

$$\phi = \text{arg.}(p_1 e^{i\phi_1} + p_2 e^{i\phi_2} + \dots + p_n e^{i\phi_n}) \quad (2.4)$$

d. Open paths, non-adiabatic evolution and non-hermitian Hamiltonian. Using the fiber bundle formulation of the definition of geometric phase, it is readily extended to open paths.

If the base space \mathbf{B} is a metric space, there is well defined geodesic. The geometric

phase accumulated when the system is transported along a geodesic is always zero. Therefore, the geometric phase of an open path can be defined to be equal to the geometric phase of the closed path obtained by connecting the end points using a geodesic on \mathbf{B} [12]. This is also in accordance with the definition of phase difference between two photons in different modes, given by Pancharatnam [13].

If the evolution along the path is non-adiabatic, it is still possible to extract the geometric phase from the total phase accumulated, by appropriately redefining the dynamical phase. As shown in [14], in this case, the dynamical phase can be defined as: $\gamma_d = \int \langle H \rangle dt$, where $\langle H \rangle$ is the expectation value of the Hamiltonian. Further, the definition has been extended to the case of cyclic evolution of non-hermitian Hamiltonians [15].

2.2 Previous experiments measuring geometric phase

Geometric phase has been measured in various physical systems and experimental techniques including photon interferometry, neutron interferometry and NMR interferometry [16, 17, 18].

Berry's phase appears as an optical activity in photonic systems. If the \vec{k} -vector of plane polarized light is transported around a closed path, the polarization rotates by an angle equal to the steradian angle enclosed by the path in the \vec{k} -space [19]. This phase has been observed using a helically wound optical fiber [20]. Non-planar interferometry, where a Michelson interferometer or a Mach-Zehnder interferometer is arranged with a non-planar optical path is another technique used to measure the Berry phase accumulated in a non-planar path [21, 22, 23, 24, 25, 26, 27, 28, 29, 30, 31, 32, 33].

Berry's phase has also been observed using neutron spin rotation experiments [34, 35, 36] and NMR interferometry [37, 38, 39]. Further, experimental measurements of Berry's phase using ultra cold atom interferometers have been done [40, 41, 42].

The generalization to mixed states provided by [11] has been observed experimentally using single photon interferometry [43], neutron interferometry [44, 45] and NMR interfe-

rometry [46, 47]. Geometric phase defined for non-cyclic evolution [12] has been measured experimentally using cold atoms [48]. Ultra cold neutrons [49] and solid state qubits [50] are other systems which have been used to demonstrate the appearance of Berry's geometric phase. Mixed state geometric phase following Uhlmann's definition has also been observed [51].

2.3 Recent developments: Fault tolerant quantum computation

It has been shown that geometrical phase is robust to statistical noise in the magnetic field [52, 53]. During an adiabatic evolution of a quantum state along a closed path, the accumulated geometric phase is proportional to the enclosed area. A fast fluctuation would presumably leave the area unchanged — the effect of fluctuations would integrate out to zero. In an explicit calculation [53], it is shown that the variance of the geometric phase is proportional to $\frac{1}{T}$, where T is the total time taken for the evolution along the path. The variance of the dynamical phase is proportional to T . Thus, in the adiabatic limit, the geometric phase is robust to noise in the magnetic field. In this calculation, the noise in the magnetic field is modeled by an Ornstein-Uhlenbeck process; *i.e.*, the noise is gaussian in its strength and a lorentzian with band width Γ in its frequency. Under the assumption that the fluctuations are much faster than the actual evolution, *i.e.*, $\Gamma T \gg 1$, the variance in the geometric phase is shown to be inversely proportional to T .

This effect has been verified experimentally [54, 55]. Due to this robustness to fluctuations, geometric phase is recognized as a promising candidate for phase gates in quantum computation [56, 57]. Fault tolerant quantum computing gates using geometric phase have been implemented recently [58, 59, 60].

CHAPTER 3

OUR GEOMETRIC PHASE

In this chapter, we qualitatively develop the theory of our geometric phase. In Chapter 4, we fill in the mathematical details. This chapter loosely follows Ref.[61]. A key idea behind the theory of our geometric phase is the minimum distance principle.

3.1 The Minimum Distance Principle

Geometric phases are carried by the system's gauge variables. For instance, in Berry's phase of a spin- $1/2$ system, the overall phase of the quantum state is the gauge variable. A point on the Bloch sphere does not completely specify the full quantum state vector; one has to append the overall phase, i.e., the gauge variable. Consequently, given a loop on the Bloch sphere, there are several ways of tuning the control parameters so as to transport a system along the loop. They all would induce the same loop, but differ in the profile of the overall phase along the loop. Of these, there is a special one, which corresponds to the parallel transport of the overall phase along the loop. Geometric phase of a loop is the mismatch between the initial and final overall phase values of the parallel transport. At the heart of this definition is the rule of parallel transport — what does it mean to parallel transport the overall phase? One way to define parallel transports is to use a structure called a connection form, which we do not elaborate here.

In general, the various ways of tuning the control parameters that all induce the same given loop, differ not only in the profile of the gauge variable, but also in the distance traversed in the full Hilbert space (including the gauge coordinate). Quite intriguingly, in all the well known examples of geometric phases, when the gauge variable is parallel transported, the system traverses the *least* possible distance in the Hilbert space [3, 62]. This prompts a more general definition of parallel transport — to parallel transport a system

is to minimize the distance traversed. If we tune the control parameters such that not only the given loop is induced, but also, the system travels the least distance in the full Hilbert space, then we have parallel transported the system. This holds for all examples of parallel transport. Indeed, it is intuitive that when a state is being parallel transported on the Bloch sphere, we carefully avoid any “unnecessary” changes to the overall phase. This is consistent with the idea of minimizing the total distance traversed in the Hilbert space, because changes in the overall phase also contribute to this distance. This also hints at a geometric interpretation of the dynamical phase — it is a measure of the deviation from minimality of distance traversed in the Hilbert space. If the actual path traversed in the Hilbert space is not the one that minimizes the length, the dynamical phase is non-zero and it needs to be subtracted from the total phase in order to obtain the geometric phase. To illustrate these ideas, we consider an example loop on the Bloch sphere.

Let us consider a latitude at θ (Fig. 3.1) on the Bloch sphere. Because this example is of Berry’s phase (and not our geometric phase), we consider a spin- $1/2$ system transported along this loop. The three obvious ways of doing this are illustrated in Fig. 3.1. The familiar adiabatic change of the direction of the applied magnetic field, where the spin vector remains parallel to it throughout (this was Berry’s original example) is shown in Fig. 3.1(a). Fig. 3.1(b) shows a constant field in the z -direction pulsed on for a period in which the spin vector completes exactly one rotation, thereby tracing out the loop. This is the example considered in [14]. Fig. 3.1(c) shows a magnetic field of constant magnitude, always maintained normal to the spin vector. This field transports the spin vector along the latitude, while itself traversing a different latitude. The three Hamiltonians (H_a, H_b, H_c)

Path	Path length	Total phase	Dynamical Phase	Geometric Phase
ψ_a	$\frac{2\pi\Omega}{\omega}$	$2\pi(\frac{\Omega}{\omega} - \cos \theta)$	$\frac{2\pi\Omega}{\omega}$	$-2\pi \cos \theta$
ψ_b	2π	0	$2\pi \cos \theta$	$-2\pi \cos \theta$
ψ_c	$2\pi \sin \theta$	$-2\pi \cos \theta$	0	$-2\pi \cos \theta$

Table 3.1: **The minimum distance principle:** Table shows the path length, total, dynamical and geometrical phase for the three ways of inducing the latitude shown in Fig. 3.1. The path length is least in ψ_c and this corresponds to the parallel transport.

and the corresponding times (T_a, T_b, T_c) are:

$$\begin{aligned}
H_a(t) &= \Omega \cos \theta \sigma_z + \Omega \sin \theta \cos(\omega t) \sigma_x + \Omega \sin \theta \sin(\omega t) \sigma_y \\
\Omega &\gg \omega \ \& \ T_a = \frac{2\pi}{\omega} \\
H_b(t) &= \Omega \sigma_z : \quad T_b = \frac{2\pi}{\Omega} \\
H_c(t) &= -\Omega \sin \theta \sigma_z + \Omega \cos \theta \cos(\omega t) \sigma_x + \Omega \cos \theta \sin(\omega t) \sigma_y \\
\Omega &= \omega \sin \theta \ \& \ T_c = \frac{2\pi}{\omega}
\end{aligned} \tag{3.1}$$

$\sigma_{x,y,z}$ are the Pauli matrices. Starting with the same initial state $|\psi\rangle$, the three Hamiltonians induce the same path on the Bloch sphere, but different paths in the Hilbert space — they differ in the profile of the overall phase. Explicitly, the paths in the Hilbert space are,

$$\begin{aligned}
|\psi_a(t)\rangle &= e^{i\omega t \sigma_z} e^{it\sigma_a} |\psi\rangle : \quad \sigma_a = (\omega + \Omega \cos \theta) \sigma_z + \Omega \sin \theta \sigma_x \\
|\psi_b(t)\rangle &= e^{i\Omega t \sigma_z} |\psi\rangle \\
|\psi_c(t)\rangle &= e^{i\omega t \sigma_z} e^{it\sigma_c} |\psi\rangle : \quad \sigma_c = (\omega - \Omega \sin \theta) \sigma_z + \Omega \cos \theta \sigma_x
\end{aligned} \tag{3.2}$$

The lengths of the three paths are computed using $s = \int \sqrt{\langle \dot{\psi} | \dot{\psi} \rangle} dt = \int \sqrt{\langle \psi | H^2 | \psi \rangle} dt$ and the dynamical phase using $\phi_d = \int \langle \psi | H | \psi \rangle dt$ (see Ref. [14]). Below is a table comparing the three paths:

Clearly, ψ_c has the least length among the three and in fact, among *all* possible paths, because its length is equal to that of the latitude [3]. This is indeed the parallel transport

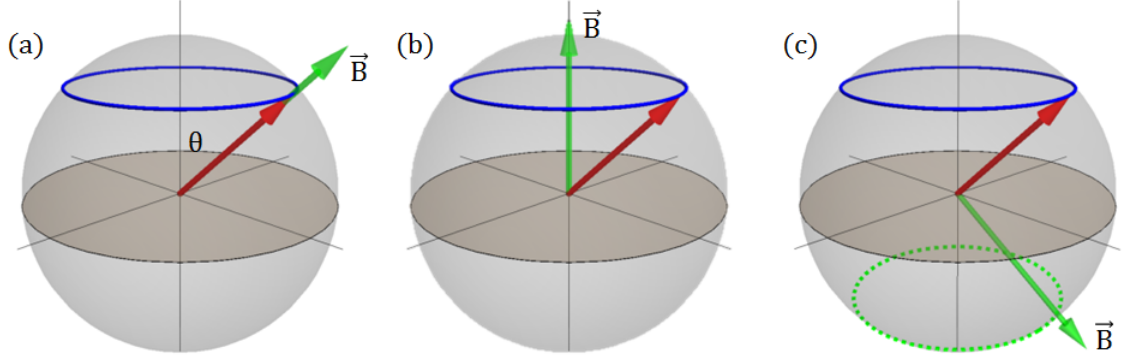


Figure 3.1: **Dynamical Phase:** (a), (b) and (c) show three different ways of inducing a latitude in a spin-1/2 system. The magnetic field in each case is indicated by \vec{B} . While the geometric phase is the same for all three of them, the dynamical phase is different (see text).

(see ref. [63]). ψ_a has the largest path length (because $\Omega \gg \omega$) and that is reflected in the very large dynamical phase. Intuitively, dynamical phase is a unnecessary rotation of the quantum state about its own spin vector, causing the system to traverse a longer path in the Hilbert space. Such rotations have been cautiously avoided in ψ_c , resulting in a zero dynamical phase and minimal path length.

The above examples illustrate two fundamental ideas regarding geometric phases — first, that geometric phase is a purely kinematic property depending only on the geometry of the loop, regardless of the dynamics inducing the loop [64, 65] and second, minimization of the length is a general definition of parallel transport. Berry's phase can be defined by the minimization of the path length. For instance, let $\hat{n}(t)$ be a loop on the Bloch sphere and $\psi(t)$ be one of its lifts in \mathbb{C}^2 . We assume that $\psi(t)$ is normalized. All other lifts of $\hat{n}(t)$ with the same initial point are of the form $e^{ix(t)}\psi(t)$, where $x(t)$ is a real scalar with $x(0) = 0$. The length of these lifts (s) is given, under the Euclidean metric, by $s = \int \sqrt{|\dot{\psi}(t)|^2 + |\dot{x}|^2 + i\dot{x}(\langle \dot{\psi}, \psi \rangle - \langle \psi, \dot{\psi} \rangle)} dt$. The first order functional derivative of s w.r.t to $x(t)$ is $\langle \dot{\psi}, \psi \rangle - \langle \psi, \dot{\psi} \rangle$ and it should vanish if ψ is a horizontal lift, according to the new definition. Together, with $|\psi(t)| = 1$, we obtain the correct parallel transport criterion: $\langle \dot{\psi}, \psi \rangle = 0$, i.e., the Berry connection form [10]. The same argument applies for

Aharonov-Anandan phase [14].

Further, *all* known examples of geometric phases can be formulated using the minimum distance principle. We illustrate this point with the Wilczek-Zee phase. We follow the generalization of Wilczek-Zee phase in [66], and show that the connection form thereof can be derived by minimizing the length. Let us assume that the Hilbert space can be decomposed into a direct sum of two subspaces with dimensions n and m respectively (denoted by V_n and V_m). V_n is the time dependent n dimensional eigenspace of the Hamiltonian. We are to define parallel transport of a vector $\psi \in V_n(0)$ in time, i.e., we are to define a path $\psi(t) \in V_n(t)$ with $\psi(0) = \psi$ and minimal length. Given any lift, $\psi(t)$, we can construct other such lifts by a transformation $U(t)\psi(t)$, where $U(t)$ is a unitary operator with all of its non-trivial eigenvectors in $V_n(t)$. The length of such a path is $s = \int \sqrt{\|\dot{\psi}(t)\|^2 + \langle \dot{U}\psi | \dot{U}^\dagger \psi \rangle + \langle U^\dagger \dot{U} \psi | \dot{\psi} \rangle + \langle \dot{\psi} | U^\dagger \dot{U} \psi \rangle} dt$. Again, setting $U^\dagger \dot{U} = iH(t)$ for some Hermitian operator $H(t)$, the first derivative of s is $\langle H(t)\dot{\psi} | \psi \rangle - \langle \psi | H(t)\dot{\psi} \rangle$. $H(t)$ is an arbitrary Hermitian with zero eigenvalues in $V_m(t)$. Therefore, s is stationary iff $\dot{\psi}$ is orthogonal to $V_n(t)$, indeed the same condition as equation (7) in ref. [66].

Using these two ideas, we provide a mathematical definition of our geometric phase in the following section.

3.2 Definition of Geometric Phase

Geometric phase arises in this system when the ellipsoid is parallel transported along a closed loop inside the Bloch sphere (Fig. 3.2). As a result of the parallel transport, the ellipsoid returns in a different orientation which can be described by a 3D rotation, represented by a 3×3 matrix. This rotation matrix (R), a member of the $SO(3)$ group, is the geometric phase of the loop. This geometric phase is an operator, unlike Berry's phase which is a complex scalar, and is therefore more similar to Wilczek-Zee phase [67] and Uhlmann phase [1], both of which are unitary matrices. This can be measured easily in the components of the spin fluctuation tensor, specifically, the component T_{ij} changes to

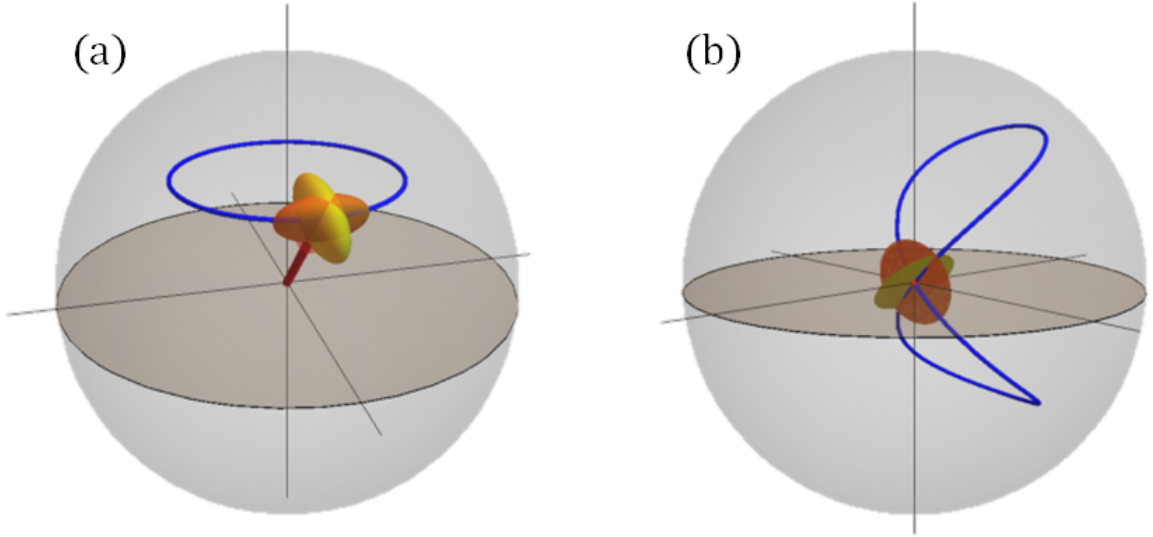


Figure 3.2: **Geometric Phases Carried by the Ellipsoid:** (a) and (b) show the geometric phase carried by the ellipsoid when parallel transported along a non-singular and a singular loop inside the Bloch sphere respectively. In either of these cases, the final orientation of the ellipsoid is different from the initial orientation, due to an $SO(3)$ geometric phase. For singular loops, this geometric phase is non-Abelian.

$R_{il}T_{lk}R_{jk}$ after the parallel transport.

In our geometric phase, the gauge variables are the components of the spin fluctuation tensor. The space of quantum states has a metric, known as the Fubini-Study metric (s_{FS}), which is essentially the fidelity measure between two normalized quantum states ψ_1, ψ_2 :

$$s_{FS}(\psi_1, \psi_2) = \cos^{-1}(|\langle \psi_1 | \psi_2 \rangle|) \quad (3.3)$$

Hereafter, we write a loop inside the Bloch sphere parameterized by t as $\vec{S}(t)$ with the parameter ranging from 0 to t_{final} . Parallel transport of the ellipsoid (or the chord) along $\vec{S}(t)$ is a loop in the space of quantum states, which we may write $\psi(t) \equiv (\vec{S}, \pm \hat{u}(t))$, where, $\hat{u}(t)$ is a unit vector in space chosen such that it is always normal to \vec{S} and the length of $\psi(t)$ under the Fubini-Study metric is minimized. This condition, of minimizing

the length translates to the following differential equation on $\hat{u}(t)$ [5] :

$$\frac{d}{dt}\hat{u}(t) = - \left(\frac{d}{dt} \frac{\vec{S}(t)}{|\vec{S}(t)|} \cdot \hat{u}(t) \right) \frac{\vec{S}(t)}{|\vec{S}(t)|} \quad (3.4)$$

The parallel transport of any starting state $\psi(0)$ along $\gamma(t)$ is obtained by solving the above differential equation with the corresponding initial value of $\hat{u}(t)$.

The corresponding geometric phase, i.e., the $SO(3)$ operator R is also obtained by solving a differential equation. We introduce a path $X(t)$ in $SO(3)$ which satisfies the following differential equation (we have used $\frac{\vec{S}(t)}{|\vec{S}(t)|} = \hat{v}(t)$ for simplicity here):

$$\begin{aligned} \frac{d}{dt}X(t) &= \left(\frac{d\hat{v}(t)}{dt} \hat{v}(t)^T - \hat{v}(t) \frac{d\hat{v}(t)}{dt}^T \right) X \\ X(0) &= 1 \end{aligned} \quad (3.5)$$

The superscript “ T ” indicates the transpose of a vector. The solution to this equation provides $X(t)$ and, the geometric phase of $\vec{S}(t)$ is given by $R = X(t_{final})$. Finally, the generalized solid angle is given by $\cos^{-1}(\hat{k} \cdot R\hat{k})$, where \hat{k} is some vector normal to both $\hat{v}(0)$ and $\hat{v}(t_{final})$. This is the angle by which R rotates a vector normal to $\hat{v}(0)$ and $\hat{v}(t_{final})$.

3.3 Interpretation: The generalized solid angle

Geometrical interpretation of this geometric phase, particularly for singular loops, needs an extended notion of solid angles introduced in [5] as *generalized solid angles*. For a non-singular loop, the geometric phase is a rotation about the spin vector by an angle equal to the solid angle of the loop (3.3(a)). This is because the parallel transport of the ellipsoid inside the Bloch sphere along a non-singular loop is reminiscent of the parallel transport of a tangent vector to a sphere. The solid angle of a non-singular loop is the angle of the cone obtained by sweeping a radius along the loop (3.3(a)), which produces a *radial projection* of the loop. For the case of singular loops, this geometric notion of solid angles is not well

defined, as illustrated in Figure 3.3(b). The radial projection is discontinuous and therefore, such loops require a generalization of the notion of solid angles.

The key idea behind generalized solid angles is to use *diametric* projections, instead of radial projections. The discontinuous jumps in a radial projection of singular loops are always diametrically opposite (3.3(b)) and therefore, sweeping a diameter along the loop generates a continuous cone with a well defined angle (3.3(c)). This angle is equal to the standard solid angle for non-singular loops and is a convenient generalization to singular loops.

While the standard solid angle is the integrated curvature or *holonomy* of a loop on a sphere, the generalized solid angle is the holonomy of a loop on a *real projective plane* (Supplementary Information). The latter is an abstract manifold, defined as the configuration space of a two-sided symmetric rigid rotor, each of whose configuration is a diameter of a sphere. It is also the space of all $m = 0$ spin states of an integer spin system and possesses unusual geometric and topological properties [68]. Because it is a close relative of the sphere, it is known as a “half sphere” and it is also the configuration space of nematic crystals. It is non-orientable and has no embedding in real three dimensional space; however, it can be represented by an immersion, i.e., a self intersecting surface, known as Boy’s surface [69] (3.3(d)). The cone generated by sweeping a diameter along a loop inside the Bloch sphere represents a path in the real projective plane. Thus, using a diametric projection, a loop inside the Bloch sphere is projected to the real projective plane, and the holonomy of the projected path is defined as the generalized solid angle of the loop inside the Bloch sphere [5]. The diametric projection also equips us with a concise way of determining the geometric phase operator R . The two endpoints of the diameter trace out a pair of congruent loops on the surface of the Bloch sphere, which we may parametrize in time as $+\hat{n}(t)$ and $-\hat{n}(t)$ respectively. The geometric phase is then given by

$$R = \mathcal{T} \exp \left\{ \int (\dot{\hat{n}}\hat{n}^T - \hat{n}\dot{\hat{n}}^T) dt \right\} \quad (3.6)$$

Here, \mathcal{T} refers to the time ordering operator and the integral is evaluated through the loop.

Thus, the generalized solid angle of a loop inside the Bloch sphere can be defined as the *holonomy* of its diametric projection into the real projective plane (\mathbb{RP}^2). The mathematical details can be found in chapter 4. In this section, we address the qualitative questions of what is meant by *holonomy*? Why is it equal to the solid angle of the cone generated by sweeping a diameter along the loop? and how is it a justifiable generalization of the standard solid angle? Although these questions are answered in Ref. [5], here we provide a more intuitive and a qualitative version of it.

3.3.1 What is “Holonomy”?

Holonomy roughly translates to ‘a local quantity which captures a global property’, an elementary example of which is the so called *spherical excess* of a spherical triangle. While it is well known that the sum of internal angles of a spherical triangle exceeds π by an amount known as the spherical excess, a lesser known fact is that the spherical excess is equal to the area or the solid angle enclosed by the triangle, known as Girard’s theorem.

The spherical excess is quite obviously related to parallel transports. The sum of internal angles of a spherical triangle and the sum of its external angles together sum up to 3π . Therefore, the latter falls short of 2π by the spherical excess. It is easy to picture the sum of external angles — a car driven along a spherical triangle on the earth is steered by an amount equal to the sum of the external angles ¹. While the car comes back to its original orientation, i.e., rotates effectively by 2π , it’s steering wheel is rotated by less than 2π . This means, if the car were parallel transported, i.e., moved somehow along the spherical triangle without being steered, it would return in a different orientation, rotated by the spherical excess.

So far, we have used only the trivial properties of a spherical triangle. An elementary, but non-trivial property of a spherical triangle is the Girard theorem, which says that the

¹We are assuming that the car’s steering rotation correctly represents the car’s actual rotation.

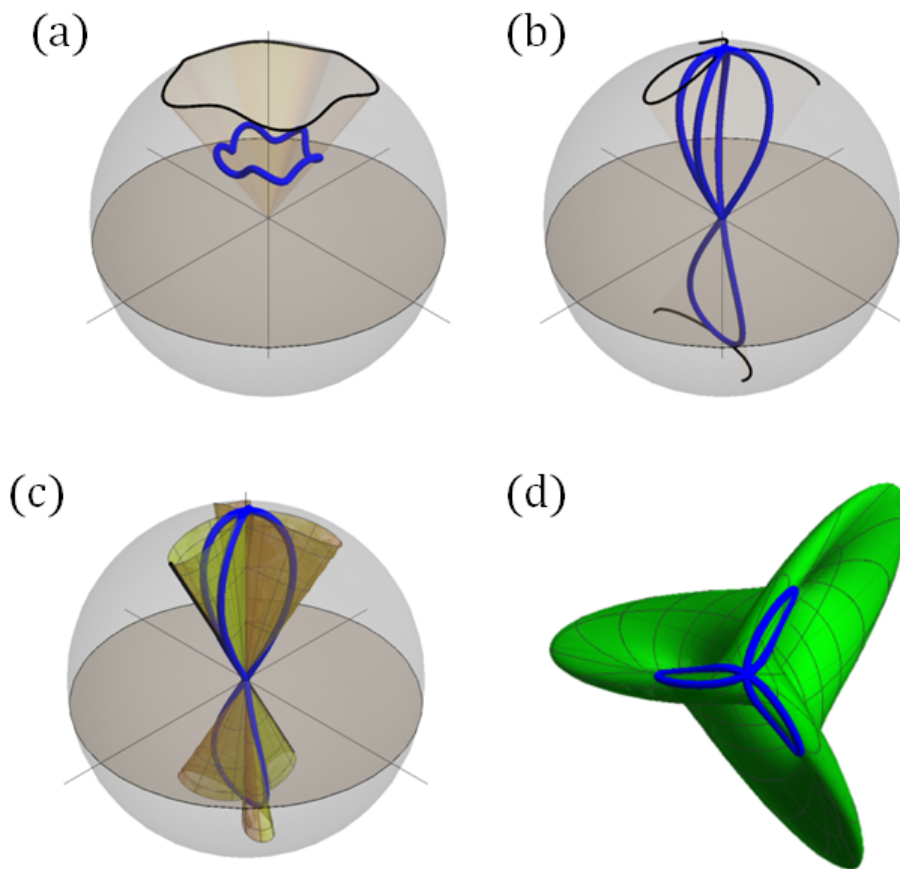


Figure 3.3: **Interpretation of Geometric Phases:** (a) and (b) contrast non-singular and singular loops under a radial projection. The former has a continuous projection and a well defined solid angle, while the latter doesn't. This problem is resolved by defining a generalized solid angle for singular loops using a diametric projection, as illustrated by (c) and (d). (c) shows a surface obtained by sweeping a diameter along the loop. The solid angle enclosed by this surface is the generalized solid angle of the singular loop. This surface is indeed a loop in the space of diameters of a sphere, i.e., in a real projective plane (\mathbb{RP}^2). (d) shows a Boy's surface, a representation of the real projective plane, together with the loop projected on it. The generalized solid angle is equal to the holonomy of this loop.

spherical excess of a triangle is exactly equal to the enclosed solid angle. This means that the car’s rotation, a local quantity, actually captures a global property — the solid angle. Therefore, we may refer to the angle of rotation due to parallel transport as a “holonomy”.

Naturally, when a tangent line is being parallel transported along a loop on a sphere, we expect that the distance traversed in some space is being minimized. To build an analogy with the geometric phase discussed in the previous section, tangent lines with a fixed point of tangency have one degree of freedom i.e., rotation about the point of tangency and this is the gauge variable. The full configuration space of the tangent line is a three dimensional manifold. A configuration of the tangent line is specified by three coordinates, including two of the point of tangency and one of the orientation of the tangent line. Transporting a tangent line along a loop on a sphere would correspond to a path in this configuration space. This configuration space has a nontrivial topology and is known as *lens space*, $L(4, 1)$. This space can be understood as a “bundle of circles” over a sphere. That is, at each point on a sphere, a circle is attached to carry the gauge variable. This structure is known as a *circle bundle* over a sphere. The rule assigning a parallel transport is known as *connection form*, which, in the present case is formulated as minimization of a distance. The solid angle of a loop on the sphere is the holonomy of the *natural* connection form on this bundle. Natural here means maximally symmetric, i.e., one that does not involve an arbitrary choice (of a basis, etc) and in this case it comes from a natural metric on $L(4, 1)$. Owing to Girard’s theorem, the solid angle can be *defined* as the holonomy of the natural connection form.

3.3.2 Holonomy of loops on \mathbb{RP}^2

A non-singular loop inside the Bloch sphere can be radially projected into the sphere and its solid angle can be defined as the holonomy of the projection. While singular loops can not be continuously projected to a sphere, both non-singular and singular loops can be continuously projected to the real projective plane through a diametric projection. Therefore, the appropriate definition of generalized solid angle is the holonomy of these projections in

\mathbb{RP}^2 , provided, it agrees with the standard solid angle for the subset of non-singular loops.

That raises the question, what is the appropriate holonomy for loops on \mathbb{RP}^2 ? Incidentally, $L(4, 1)$ is also a circle bundle over \mathbb{RP}^2 ; in fact, $L(4, 1)$ is also the configuration space of a unit tangent vector to \mathbb{RP}^2 . At each point on \mathbb{RP}^2 , the tangent vector has a circle's worth of configurations, which form a circle in $L(4, 1)$ corresponding to the point in \mathbb{RP}^2 . This bundle also has a natural connection form that defines parallel transport of the unit tangent vector along a loop on \mathbb{RP}^2 . The holonomy of a loop in \mathbb{RP}^2 is defined as the angle of rotation of a unit tangent vector when parallel transported along the loop. The corresponding connection form also comes from the same metric on $L(4, 1)$ and the corresponding holonomy does agree with the standard solid angle for projection of non-singular loops [5]. In fact, $L(4, 1)$ is the only lens space that is a circle bundle over both sphere and \mathbb{RP}^2 .

While the generalized solid angle is a scalar, the geometric phase has been defined as an $SO(3)$ operator. Because the Bloch sphere has a singularity at the center, it is important to retain more information than just an angle of rotation. Consequently the geometric phase, as it is defined, is the full $SO(3)$ operator.

3.3.3 Holonomy of open paths in \mathbb{RP}^2

Before ending this section, we discuss the holonomy of open paths in \mathbb{RP}^2 . Like the loop induced in the experiment, it is possible that the projection of a singular loop is an open path in \mathbb{RP}^2 . The geometric phase, being an $SO(3)$ operator, is still well defined and represents a transformation between the tangent vectors of \mathbb{RP}^2 at the two endpoints of the loop. However, generalized solid angle, which is just the angle of rotation needs some clarification.

The problem of deciding the angle between two tangent vectors at two different points on \mathbb{RP}^2 is analogous to the problem of comparing the phases of two laser beams in different momentum modes and dates back to 1956 [13]. The straightforward solution is to connect

the two points by a geodesic and thereby close the open path. Geodesics in general have the special property that they do not accumulate any geometric phase [12].

Accordingly, the generalized solid angle is defined as follows: if R is the geometric phase of a loop whose projection is open in \mathbb{RP}^2 and d_1 and d_2 are its endpoints (i.e, the diameters to a sphere representing the initial and final points on \mathbb{RP}^2), the generalized solid angle is

$$\Omega = \cos^{-1}(\hat{k} \cdot R\hat{k}) \quad (3.7)$$

for some unit vector \hat{k} which is normal to both d_1 and d_2 . If $d_1 = d_2$, i.e., if the path is closed in \mathbb{RP}^2 , Ω is simply the angle of rotation of R . If $d_1 \neq d_2$, the above expression provides the holonomy of the loop obtained by closing the path using a geodesic in \mathbb{RP}^2 .

CHAPTER 4

THE MATHEMATICAL THEORY OF OUR GEOMETRIC PHASE

In this chapter, we develop the theory of our geometric phase with full mathematical rigor. This theory has been published in Ref.[5] and this chapter largely follows this paper. We begin with an overview of the mathematics of the phase space of spin-1 systems, followed by a summary of Ehresmann connection — a tool that we use to develop the theory of geometric phases. Finally, we provide rigorous definition the geometric phase and discuss its interpretation.

4.1 The Complex Projective Plane

The quantum state of a spin-1 system is represented by a non-zero vector $\psi = (z_{-1}, z_0, z_{+1})^T$ in the 3-dimensional complex Hilbert space \mathbb{C}^3 ; here superscript T denotes matrix transpose. The physical properties of the spin system are invariant under a multiplication of this vector by a non-zero complex scalar, i.e., ψ and $\lambda\psi$ are physically equivalent state vectors for $\lambda \in \mathbb{C} - \{0\}$; this defines an equivalence class under the equivalence relation $\psi \sim \lambda\psi$. The quotient space under this equivalence is a four dimensional manifold. Topologically, the manifold is the *complex projective plane* ($\mathbb{C}\mathbb{P}^2$), defined as the space of all lines in a 3-dimensional complex vector space passing through the origin:

$$\mathbb{C}\mathbb{P}^2 = \left\{ \psi \in \mathbb{C}^3 - \{\vec{0}\} : \psi \sim \lambda\psi \text{ for } \lambda \in \mathbb{C} - \{0\} \right\} \quad (4.1)$$

Equivalently, $\mathbb{C}\mathbb{P}^2$ is the space of all 1-dimensional subspaces of \mathbb{C}^3 . Each 1-dimensional subspace of \mathbb{C}^3 represents an equivalence class. The spin expectation values can be written as $\langle S_i \rangle = \frac{\langle \psi, S_i \psi \rangle}{\langle \psi, \psi \rangle}$, where $\langle \cdot, \cdot \rangle$ is the standard inner product on \mathbb{C}^3 . We may define a map $\phi : \mathbb{C}\mathbb{P}^2 \rightarrow \mathbb{B}$ that takes every equivalence class of \mathbb{C}^3 to its real space spin vector: $\phi(\psi) = \vec{S}$.

In terms of coordinates, for a vector $\psi = (z_{-1}, z_0, z_{+1})^T$ representing the equivalence class $\{\lambda\psi : \lambda \in \mathbb{C} - \{0\}\}$, the image under this map is:

$$\phi \left(\begin{pmatrix} z_{-1} \\ z_0 \\ z_{+1} \end{pmatrix} \right) = \frac{1}{|z_{-1}|^2 + |z_0|^2 + |z_{+1}|^2} \begin{pmatrix} \sqrt{2}\text{Re}(z_{-1}z_0^* + z_0z_{+1}^*) \\ \sqrt{2}\text{Im}(z_{-1}z_0^* + z_0z_{+1}^*) \\ |z_{+1}|^2 - |z_{-1}|^2 \end{pmatrix} = \vec{S} \in \mathbb{B} \quad (4.2)$$

We note that the map ϕ is independent of the choice of the representative in any equivalence class and therefore, it is well defined. In other words, $\phi(\psi) = \phi(\lambda\psi)$ for $\lambda \in \mathbb{C} - \{0\}$.

The components of the spin fluctuation tensor can also be written in terms of the coordinates of ψ . Together, the spin vector and the spin fluctuation tensor contain all the information about the spin-1 quantum state. Indeed, every spin-1 state is uniquely represented by the pair (\vec{S}, \mathbf{T}) . Defining a parallel transport of ellipsoids along a loop in \mathbb{B} is tantamount to defining a horizontal lift of loops in \mathbb{B} to $\mathbb{C}\mathbb{P}^2$. The map $\phi : \mathbb{C}\mathbb{P}^2 \rightarrow \mathbb{B}$ does not, however, have a fiber bundle structure. Any fiber bundle over \mathbb{B} is necessarily a product bundle as \mathbb{B} is a contractible space. The space $\mathbb{C}\mathbb{P}^2$, being 4-dimensional, is not a product bundle over \mathbb{B} because it has non-trivial second homology. Any 4-dimensional product bundle over \mathbb{B} , being homotopic to the 1-dimensional fiber itself, would have a trivial second homology. Therefore, this geometric phase cannot be formulated as a holonomy of loops in \mathbb{B} , in general. We use a modified notion of holonomy to define this geometric phase. We begin with a summary of Ehresmann connection — the standard tool used to define holonomies in the section 4.2 and use a modified version of it to develop the theory of geometric phases in our system in section 4.3.

4.2 Ehresmann Connection

The well known parallel transport of tangent vectors on a sphere is formulated using the affine connection. However, our geometric phase can not be formulated using affine connection because its features are compatible only with Ehresmann connection. In order to

put our geometric phase in perspective with the other well known examples and to bridge the gap between affine connection and Ehresmann connection, in this section, we show how the former naturally generalizes to the latter and that minimizing the length is a concise way of defining parallel transports.

We begin with an overview of affine connection. Let M be an n -manifold and TM be its tangent bundle. At a point $q \in M$, with local coordinates (x^1, x^2, \dots, x^n) , the tangent plane, T_qM is an n dimensional vector space spanned by $e_\mu = \frac{\partial}{\partial x^\mu}$, $\mu = 1, 2, \dots, n$. Central to an affine connection is the covariant derivative, which comes from “differentiating” the basis vectors, $\frac{\partial}{\partial x^\nu} e_\mu = \Gamma_{\mu\nu}^\sigma e_\sigma$. In the more formal language, the covariant derivative, denoted by “ D ” is defined as $De_\mu = \Gamma_{\mu\nu}^\sigma e_\sigma \otimes dx^\nu$.

The basic problem, that the affine connection is designed to solve is to define a parallel transport $\tilde{\gamma}$, i.e., a horizontal lift, in TM for a path γ in M . This can be restated as follows: for a point $q \in M$ on γ with a given a lift $(q, v) \in TM$ on $\tilde{\gamma}$ (where $v = v^\mu e_\mu \in T_qM$) and the local tangent vector $y = y^\mu e_\mu$ of γ , along which q is moved, how do we change the coordinates v^μ in order to maintain the vector v parallel to itself? In other words, we are to decide the local tangent vector t of $\tilde{\gamma}$, that moves the point $(q, v) \in TM$ such that q is moved along y and v remains parallel to itself. This tangent vector is in the $2n$ dimensional tangent plane of TM at (p, v) , i.e., $t \in T_{(q,v)}(TM)$. This space is spanned by the basis vectors $(e_1, e_2, \dots, e_n, f_1, f_2, \dots, f_n)$, where $f_\mu = \frac{\partial}{\partial v^\mu}$. Quite obviously, $t = y^\mu e_\mu + z^\nu f_\nu$, for a suitable choice of coefficients z^ν such that $tDv = 0$. This condition is the parallel transport criterion. Using $Dv = D(v^\mu e_\mu) = dv^\mu e_\mu + v^\mu De_\mu$, we get $z^\mu e_\mu + \Gamma_{\mu\nu}^\sigma e_\sigma y^\nu v^\mu = 0$. For convenience, the connection matrix is defined as $\omega_\nu^\mu = \Gamma_{\nu\sigma}^\mu y^\sigma$, in terms of which, $z^\mu = -\omega_\nu^\mu y^\nu$ [70].

In order to move towards Ehresmann connection, we rewrite the affine connection in a coordinate-free form. Two observations are crucial. First, in the $2n$ dimensional tangent space $T_{q,v}(TM)$, the n dimensional subspace spanned by f_μ represent changes to the tangent v alone and is therefore known as the *vertical subspace* of $T_{(q,v)}(TM)$. And second,

the special vectors $t \in T_{(q,v)}(TM)$ that satisfy $tDv = 0$ also form an n dimensional subspace spanned by $\{e_\mu - \omega_\mu^\nu f_\nu : \mu = 1, 2, \dots, n\}$. This space complements the vertical subspace and is known as *horizontal subspace* of $T_{(q,v)}(TM)$. It is straightforward to see that all that the affine connection does is to identify this horizontal subspace at each point of TM . Indeed, any n dimensional subspace of $T_{(q,v)}(TM)$ that complements the vertical subspace uniquely defines the elements ω_μ^ν of the connection matrix. This follows from the fact that the vector e_μ can be written uniquely as a sum of two vectors, one in the horizontal subspace and one in the vertical subspace. Thus, in the coordinate-free form, a connection is a specification of a horizontal subspace at each point of TM , that complements the vertical subspace. Indeed, it is an n dimensional distribution over TM .

This definition extends to any fiber bundle and is known as Ehresmann connection. Apart from being coordinate-free, it also has two other advantages over the affine and the Levi-Civita connections. The covariant derivative, upon which the affine and Levi-Civita connections are based, is rooted in differentiating vector fields over a manifold (i.e., sections of the vector bundle). In a fiber bundle where the fiber has non-trivial topology, in general there are no sections. The Ehresmann connection is therefore the most natural way of defining horizontal lifts. Furthermore, the Ehresmann connection generalizes naturally to structures that are not bundles. The dimension of the horizontal space can be non-uniform. Such a connection, however, can not be traced back to a connection matrix and therefore, regarding a connection as a distribution becomes inevitable.

If a fiber bundle has a natural Riemannian metric, the horizontal subspace can be defined as the orthogonal complement of the vertical subspace. The resulting horizontal lifts minimize the path length. The tangent vector to the horizontal lift is always confined to the local horizontal subspace and because the vertical subspace is orthogonal to it, any added component would only make the lift longer.

In our system, at most of the points in $\mathbb{C}\mathbb{P}^2$, the vertical subspace is one dimensional and the horizontal subspace, defined by the Fubini-Study metric is three dimensional. However,

at some points, i.e., within the pre-image of the center of the Bloch ball, the vertical and the horizontal subspaces are both two dimensional. This feature adds all the non-trivialities to the system and therefore, we have to use Ehresmann connection in this problem.

4.3 Definition of Horizontal Lift And Geometric Phase

In definitions 1 and 2 below, we answer (i) by invoking the important role played by metrics in the theory of geometric phase [3], [71], [72]. In the definition of Berry’s phase and Uhlmann’s phase, horizontal lifts are constructed using Berry’s connection form [10] and Uhlmann’s connection form [1], respectively. It has been noted that in both of these cases, the horizontal lift can also be defined as the lift with minimal length in the respective fiber bundles [3, 62]. For a general Ehresmann connection [73], if the horizontal subspace of the tangent space of a fiber bundle is defined as the orthogonal complement of the vertical subspace under a Riemannian metric, the resulting horizontal lift of a loop always minimizes the length among all lifts of the loop. While $\mathbb{C}\mathbb{P}^2$ is not a fiber bundle over \mathbb{B} , it has a standard, natural (i.e., maximally symmetric) metric — the Fubini-Study metric (s_{FS}) [8]. It is essentially the “angle” between two quantum state vectors in the Hilbert space:

$$s_{FS}(\psi_1, \psi_2) = \cos^{-1} \left(\frac{|\langle \psi_1, \psi_2 \rangle|}{\sqrt{\langle \psi_1, \psi_1 \rangle \langle \psi_2, \psi_2 \rangle}} \right) \quad (4.3)$$

We note that this definition extends to $\mathbb{C}\mathbb{P}^2$, when we employ any Hilbert space representatives for the equivalence classes corresponding to the points in $\mathbb{C}\mathbb{P}^2$, i.e., it is invariant under scalar multiplications: $s_{FS}(\psi_1, \psi_2) = s_{FS}(\lambda_1\psi_1, \lambda_2\psi_2)$ where $\lambda_1, \lambda_2 \in \mathbb{C} - \{0\}$. We define a horizontal lift for loops in \mathbb{B} using this metric.

Definition 1 (Horizontal Lift): A continuous path $\tilde{\gamma} : [0, 1] \rightarrow \mathbb{C}\mathbb{P}^2$ is called a *horizontal lift* of a loop $\gamma : [0, 1] \rightarrow \mathbb{B}$ iff $\phi \circ \tilde{\gamma} = \gamma$ and $\tilde{\gamma}$ minimizes the Fubini-Study length in $\mathbb{C}\mathbb{P}^2$.

In the next section, we show that the earlier described intuitive notion of parallel trans-

port of the ellipsoids along a loop in \mathbb{B} is equivalent to the above definition of a horizontal lift of the loop. We show that, corresponding to every choice of $\tilde{\gamma}(0)$ satisfying $\phi(\tilde{\gamma}(0)) = \gamma(0)$, there is a unique horizontal lift of γ . In the next section, we provide explicit equations to compute the horizontal lift of a given loop and a given initial point of the lift. Before proceeding to define a geometric phase using this horizontal lift, we note that not every loop in \mathbb{B} has a well-defined horizontal lift in $\mathbb{C}\mathbb{P}^2$. The relevant regularity conditions on the loop are summarized in theorem 1.

Theorem 1 (Existence criteria for horizontal lifts): A continuous, piece-wise differentiable loop $\gamma : [0, 1] \rightarrow \mathbb{B}$ has a horizontal lift if it is differentiable at every $t \in [0, 1]$ where $\gamma(t) = \vec{0} \in \mathbb{B}$.

This theorem essentially states that a loop in \mathbb{B} has a horizontal lift if it has no “kinks” while passing through the center of \mathbb{B} . We refer to the loops satisfying the condition mentioned in this theorem as *liftable* loops. Clearly, any piece-wise differentiable loop not passing through the center of \mathbb{B} is liftable. Fig. 4.1 shows two examples of liftable loops and one example of a loop that is not liftable. Fig. 4.1 (b) is an important example of a loop that appears to have a kink at the center of \mathbb{B} , but is nevertheless liftable. The apparent non-differentiability at the center is removable. If we choose the center as the starting and the ending points of the loop, i.e., $\gamma(0) = \gamma(1) = \vec{0} \in \mathbb{B}$, the loop satisfies all conditions mentioned in the theorem. However, the loop in Fig. 4.1 (c) is not liftable. There are multiple points of non-differentiability at the center, and so this loop does not satisfy the conditions mentioned in the above theorem. Therefore, a loop is liftable, if there is at least one parametrization under which it is differentiable at every visit to the center.

We now define geometric phase using the horizontal lift defined above. For a given loop γ and a horizontal lift $\tilde{\gamma}$, the end points $\tilde{\gamma}(0)$ and $\tilde{\gamma}(1)$ are in $\mathbb{C}\mathbb{P}^2$ and therefore, there is an operator $U \in SU(3)$ such that $\tilde{\gamma}(1) = U\tilde{\gamma}(0)$. This is because, $SU(3)$ acts transitively on $\mathbb{C}\mathbb{P}^2$. The operator is not unique — there are infinitely many such operators. Through its irreducible representation in $SU(3)$, $SO(3)$ can be regarded as a subgroup of $SU(3)$.

We denote the representation as $\mathcal{D} : SO(3) \rightarrow SU(3)$. In the next section, we show that there is an $SO(3)$ choice for the operator U , i.e., there is an operator $R \in SO(3)$ with a representation $\mathcal{D}(R) \in SU(3)$ such that $\tilde{\gamma}(1) = \mathcal{D}(R)\tilde{\gamma}(0)$. However, this operator is still not unique — it has a two fold ambiguity. We clear up this ambiguity and provide a more rigorous definition in the next section. We also show that this operator is independent of the choice of $\tilde{\gamma}(0)$, and so it is well-defined for γ . We define this $SO(3)$ operator as the geometric phase of γ .

Definition 2 (Geometric Phase): If γ is a liftable loop in \mathbb{B} , its *geometric phase* is the operator $R \in SO(3)$ such that, $\tilde{\gamma}(1) = \mathcal{D}(R)\tilde{\gamma}(0)$ holds for every horizontal lift $\tilde{\gamma}$ of γ , where $\mathcal{D}(R) \in SU(3)$ is the representation of R in $SU(3)$.

In the next section, we provide an explicit way of computing the geometric phase of a given loop. Going back to the earlier described geometric picture of representing a quantum state by a spin vector and an ellipsoid centered at its tip, the end points $\tilde{\gamma}(0)$ and $\tilde{\gamma}(1)$ are two quantum states with the same spin vector but different ellipsoids; i.e., we can represent them as $\tilde{\gamma}(0) \equiv (\vec{S}, \mathbf{T}_1)$ and $\tilde{\gamma}(1) \equiv (\vec{S}, \mathbf{T}_2)$. The geometric phase of γ , we show, is precisely the rotation R which rotates the ellipsoid \mathbf{T}_1 to \mathbf{T}_2 , i.e., $\mathbf{T}_2 = R\mathbf{T}_1R^T$.

In the axis-angle representation, a right-hand rotation about a unit vector $\hat{n} \in \mathbb{R}^3$ by an angle $\theta \in [0, 2\pi)$ is represented by $R_{\hat{n}}(\theta)$. For non-singular loops, the geometric phase is $R = R_{\gamma(0)}(\Omega)$, a rotation about the spin vector $\gamma(0)$ by an angle Ω , equal to the solid angle enclosed by γ (Fig. 8.1 (b)). To see this, we need the following simple facts about the ellipsoids, which follow from Eq. 4.2. One of the eigenvectors of \mathbf{T} coincides with \vec{S} with an eigenvalue $1 - |\vec{S}|^2$. Therefore, the ellipsoid is always oriented with one axis parallel to \vec{S} (see Appendix for a detailed derivation). The other two eigenvalues are $\frac{1}{2}(1 \pm \sqrt{1 - |\vec{S}|^2})$ and that leaves only one degree of freedom for the ellipsoid when the spin vector is fixed, namely, rotation about the spin vector (Fig. 8.1 (a)). Therefore, if $\gamma(t) \neq 0$ throughout the loop, the geometric phase is necessarily a rotation about the vector $\gamma(0)$. The parallel transport of the ellipsoid is reminiscent of the parallel transport of a tangent line to S^2 along

a loop and thus the holonomy is the solid angle of the loop. Therefore, the angle of rotation of the ellipsoid is also this solid angle.

The above interpretation, however, does not work for singular loops. We provide a generalization of the above interpretation in the following section.

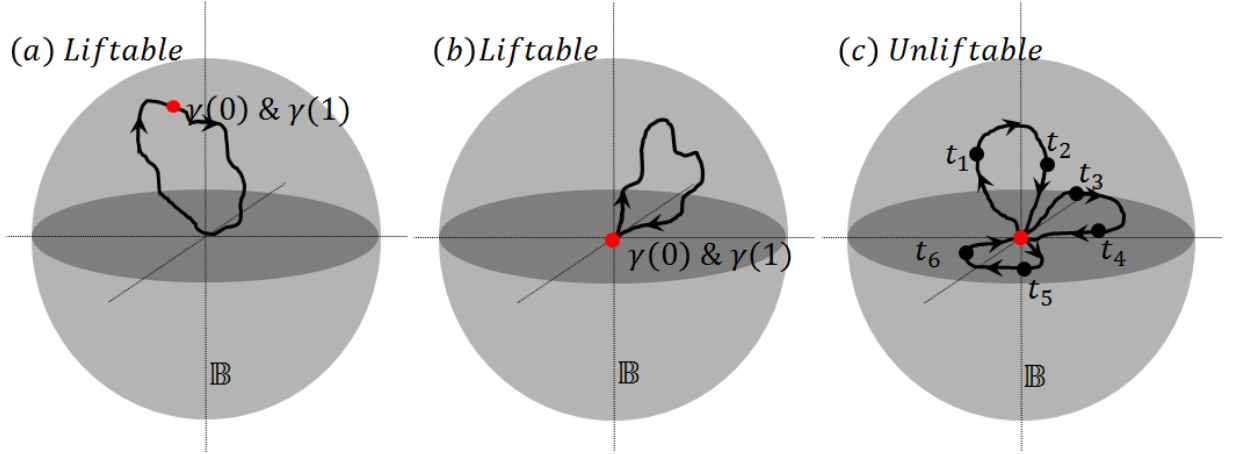


Figure 4.1: **Liftable and unliftable loops.** (a) and (b) show liftable loops and (c) shows an unliftable loop. In all three loops, the red point represents the starting and the ending point (i.e., $\gamma(0)$ and $\gamma(1)$). For the loop in (a), $\gamma^{-1}(\vec{0}) = \{t\}$ for some $t \in (0, 1)$ and the loop is differentiable at that point. The loop in (b) has a kink at zero, but with a suitable choice of the starting and ending points, it is liftable. In particular, when the starting and the ending points are chosen at the center, i.e., $\gamma^{-1}(\vec{0}) = \{0, 1\}$, $\dot{\gamma}(0)$ and $\dot{\gamma}(1)$ are both well-defined and therefore, the loop is liftable. The loop in (c) has multiple kinks at the center. Six intermediate points between 0 & 1, with the following ordering: $0 < t_1 < t_2 < t_3 < t_4 < t_5 < t_6 < 1$ are indicated to guide the reader through the loop. There is no choice of the starting and the ending points such that it is liftable. $\gamma^{-1}(\vec{0})$ has two points other than 0 & 1 and the loop is not differentiable at either of these points. Therefore, this loop is not liftable.

4.4 Interpretation of this geometric phase

We define a *generalized solid angle* for all loops inside \mathbb{B} in definition 3 below. The idea is to first project a loop in the Bloch ball onto the *real projective plane* ($\mathbb{R}\mathbb{P}^2$) and to define a solid angle for this projection. We begin with the definition of the projection.

We recall that $\mathbb{R}\mathbb{P}^2$ is the space of all lines through the origin of \mathbb{R}^3 . Equivalently, it is the space obtained from the 2-sphere S^2 by identifying diametrically opposite points. We

use the following notation for points in \mathbb{RP}^2 :

Notation: The projection of a unit vector $\hat{n} \in S^2$, to \mathbb{RP}^2 is the equivalence class $\{+\hat{n}, -\hat{n}\}$ and will be denoted by $\pm\hat{n}$.

Every loop in S^2 can be projected to a loop in \mathbb{RP}^2 . As described earlier, the solid angle of a non-singular loop can be pictured by radially projecting it to the boundary of \mathbb{B} , which is S^2 (Fig. 8.3 (a)). A singular loop can also be projected to S^2 after removing the point(s) at the center. The projected path will, however, be discontinuous (Fig. 8.3 (b)). Every time the loop crosses the center of \mathbb{B} , the projected path makes a discontinuous jump across the diameter of S^2 , parallel to the tangent of the loop at the center. This holds for all liftable loops. The discontinuity can be removed by identifying diametrically opposite points on S^2 and in doing so, we obtain an \mathbb{RP}^2 . Thus, every liftable loop γ in \mathbb{B} can be projected to a continuous path $\alpha : [0, 1] \rightarrow \mathbb{RP}^2$:

$$\alpha(t) = \begin{cases} \pm \frac{\gamma(t)}{|\gamma(t)|} & \gamma(t) \neq 0 \\ \pm \frac{\dot{\gamma}(t)}{|\dot{\gamma}(t)|} & \gamma(t) = 0 \end{cases} \quad (4.4)$$

Here, $\dot{\gamma} = \frac{d\gamma}{dt}$. Note that the projection is in general an open path.

We will next define a solid angle for paths in \mathbb{RP}^2 , as an appropriate $U(1)$ holonomy. Indeed the relevant $U(1)$ bundle over \mathbb{RP}^2 is isomorphic to the lens space $L(4, 1)$. We recall that the lens space $L(4, 1)$ is a quotient of the 3-sphere S^3 by the discrete group Z_4 action $(z_1, z_2) \mapsto (iz_1, iz_2)$, where S^3 is represented as the set of all normalized vectors in \mathbb{C}^2 , i.e.,

$$S^3 = \{(z_1, z_2) \in \mathbb{C}^2 : |z_1|^2 + |z_2|^2 = 1\}, \quad (4.5)$$

and $Z_4 = \{1, i, -1, -i\}$. Thus $L(4, 1)$ is obtained by identifying the orbits of Z_4 in S^3 ,

$$L(4, 1) = \frac{S^3}{(z_1, z_2) \sim (iz_1, iz_2)} \quad (4.6)$$

S^3 is a 4-sheet covering space of $L(4, 1)$.

The lens space $L(4, 1)$ is a $U(1)$ bundle over both \mathbb{RP}^2 and S^2 (we will show this explicitly in the next section). In fact, this is the only lens space that is a $U(1)$ bundle over \mathbb{RP}^2 [74]. The solid angle of a loop in S^2 can be defined as the $U(1)$ holonomy of its lift in $L(4, 1)$. Similarly, we define the solid angle of a loop in \mathbb{RP}^2 as the $U(1)$ holonomy of its lift in $L(4, 1)$. An important property of this solid angle is that it is preserved under the projection map from S^2 to \mathbb{RP}^2 — the solid angle of a loop in S^2 is equal to the solid angle of its projection in \mathbb{RP}^2 . We prove this in lemma 3 in the next section. The appropriate generalization of a holonomy to open paths is a *vertical displacement* [73]. The vertical displacement of the horizontal lift of a path in \mathbb{RP}^2 is a map from the fiber above the initial point of the path to the fiber above the final point of the path. Noting that $SO(3) \approx L(2, 1)$ is a double cover of $L(4, 1)$ and it acts transitively on $L(4, 1)$, the vertical displacement can be represented by an $SO(3)$ action on $L(4, 1)$, i.e., by an operator $V \in SO(3)$. We provide the details in the next section.

We now define the generalized solid angle of a loop in \mathbb{B} .

Definition 3 (Generalized Solid Angle): Let γ be a liftable loop in \mathbb{B} and let α be its projection in \mathbb{RP}^2 . If $\tilde{\alpha}$ is a horizontal lift of α in $L(4, 1)$ with a vertical displacement $V \in SO(3)$, and \hat{k} is any unit vector normal to both $\alpha(0)$ and $\alpha(1)$, the generalized solid angle (Ω) of the loop γ is given by $\Omega = \cos^{-1}(\hat{k} \cdot V\hat{k})$.

In the next section, we show that the expression $\Omega = \cos^{-1}(\hat{k} \cdot V\hat{k})$ is the correct holonomy of α when it is closed, and a meaningful definition of the solid angle of α , also when it is open. Furthermore, we also show that it is equal to the standard solid angle of γ when it is non-singular. Hence we refer to this angle as the generalized solid angle of γ . The following theorem establishes the connection between the generalized solid angle and geometric phase:

Theorem 2: If γ is a liftable loop in \mathbb{B} and α is its projection in \mathbb{RP}^2 , then the geometric phase of γ is equal to the vertical displacement of α .

Thus, the geometric phase of any loop inside \mathbb{B} can be interpreted in terms of the generalized solid angle of its projection into $\mathbb{R}\mathbb{P}^2$. This interpretation builds on the $m = 0$ geometric phases introduced in [68]. In the following section, we fill in the details of definitions 1, 2, 3 and provide proofs of theorem 1 and theorem 2. Before proceeding, we make a few remarks contrasting our geometric phase with Berry's phase. Unlike Berry's phase, our geometric phase does not arise naturally from the dynamics of the system. For any liftable loop inside \mathbb{B} , our geometric phase is well defined, regardless of how the physical system is transported along the loop. Therefore, our geometric phase is similar to the mixed state geometric phase introduced in [1] and the non-adiabatic geometric phases introduced in [14, 66]. Both of these formulations have been observed experimentally [51, 39].

4.5 Proofs of Theorem 1 and 2

The basic idea behind the proof of theorem 1 is that although $\phi : \mathbb{C}\mathbb{P}^2 \rightarrow \mathbb{B}$ does not have a fiber bundle structure, it is closely related to a fiber bundle. In fact, it can be constructed as a quotient of a fiber bundle. \mathbb{B} can be constructed as a quotient space of $S^2 \times [0, 1]$, by collapsing the sphere $S^2 \times \{0\}$ to a point. We show in lemma 2(a) below that $\mathbb{C}\mathbb{P}^2$ can also be constructed as a quotient space of $L(4, 1) \times [0, 1]$ by collapsing $L(4, 1) \times \{0\}$ and $L(4, 1) \times \{1\}$ to an $\mathbb{R}\mathbb{P}^2$ and an S^2 respectively. $L(4, 1) \times [0, 1]$ is an S^1 bundle over $S^2 \times [0, 1]$, because $L(4, 1)$ is an S^1 bundle over S^2 . Thus, $\mathbb{C}\mathbb{P}^2 \rightarrow \mathbb{B}$ can be constructed from the fiber bundle $L(4, 1) \times [0, 1] \rightarrow S^2 \times [0, 1]$. Before proceeding to state and prove lemma 2, we develop a geometrical construction of $L(4, 1)$. We show, in lemma 1, that $L(4, 1)$ is the space of all tangent lines to a unit sphere.

Lemma 1: $L(4, 1)$ is homeomorphic to the space of all tangent lines to a unit sphere and it is an S^1 bundle over both S^2 and $\mathbb{R}\mathbb{P}^2$.

Proof: A tangent line (ℓ) to a sphere is uniquely represented by the pair $\ell = (\hat{v}, \pm\hat{u})$ (Fig. 4.2(a)) of orthogonal unit vectors, \hat{v} representing the point of tangency of ℓ and \hat{u} representing the direction of ℓ . Here, $-\hat{u}$ and $+\hat{u}$ represent the same tangent line and

therefore, we use a “ \pm ” sign before \hat{u} , as a short hand for the equivalence class $\{+\hat{u}, -\hat{u}\}$. We show that the space of all tangent lines to a sphere, i.e., $\{\ell = (\hat{v}, \pm\hat{u}) : \hat{v} \cdot \hat{u} = 0\}$ is homeomorphic to $L(4, 1)$ by explicitly constructing a 4-sheeted covering map from S^3 to this space and showing that this space is also obtained as a quotient of S^3 under a Z_4 action (Eq. 4.6).

Noting that $SU(2)$ is topologically homeomorphic to S^3 and $SO(3)$ acts transitively on the space of tangent lines to a sphere, we construct a composition of the following two maps:

$$SU(2) \xrightarrow{f} SO(3) \xrightarrow{g} \{\ell = (\hat{v}, \pm\hat{u}) : \hat{v} \cdot \hat{u} = 0\} \quad (4.7)$$

f is the standard double cover from $SU(2)$ to $SO(3)$ i.e., $f : e^{i\hat{n} \cdot \vec{\sigma} \frac{\theta}{2}} \mapsto R_{\hat{n}}(\theta) \in SO(3)$, where \hat{n} is a unit vector in \mathbb{R}^3 and $\vec{\sigma} = (\sigma_x, \sigma_y, \sigma_z)$ are the Pauli matrices:

$$\sigma_x = \begin{pmatrix} 0 & 1 \\ 1 & 0 \end{pmatrix}, \quad \sigma_y = \begin{pmatrix} 0 & -i \\ i & 0 \end{pmatrix}, \quad \sigma_z = \begin{pmatrix} 1 & 0 \\ 0 & -1 \end{pmatrix} \quad (4.8)$$

The map g is constructed from the action of $SO(3)$ on the space of tangent lines to a sphere. Fixing a tangent line $\ell_0 = (\hat{z}, \pm\hat{x})$ (Fig. 4.2(a)), we obtain:

$$g : R_{\hat{n}}(\theta) \mapsto R_{\hat{n}}(\theta)\ell_0 = (R_{\hat{n}}(\theta)\hat{z}, \pm R_{\hat{n}}(\theta)\hat{x}) \quad (4.9)$$

We now show that $g \circ f : SU(2) \rightarrow \{(\hat{v}, \pm\hat{u}) : \hat{v} \cdot \hat{u} = 0\}$ is the required 4-sheet covering map. The action of $SO(3)$ on a tangent line to a sphere has a Z_2 stabilizer. For instance, the stabilizer of ℓ_0 is $\{1, R_{\hat{z}}(\pi)\}$. Therefore, g is a double covering map. For an arbitrary tangent line ℓ , the pre-image set under g contains two points in $SO(3)$. If $\ell = R_{\hat{n}}(\theta)\ell_0$, for some \hat{n} and θ , then its pre-image set is $g^{-1}(\ell) = \{R_{\hat{n}}(\theta), R_{\hat{n}}(\theta)R_{\hat{z}}(\pi)\}$. Further, $f^{-1} \circ g^{-1}(\ell)$ is a set of 4 elements in $SU(2)$ given by:

$$f^{-1} \circ g^{-1}(\ell) = e^{i\hat{n} \cdot \vec{\sigma} \frac{\theta}{2}} \{1, i\sigma_z, -1, -i\sigma_z\} \quad (4.10)$$

Thus, the pre-image set is generated by a Z_4 action and therefore, $g \circ f$ is the required covering map and $L(4, 1) \approx \{\ell = (\hat{v}, \pm\hat{u}) : \hat{v} \cdot \hat{u} = 0\}$. We can now define the bundle maps $\pi_1 : L(4, 1) \rightarrow S^2$ and $\pi_2 : L(4, 1) \rightarrow \mathbb{RP}^2$:

$$\begin{aligned}\pi_1 : (\hat{v}, \pm\hat{u}) &\mapsto \hat{v} \in S^2 \\ \pi_2 : (\hat{v}, \pm\hat{u}) &\mapsto \pm\hat{u} \in \mathbb{RP}^2\end{aligned}\tag{4.11}$$

π_1 takes every tangent line to its point of tangency, and π_2 takes every tangent line to a parallel line through the center, which is an element of \mathbb{RP}^2 . It is straight forward to verify that they are both S^1 bundle maps ■.

A natural metric on $L(4, 1)$ is induced by the round metric (i.e., the standard Cartesian metric) on S^3 . This metric, at a point $\ell = (\hat{v}, \pm\hat{u}) \in L(4, 1)$ is:

$$ds^2 = d\hat{v} \cdot d\hat{v} + d\hat{u} \cdot d\hat{u} - (\hat{v} \cdot d\hat{u})^2\tag{4.12}$$

The first term ($d\hat{v} \cdot d\hat{v}$) corresponds to the distance covered by the point of contact on S^2 . The term $d\hat{u} \cdot d\hat{u} - (\hat{v} \cdot d\hat{u})^2$ corresponds to the angle of rotation of the tangent line about its point of contact.

Using a similar argument, it can be shown that the lens space $L(2, 1)$ is the space of all unit tangent vectors to a unit sphere, i.e., $L(2, 1) \approx \{(\hat{v}, \hat{u}) : \hat{u} \cdot \hat{v} = 0\}$ (Fig. 4.2 (b)).

Lemma 2:

- (a) \mathbb{CP}^2 can be constructed from the stack $L(4, 1) \times [0, 1]$ by collapsing $L(4, 1) \times \{0\}$ to an \mathbb{RP}^2 and $L(4, 1) \times \{1\}$ to an S^2 using the respective bundle maps π_1 and π_2 . That is,

$$\mathbb{CP}^2 = \frac{L(4, 1) \times [0, 1]}{\pi}\tag{4.13}$$

where $\pi = 1$ on $L(4, 1) \times (0, 1)$, $\pi = \pi_1$ on $L(4, 1) \times \{1\}$ and $\pi = \pi_2$ on $L(4, 1) \times \{0\}$

- (b) Writing $\mathbb{B}^\circ - \{0\} = S^2 \times (0, 1)$, where \mathbb{B}° is the interior of \mathbb{B} , the restriction of ϕ to

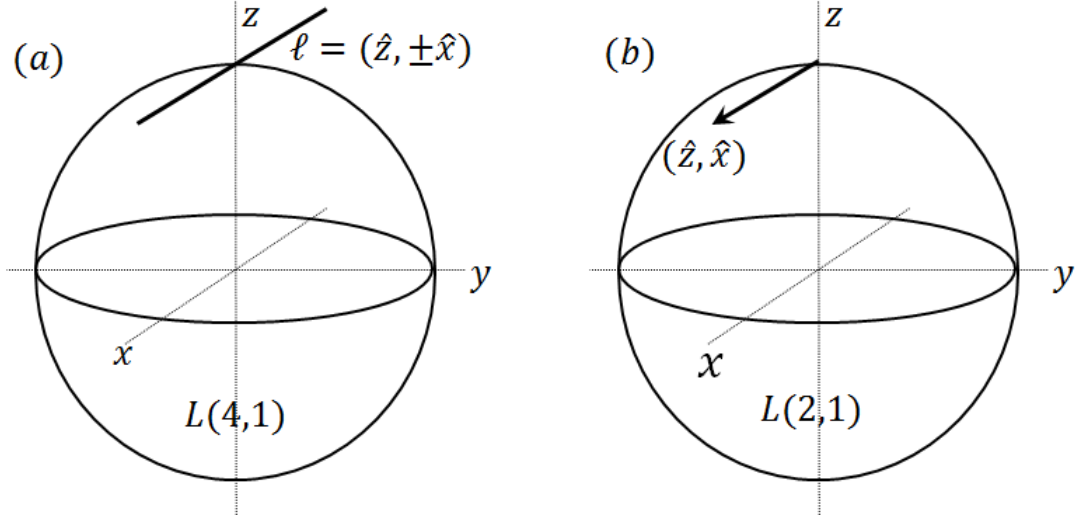


Figure 4.2: **The lens spaces $L(4, 1)$ and $L(2, 1)$.** $L(4, 1)$ is the space of all tangent lines to a sphere and $L(2, 1)$ is the space of all unit tangent vectors to a sphere. (a) shows the tangent line $\ell = (\hat{z}, \pm\hat{x}) \in L(4, 1)$, parallel to \hat{x} and touching the sphere at \hat{z} . (b) shows a unit tangent vector to a sphere $(\hat{z}, \hat{x}) \in L(2, 1)$ at \hat{z} parallel to \hat{x} .

$L(4, 1) \times (0, 1)$ is,

$$\phi = \pi_1 \times 1 : L(4, 1) \times (0, 1) \rightarrow S^2 \times (0, 1). \quad (4.14)$$

(c) $\mathbb{C}\mathbb{P}^2$ is the space of all chords to a unit sphere and ϕ maps each chord to its center.

Proof: We begin with a proof of (a). Let us consider the pre-image sets of ϕ :

$$\phi^{-1}(\vec{S}) = \begin{cases} \mathbb{R}\mathbb{P}^0 & \text{if } |\vec{S}| = 1 \\ \mathbb{R}\mathbb{P}^1 & \text{if } 0 < |\vec{S}| < 1 \\ \mathbb{R}\mathbb{P}^2 & \text{if } |\vec{S}| = 0 \end{cases} \quad (4.15)$$

This can be shown using the explicit algebraic expression of ϕ , Eq. 4.2. However, it is more illuminating to use the earlier described geometric picture of representing a point in $\mathbb{C}\mathbb{P}^2$ as a vector and an ellipsoid, i.e., (\vec{S}, \mathbf{T}) (Fig. ?? (a)). The lengths of the axes of the ellipsoid are $1 - |\vec{S}|^2$, $\frac{1}{2}(1 \pm \sqrt{1 - |\vec{S}|^2})$ (see Appendix). Therefore, its dimensions depend only on

the length of the spin vector. When $|\vec{S}| \neq 0$, one of its axes is parallel to \vec{S} . For a given spin vector with $0 < |\vec{S}| < 1$, the ellipsoid has one degree of freedom — rotation about \vec{S} , which produces the set of all quantum states with spin vector \vec{S} . This set is an \mathbb{RP}^1 , because the ellipsoid has a two fold symmetry when rotated about \vec{S} .

On the boundary of \mathbb{B} , when $|\vec{S}| = 1$, the lengths of the two transverse axes of the ellipsoid are equal and the length of the third axis is zero. Therefore, the ellipsoid degenerates into a disk perpendicular to \vec{S} . It has no degrees of freedom; it is the only quantum state with the given spin vector. Thus, the pre-image set of this spin vector is just a point i.e., \mathbb{RP}^0 .

Finally, when $|\vec{S}| = 0$, the ellipsoid again degenerates to a disk at the center of \mathbb{B} . This time, however, it has two degrees of freedom. The pre-image set $\phi^{-1}(\vec{0})$ is the space of all orientations of a disk in \mathbb{R}^3 centered at the origin. This is indeed \mathbb{RP}^2 .

It follows, now, that the pre-image set of the boundary of \mathbb{B} , i.e., $\phi^{-1}(\{\vec{S} : |\vec{S}| = 1\})$ is a sphere in \mathbb{CP}^2 . For a shell of radius $0 < r < 1$, the pre-image set is a lens space $L(4, 1)$:

$$\phi^{-1}(\{\vec{S} : |\vec{S}| = r\}) = L(4, 1) \quad 0 < r < 1 \quad (4.16)$$

To show this, we use lemma 1 and construct a bijective map from the pre-image of the shell to $L(4, 1)$. Consider the map $(\vec{S}, \mathbf{T}) \mapsto (\hat{v}, \pm \hat{u})$ where $\hat{v} = \frac{\vec{S}}{r}$ and \hat{u} is the eigenvector of \mathbf{T} normal to \vec{S} , with the smaller eigenvalue. Indeed, there is a one-one correspondence between the orientations of an ellipsoid at \vec{S} and tangent lines at \vec{S} to a sphere of radius $|\vec{S}|$. Thus, it follows from lemma 1 that the pre-image of a shell is homeomorphic to $L(4, 1)$.

We can now construct \mathbb{CP}^2 using the pre-image sets:

$$\begin{aligned} \phi^{-1}(\{\vec{S} : |\vec{S}| = 1\}) &= S^2 \\ \phi^{-1}(\{\vec{S} : 0 < |\vec{S}| < 1\}) &= L(4, 1) \times (0, 1) \\ \phi^{-1}(\vec{0}) &= \mathbb{RP}^2 \end{aligned} \quad (4.17)$$

$\mathbb{C}\mathbb{P}^2$ is therefore obtained by attaching an $\mathbb{R}\mathbb{P}^2$ and an S^2 to either ends of $L(4, 1) \times (0, 1)$. The attaching maps are easily seen to be π_1 and π_2 , using the geometric picture. Thus, $\mathbb{C}\mathbb{P}^2$ is obtained from $L(4, 1) \times [0, 1]$ by collapsing $L(4, 1) \times \{0\}$ to an $\mathbb{R}\mathbb{P}^2$ and $L(4, 1) \times \{1\}$ to an S^2 using the respective bundle maps.

(b) follows trivially from the above construction of pre-image sets. The geometrical construction of $\mathbb{C}\mathbb{P}^2$ claimed in (c) can be shown as follows. The chords passing through the center of a unit sphere form an $\mathbb{R}\mathbb{P}^2$. The chords at some distance $r \in (0, 1)$ from the center form an $L(4, 1)$ and the chords at a distance 1 from the center degenerate to points on a sphere, forming a sphere. Thus, the space of all chords to a unit sphere has the same structure as $\mathbb{C}\mathbb{P}^2$ and is homomorphic to it. ■.

Lemma 2(c) is also a consequence of Majorana constellation [75] which has been used very fruitfully to understand geometric phases [76]. States of a spin-1 system can be considered as symmetric states of a two coupled spin-1/2 systems. A spin-1/2 state is a point on a Bloch sphere (i.e., $\mathbb{C}\mathbb{P}^1$) and therefore, a spin-1 state is an unordered pair of points on the Bloch sphere (see ref. [8] for a detailed description of this representation). This is equivalent to a chord¹. ϕ maps each chord to its center.

We can represent a chord as $(r, \hat{v}, \pm\hat{u})$, where $r\hat{v}$ is the center of the chord and \hat{u} is its direction. This corresponds to a quantum state whose spin vector is $r\hat{v}$ and the ellipsoid is oriented such that the eigenvector normal to \vec{S} with the smaller eigenvalue is parallel to \hat{u} . It is straightforward to construct this quantum state $\psi \in \mathbb{C}^3$. For instance, written in the standard basis,

$$(r, \hat{z}, \pm\hat{x}) \mapsto \psi = \left(\sqrt{\frac{1-r}{2}}, 0, \sqrt{\frac{1+r}{2}} \right) \in \mathbb{C}^3 \quad (4.18)$$

Quantum states corresponding to any chord can be obtained by performing rotations on both sides of the above equation. Conversely, the chord corresponding to given quantum state can be obtained from its spin vector and fluctuation tensor, (\vec{S}, \mathbf{T}) — it is the chord

¹This picture has a generalization. $\mathbb{C}\mathbb{P}^n$ is a *unordered product* of n $\mathbb{C}\mathbb{P}^1$'s. It is the space of all unordered set of n points on a unit sphere. That is, $\mathbb{C}\mathbb{P}^n = \mathbb{C}\mathbb{P}^1 \times \dots \times \mathbb{C}\mathbb{P}^1 / \sim$ where $(r_1, \dots, r_i, \dots, r_j, \dots, r_n) \sim (r_1, \dots, r_j, \dots, r_i, \dots, r_n)$ for $r_i \in \mathbb{C}\mathbb{P}^1$. This is known as Majorana constellation.

centered at \vec{S} and oriented parallel to the largest axis of \mathbf{T} perpendicular to \vec{S} .

The Fubini-Study metric on \mathbb{CP}^2 can be applied to the space of all chords to a unit sphere. At $(r, \hat{v}, \pm \hat{u})$, the metric is:

$$ds_{FS}^2 = \frac{1}{2}(1 - \sqrt{1 - r^2})d\hat{v} \cdot d\hat{v} + \sqrt{1 - r^2}(\hat{u} \cdot d\hat{v})^2 + (1 - r^2)(d\hat{u} \cdot d\hat{u} - (\hat{v} \cdot d\hat{u})^2) + \frac{1}{4(1 - r^2)}dr^2 \quad (4.19)$$

This follows from Eq. 4.3. We now proceed to prove theorem 1.

4.5.1 Proof of theorem 1

Without loss of generality, we may assume that $\dot{\gamma}(t) \neq 0$ whenever it is well-defined. Therefore, $\gamma^{-1}(\vec{0})$ is a zero dimensional compact manifold, i.e., it is a finite set of points. Adding the end points 0 and 1 to this finite set, we obtain a set of points, $\gamma^{-1}(\vec{0}) \cup \{0, 1\} = \{a_0, \dots, a_{n+1}\}$ where, $a_i < a_{i+1}$, $a_0 = 0$ and $a_{n+1} = 1$. This set divides the loop into $n + 1$ pieces, $\gamma_j : [a_{j-1}, a_j] \rightarrow \mathbb{B}$ for $j = 1, 2, \dots, n + 1$. Each piece γ_j may start and end at the center of \mathbb{B} , but lies away from the center otherwise. That is, its interior lies away from the center, $\gamma((a_{j-1}, a_j)) \subset S^2 \times (0, 1]$. The closure of this path in $S^2 \times [0, 1]$ has a horizontal lift in $L(4, 1) \times [0, 1]$, defined using the standard theory of connections [73], because this space has a circle bundle structure over $S^2 \times [0, 1]$. We denote this horizontal lift by $\tilde{\gamma}_j : [a_{j-1}, a_j] \rightarrow L(4, 1) \times [0, 1]$. This path can be projected to \mathbb{CP}^2 by composing it with π , as shown in lemma 2(a). The idea behind this proof is to show that these projected paths can be attached continuously under the assumptions of the theorem, and the resulting path in \mathbb{CP}^2 is a lift of γ that minimizes the Fubini-Study length.

Within (a_{j-1}, a_j) , we may write $\gamma_j(t) = (\frac{\gamma_j(t)}{|\gamma_j(t)|}, |\gamma_j(t)|) \in S^2 \times (0, 1]$ where the two components represent the coordinates in S^2 and $(0, 1]$ respectively, i.e., $\frac{\gamma_j(t)}{|\gamma_j(t)|} \in S^2$ and

$|\gamma_j(t)| \in (0, 1]$. Let us define the closure of the first component as $\beta_j : [a_{j-1}, a_j] \rightarrow S^2$:

$$\beta_j(t) = \begin{cases} \frac{\gamma_j(t)}{|\gamma_j(t)|} & a_{j-1} < t < a_j \\ \lim_{t' \rightarrow a_k} \frac{\gamma_j(t')}{|\gamma_j(t')|} & t = a_k, k = j, j-1 \end{cases} \quad (4.20)$$

Note that β_j are indeed the closures of the discontinuous radial projections shown in Fig. 8.3

(b). Let $\tilde{\beta}_j$ denote a horizontal lift of β_j in $L(4, 1)$. We define paths $\tilde{\gamma}_j : [a_{j-1}, a_j] \rightarrow L(4, 1) \times [0, 1]$ as:

$$\tilde{\gamma}_j(t) = (\tilde{\beta}_j(t), |\gamma_j(t)|) \quad (4.21)$$

We next show that after projecting these paths to \mathbb{CP}^2 , i.e., $\pi \circ \tilde{\gamma}_j$ can be attached continuously at all a_j for $j = 1, 2 \dots n$. Note that $\gamma(a_j) = \vec{0}$ for $j = 1, 2 \dots n$. The end points of the two neighboring paths, $\tilde{\gamma}_j$ and $\tilde{\gamma}_{j+1}$ at a_j , projected to \mathbb{CP}^2 are given by:

$$\begin{aligned} \pi \circ \tilde{\gamma}_j(a_j) &= \pi \circ (\tilde{\beta}_j(a_j), 0) \equiv \pi_2 \circ \tilde{\beta}_j(a_j) \in \mathbb{RP}^2 = \phi^{-1}(\vec{0}) \\ \pi \circ \tilde{\gamma}_{j+1}(a_j) &= \pi \circ (\tilde{\beta}_{j+1}(a_j), 0) \equiv \pi_2 \circ \tilde{\beta}_{j+1}(a_j) \in \mathbb{RP}^2 = \phi^{-1}(\vec{0}) \end{aligned} \quad (4.22)$$

It suffices to show that the first point of the lift, $\tilde{\beta}_{j+1}(a_j)$, can be chosen such that the above two points coincide in \mathbb{CP}^2 . We begin with a simple observation; since γ is liftable, it is differentiable at a_j and it follows that ²:

$$\begin{aligned} \beta_j(a_j) &= \lim_{t \rightarrow a_j} \frac{\gamma_j(t)}{|\gamma_j(t)|} = \frac{\dot{\gamma}(a_j)}{|\dot{\gamma}(a_j)|} \\ \beta_{j+1}(a_j) &= \lim_{t \rightarrow a_j} \frac{\gamma_{j+1}(t)}{|\gamma_{j+1}(t)|} = -\frac{\dot{\gamma}(a_j)}{|\dot{\gamma}(a_j)|} \end{aligned} \quad (4.23)$$

Let $\tilde{\beta}_j(a_j) = (\beta_j(a_j), \pm \hat{u}) \in L(4, 1)$ for some \hat{u} normal to $\beta_j(a_j)$, following lemma 1. We may choose

$$\tilde{\beta}_{j+1}(a_j) = (\beta_{j+1}(a_j), \pm \hat{u}) \in \pi_1^{-1}(\beta_{j+1}(a_j)) \quad (4.24)$$

²We have used $\lim_{t \rightarrow a_k^\pm} \frac{\gamma_j(t)}{|\gamma_j(t)|} = \lim_{t \rightarrow a_k^\pm} \frac{\gamma_j(t) - \gamma_j(a_k)}{|\gamma_j(t) - \gamma_j(a_k)|} = \pm \frac{\dot{\gamma}_j(a_k)}{|\dot{\gamma}_j(a_k)|}$

This is a valid choice because \hat{u} is normal to $\beta_{j+1}(a_j)$ (this follows from $\beta_{j+1}(a_j) = -\beta_j(a_j)$). It now follows that $\pi_2 \circ \beta_j(a_j) = \pi_2 \circ \beta_{j+1}(a_j) = \pm \hat{u} \in \mathbb{RP}^2$ and therefore, $\tilde{\gamma}_j$ and $\tilde{\gamma}_{j+1}$ can be attached continuously .

It remains to show that the lift $\tilde{\gamma}$ obtained by attaching $\pi \circ \tilde{\gamma}_j$ minimizes the Fubini-Study metric. It suffices to show this for the interior of each segment $\pi \circ \tilde{\gamma}_j$, which is contained in $L(4, 1) \times (0, 1)$. Consider $\tilde{\gamma}_j(t) = (r(t), \hat{v}(t), \pm \hat{u}(t))$ as a path in the set of all chords to a unit sphere, following lemma 2(c) and using the notation $(r, \hat{v}, \pm \hat{u})$ for a chord with center at $r\hat{v}$ and in direction \hat{u} . It follows from the construction of $\tilde{\gamma}_j$ that:

$$\begin{aligned} r(t) &= |\gamma_j(t)| \\ (\hat{v}(t), \pm \hat{u}(t)) &= \tilde{\beta}_j(t) \in L(4, 1) \quad \text{and} \\ \hat{v}(t) &= \beta_j(t) \end{aligned} \tag{4.25}$$

$r(t)$ and $\hat{v}(t)$ are determined by $|\gamma_j(t)|$ and $\beta_j(t)$ respectively. The key observation is that the horizontal lift $\tilde{\beta}_j$ minimizes the length under the induced round metric on $L(4, 1)$ (Eq. 4.12) among all lifts of β_j [73], [77]. That is, $\hat{u}(t)$ is chosen so as to minimize the length of $\tilde{\beta}_j$ in $L(4, 1)$. From Eq. 4.12, it follows that $\dot{\hat{u}} \cdot \hat{u} = (\hat{v} \cdot \dot{\hat{u}})^2$ (here, $\dot{\hat{u}} = \frac{d\hat{u}}{dt}$). This is the condition for minimizing the length. From Eq. 4.19, it follows that the same condition minimizes the Fubini-Study length of $\tilde{\gamma}_j$ in $L(4, 1) \times (0, 1)$. Thus, $\tilde{\gamma}$ is a horizontal lift of γ . ■

We next demonstrate that the horizontal lift defined by minimizing the Fubini-Study metric is equivalent to the intuitive notion of parallel transport of ellipsoids inside \mathbb{B} . It is easier to use chords in \mathbb{B} , following lemma 2(c), instead of ellipsoids. Let ψ be a quantum state vector represented by the chord $(r, \hat{v}, \pm \hat{u})$. Its spin vector is $\vec{S} = r\hat{v}$. We show that for every infinitesimal change $d\vec{S}$ of the spin vector, the corresponding intuitive parallel transport of the chord also minimizes the Fubini-Study metric. $d\vec{S}$ is a 3-dimensional vector and it can be written as a superposition of \hat{v} , \hat{u} and $\hat{v} \times \hat{u}$. It suffices to consider the three cases where $d\vec{S}$ is parallel to the above mentioned three vectors separately. Let us begin

with the case $d\vec{S} = |d\vec{S}|\hat{v}$ (Fig. 4.3 (a)). Intuitively, the chord should be moved radially, parallel to itself, i.e., after parallel transport, the new chord will be $(r + |d\vec{S}|, \hat{v}, \pm\hat{u})$. From Eq. 4.19, it follows that this is consistent with the minimization of the Fubini-Study metric. When $d\vec{S}$ is perpendicular to both \hat{v} and \hat{u} , intuitively, the chord should be moved to $(r, \hat{v} + \frac{d\vec{S}}{r}, \pm\hat{u})$ — consistent with minimization of Fubini-Study metric (Fig. 4.3 (b)). Finally, when $d\vec{S}$ is parallel to \hat{u} , the chord should be parallel transported like a tangent line to the shell of radius r . Using straightforward geometry, it follows that the new chord is $(r, \hat{v} + \frac{d\vec{S}}{r}, \pm(\hat{u} - \frac{|d\vec{S}|}{r}\hat{v}))$ (Fig. 4.3 (c)). This satisfies the correct minimization condition for the Fubini-Study metric, $d\hat{u} \cdot d\hat{u} = (\hat{v} \cdot d\hat{u})^2$.

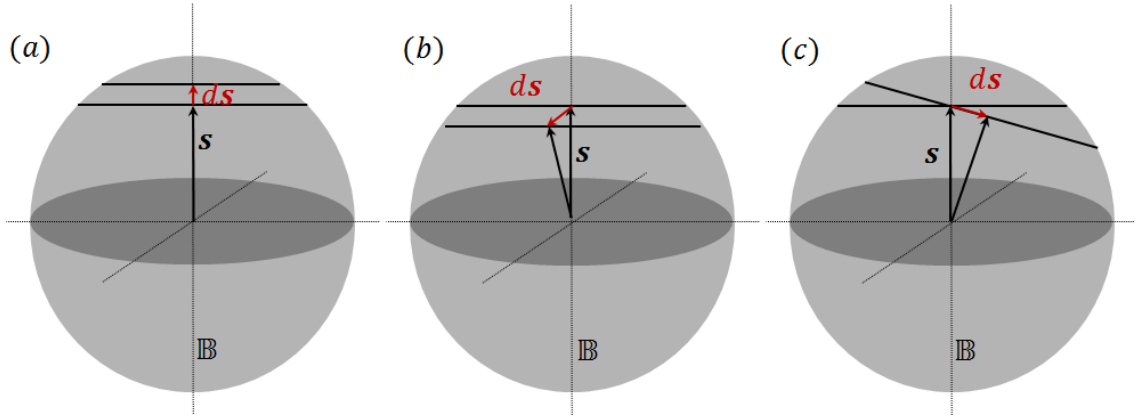


Figure 4.3: **Parallel transport.** Horizontal lifts (i.e., parallel transports) are defined by minimizing the Fubini-Study metric on $\mathbb{C}\mathbb{P}^2$, which turns out to be equivalent to the intuitive notion of parallel transport similar to tangent vectors. Quantum state vectors can be represented by chords inside \mathbb{B} . The spin vector is given by the center of the chord. Corresponding to a change $d\vec{S}$ in the spin vector, the chords can be parallel transported. (a) shows the parallel transport of the chord when $d\vec{S}$ is parallel to \vec{S} . (b) shows parallel transport of the chord when $d\vec{S}$ is perpendicular to the chord and \vec{S} . (c) shows the parallel transport when $d\vec{S}$ is parallel to the chord.

Geometric phase was defined in the previous section as the operator $R \in SO(3)$ such that $\tilde{\gamma}(1) = \mathcal{D}(R)\tilde{\gamma}(0)$ holds for all lifts $\tilde{\gamma}$ of γ . However, this operator is not unique — it has a two fold ambiguity because $\tilde{\gamma}(0)$ has a non-trivial stabilizer in $SO(3)$. For instance, when $|\vec{S}| \neq 0$, $R_{\vec{S}}(\pi)\tilde{\gamma}(0) = \tilde{\gamma}(0)$. We now use the details of the construction of $\tilde{\gamma}$ to clear this ambiguity and provide a rigorous definition of R .

Corresponding to each segment β_j in S^2 , we define a vertical displacement $R_j \in SO(3)$ such that its lift satisfies $\tilde{\beta}_j(a_j) = R_j \tilde{\beta}_j(a_{j-1})$. Here, $\tilde{\beta}_j$ is considered a path in the space of tangent lines to a sphere and R_j acts on the tangent lines as a rotation. To define R_j uniquely, we note that $SO(3) \approx L(2, 1)$ is a double cover of $L(4, 1)$. As remarked earlier, $L(2, 1)$ is the space of all unit tangent vectors to a unit sphere. $\tilde{\beta}_j$ can be lifted to $L(2, 1)$, and the end points of this lift will define a unique $R_j \in SO(3)$. For example, if $\tilde{\beta}_j(t) = (\hat{v}(t), \pm \hat{u}(t))$, we may assume without loss of generality, that $(\hat{v}(t), \hat{u}(t))$ represents a continuous path in the space of all unit tangent vectors, i.e., in $L(2, 1)$. Indeed, this is a lift of $\tilde{\beta}_j$ in $L(2, 1)$. The only other lift is $(\hat{v}(t), -\hat{u}(t))$. Both of these lifts define the same, unique vertical displacement $R_j \in SO(3)$ with

$$R_j \hat{v}(a_{j-1}) = \hat{v}(a_j) \quad \text{and} \quad R_j \hat{u}(a_{j-1}) = \hat{u}(a_j) \quad (4.26)$$

Noting that $L(4, 1)$ is a $U(1)$ bundle over S^2 , it is straightforward to show that this operator is independent of the choice of the first point, $\tilde{\beta}_j(a_{j-1})$ of the lift [73]. We now define the geometric phase as

$$R = R_{n+1} R_n \cdots R_1 \quad (4.27)$$

It follows that $\mathcal{D}(R)\tilde{\gamma}(0) = \tilde{\gamma}(1)$.

We end this section with an explicit formula to compute the horizontal lift in $\mathbb{C}\mathbb{P}^2$ and the geometric phase of a given loop in \mathbb{B} . It suffices to compute $\tilde{\beta}_j$ and R_j for each piece γ_j of the loop. Assuming that $\beta_j = \hat{v}(t)$ for $t \in [a_j, a_{j+1}]$, we are to find a $\hat{u}(t)$ such that $(\hat{v}(t), \pm \hat{u}(t))$ is a horizontal lift of β_j with a given initial point $\hat{u}(0)$. Using the minimization condition for Eq. 4.12 and $\hat{u}(t) \cdot \hat{v}(t) = 0$, it follows that $\hat{u}(t)$ is the solution to the differential equation with the given initial value:

$$\frac{d}{dt} \hat{u}(t) = - \left(\frac{d\hat{v}(t)}{dt} \cdot \hat{u}(t) \right) \hat{v}(t) \quad (4.28)$$

To find the geometric phase, we introduce $X : [a_j, a_{j+1}] \rightarrow SO(3)$ satisfying $\hat{u}(t) = X(t)\hat{u}(a_j)$, $\hat{v}(t) = X(t)\hat{v}(a_j)$ and $X(a_j) = 1$. The geometric phase will then be $R_j = X(a_{j+1})$. It is straightforward to see that $X(t)$ is the solution to the following initial value problem:

$$\begin{aligned} \frac{d}{dt}X(t) &= \left(\frac{d\hat{v}(t)}{dt}\hat{v}(t)^T - \hat{v}(t)\frac{d\hat{v}(t)^T}{dt} \right) X \\ X(a_j) &= 1 \end{aligned} \tag{4.29}$$

The above two equations, along with Eq. 4.18 provide a complete set of equations to compute the horizontal lift and the geometric phase for any loop in \mathbb{B} .

Before proving theorem 2, we make a few remarks regarding the points on the boundary of \mathbb{B} . The pre-image set of these points is trivial (Eq. 4.15). This implies that the corresponding quantum states can not carry any geometric phase information. Nevertheless, the definition of horizontal lifts and geometric phase given above are valid even for loops that visit the boundary of \mathbb{B} .

To understand what the horizontals lift and geometric phases of the class of loops that visit the boundary of \mathbb{B} mean, we note that such loops can be pushed to the interior of \mathbb{B} through infinitesimal perturbations. It is straightforward to see that the horizontal lift (geometric phase) of such loops is indeed equal to the limit of the horizontal lift (geometric phase) of the perturbed loops. Therefore, although no geometric phase can be extracted physically from this particular class of loops, for the purpose of theoretical completeness, it is possible to consistently define a geometric phase for them.

4.5.2 Proof of Theorem 2

As shown in lemma 1, $L(4, 1)$ admits two S^1 bundle structures, namely, $\pi_1 : L(4, 1) \rightarrow S^2$ and $\pi_2 : L(4, 1) \rightarrow \mathbb{R}\mathbb{P}^2$. Accordingly, loops in S^2 and loops in $\mathbb{R}\mathbb{P}^2$ both have well-defined solid angles in terms of the respective $U(1)$ holonomies. The natural projection

from S^2 to \mathbb{RP}^2 preserves the solid angle. This is the core ingredient in the interpretation of the geometric phase and the proof of theorem 2. We prove this fact in lemma 3 and then proceed to prove theorem 2. We denote the natural projection map from S^2 to \mathbb{RP}^2 by p .

Lemma 3: Let β be a piece-wise differentiable path in S^2 and $p \circ \beta$ be its projection in \mathbb{RP}^2 . The vertical displacements of the horizontal lifts of β and $p \circ \beta$ in $L(4, 1)$ are equal.

Proof: Let $\beta(t) = \hat{v}(t)$ and let $\tilde{\beta}(t) = (\hat{v}(t), \pm\hat{u}(t))$ be its horizontal lift in $L(4, 1)$. The projection of β in \mathbb{RP}^2 is $p \circ \beta = \pm\hat{v}(t)$. We first show that the path obtained by interchanging the two vectors \hat{u} and \hat{v} in $\tilde{\beta}$, i.e., $(\hat{u}(t), \pm\hat{v}(t))$, is a horizontal lift of $p \circ \beta$ in $L(4, 1)$.

From the condition $\hat{u}(t) \cdot \hat{v}(t) = 0$, it follows that $\dot{\hat{u}}(t) \cdot \hat{v}(t) + \hat{u}(t) \cdot \dot{\hat{v}}(t) = 0$. Therefore, the paths $(\hat{v}(t), \pm\hat{u}(t))$ and $(\hat{u}(t), \pm\hat{v}(t))$ have the same length in $L(4, 1)$ (see Eq. 4.12). Further, $(\hat{u}(t), \pm\hat{v}(t))$ is a lift of $p \circ \beta$ because, $\pi_2 \circ (\hat{u}(t), \pm\hat{v}(t)) = \pm\hat{v}(t) = p \circ \beta(t)$. We show, by contradiction, that it is indeed a horizontal lift. If it is not a horizontal lift, let $(\hat{u}'(t), \pm\hat{v}(t))$ be the unique horizontal lift with the initial value $\hat{u}'(0) = \hat{u}(0)$. It must have a shorter length than $(\hat{u}(t), \pm\hat{v}(t))$. It follows now that $(\hat{v}(t), \pm\hat{u}'(t))$ is a lift of β with a length shorter than $\tilde{\beta}(t) = (\hat{v}(t), \pm\hat{u}(t))$, and they have the same initial point i.e., $(\hat{v}(0), \pm\hat{u}'(0)) = (\hat{v}(0), \pm\hat{u}(0))$. This contradicts with the hypothesis that $\tilde{\beta}$ is a horizontal lift.

Thus, $p \circ \tilde{\beta} = (\hat{u}(t), \pm\hat{v}(t))$ is a horizontal lift of $p \circ \beta$. Let us now consider lifts of $\tilde{\beta}$ and $p \circ \tilde{\beta}$ in $L(2, 1)$ i.e., $(\hat{v}(t), \hat{u}(t))$ and $(\hat{u}(t), \hat{v}(t))$ respectively. It is straightforward to see that the vertical displacements are identical and is given by the unique $SO(3)$ operator V which satisfies $V\hat{v}(0) = \hat{v}(1)$ and $V\hat{u}(0) = \hat{u}(1)$. ■

We now return to prove theorem 2. Although the pieces β_j in S^2 cannot be attached continuously, their projections in \mathbb{RP}^2 can be attached continuously:

$$p \circ \beta_j(a_j) = \pm \frac{\dot{\gamma}(a_j)}{|\dot{\gamma}(a_j)|} = p \circ \beta_{j+1}(a_j) \quad (4.30)$$

This follows from Eq. 4.20. Indeed, the path obtained by attaching the segments $p \circ \beta_j$ in \mathbb{RP}^2 is α , the projection of γ defined in Eq. 4.4. From lemma 3, it follows that the vertical displacements of β_j and $p \circ \beta_j$ are equal. Thus, the vertical displacement of α is given by

$$V = R_{n+1}R_n \cdots R_1 \quad (4.31)$$

Where, R_j is the vertical displacement of β_j . This is equal to the geometric phase of γ , defined in Eq. 4.27. ■

4.6 Generalized Solid Angle

The notion of generalized solid angle was introduced through definition 3 in Section 4.4. In the following, we show that this generalized solid angle reduces to the standard solid angle for non-singular loops. Furthermore, we discuss the reasons why this definition is a meaningful generalization of solid angles for singular loops. In particular, we discuss the case when the projected path α is open in \mathbb{RP}^2 .

When γ is non-singular, its projection α is necessarily closed. We consider the following three cases separately — (i) γ is non singular, (ii) γ is singular and α is closed and (iii) γ is singular and α is an open path.

For a non-singular loop, by definition $|\gamma(t)| \neq 0$ throughout. Therefore it comprises of only one piece, i.e., $a_0 = 0$ and $a_1 = 1$. The corresponding projected path in S^2 , $\beta = \frac{\gamma}{|\gamma|}$ is closed. From lemma 3 and the definition of the geometric phase given by Eq. 4.27, it follows that the geometric phase (R) of γ is a rotation about $\beta(0)$ (or equivalently, about $\alpha(0)$) by an angle equal to the solid angle of γ . This angle is obtained by the expression $\cos^{-1}(\hat{k} \cdot R\hat{k})$ for some unit vector \hat{k} normal to $\alpha(0)$. Thus, the generalized solid angle is consistent with the standard solid angle for non-singular loops.

For a singular loop, the standard solid angle is not well-defined. However, if the projection α is closed, i.e., $\alpha(0) = \alpha(1)$, the geometric phase (i.e., the vertical displacement

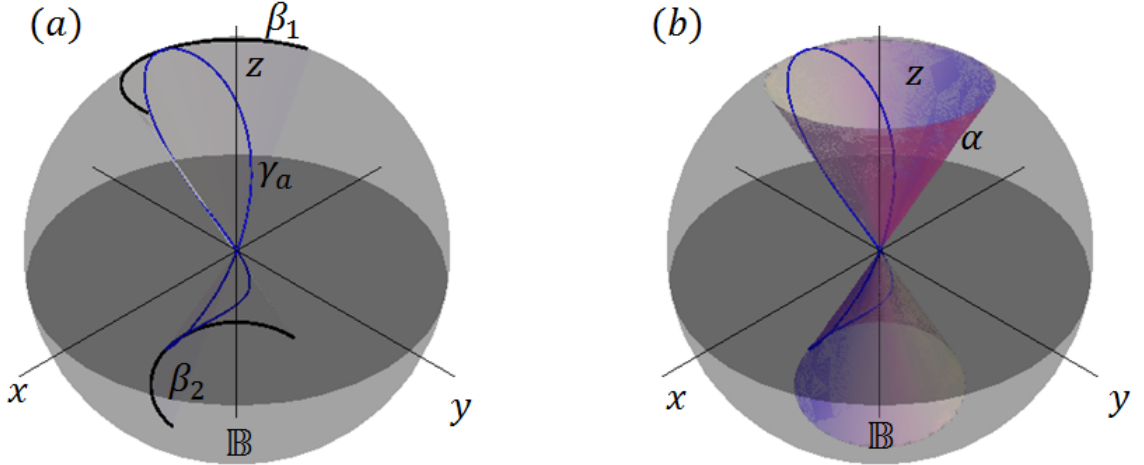


Figure 4.4: **Generalized solid angle:** (a) shows a singular loop γ_a (in blue) and the segments of its projection to S^2 , β_1 and β_2 (in black). (b) shows the projection of γ_a to $\mathbb{R}P^2$, α . Every point in $\mathbb{R}P^2$ is a diameter of S^2 and therefore, α is obtained by mapping every point on γ_a to the respective diameter of \mathbb{B} . The resulting cone is a loop in the space of diameters to S^2 , i.e., in $\mathbb{R}P^2$. Thus, the cone represents α and the generalized solid angle of γ_a is indeed equal to the solid angle of the cone.

of α) is still a rotation about $\alpha(0)$ — it maps the fiber above $\alpha(0)$ in $L(4, 1)$ to itself. Therefore, the angle of rotation about $\alpha(0)$ is well-defined and is the natural extension of solid angles to this case.

Finally, we consider the case where α is open. Fig. 4.1(b) shows one such example of a loop γ , whose projection is open in $\mathbb{R}P^2$. That is, $\gamma(0) = \gamma(1) = \vec{0}$ but $\pm \frac{\dot{\gamma}(0)}{|\dot{\gamma}(0)|} = \alpha(0) \neq \alpha(1) = \pm \frac{\dot{\gamma}(1)}{|\dot{\gamma}(1)|}$. Solid angles are well-defined for open paths in S^2 by closing them using a geodesic in [13], [12] (see also ref. [78] for an alternative formulation). We adopt a similar technique to define solid angles for open paths in $\mathbb{R}P^2$. The geometric phase (R) maps the fiber above $\alpha(0)$ to the fiber above $\alpha(1)$ in $L(4, 1)$. Indeed, it can be written uniquely as a product of two rotations, one that takes $\alpha(0)$ to $\alpha(1)$ and another that rotates about $\alpha(1)$:

$$R = R_{\alpha(1)}(\Omega_2)R_{\hat{k}}(\Omega_1) \quad (4.32)$$

where \hat{k} is a vector normal to $\alpha(0)$ and $\alpha(1)$ and Ω_1 is the angle between $\alpha(0)$ and $\alpha(1)$. The natural definition of solid angle for such a path is Ω_2 , which is given by $\cos^{-1}(\hat{k} \cdot R\hat{k})$.

CHAPTER 5

EXPERIMENTAL SYSTEM

In this chapter, we describe our experimental system and the available control operations.

5.1 Our System and Hamiltonian

Our system is a BEC of ^{87}Rb atoms trapped and cooled in a dipole trap. The outer most electron of an ^{87}Rb atom has an orbital angular momentum of $l = 0$ and a spin of $s = 1/2$. The nuclear spin is $I = 3/2$. Therefore, the total angular momentum $F = I + s$ has two sets of spin eigenstates (*i.e.*, coupled states) one with $F = 1$ and the other with $F = 2$. The hyperfine energy gap between these two is $E_{HFS} = 6.834682$ GHz, known as the clock transition.

In our experiment, the atoms remain confined to $F = 1$ level. When a magnetic field B is applied in the z direction, the Zeeman splitting within the hyperfine levels can be characterized using perturbation theory. Treating the magnetic field as a perturbation over the hyper fine splitting, we obtain

$$H = H_{HFS} + \mu_B B (g_I I_z + g_s S_z) \approx H_{HFS} + \mu_B B g_F F_z + \frac{(\mu_B B)^2}{\hbar E_{HFS}} F_z^2 \quad (5.1)$$

Here, the g 's are the landé-g factors. Since the condensate is dilute, we may assume that only 2-body collisions are significant. For N atoms, the total Hamiltonian of the system is:

$$H = \sum_{i=1}^N \left(-\frac{\hbar^2}{2m} \nabla_i^2 + V_T(\vec{r}_i) \right) + \sum_{i \neq j} \delta(\vec{r}_i - \vec{r}_j) \vec{F}_i \cdot \vec{F}_j + p \sum_{i=1}^N F_{zi} + q \sum_{i=1}^N F_{zi}^2 \quad (5.2)$$

where, $p = \mu_B B g_F$ and $q = \frac{(\mu_B B)^2}{\hbar E_{HFS}}$. We have also assumed that the collision interaction

can be modeled using a Dirac-delta function potential.

Assuming that the atoms are cooled down sufficiently close to absolute zero, we may ignore any momentum mode excitation above the zero momentum mode. In other words, we may ignore the spatial part of the Hamiltonian by writing the collective quantum state of all atoms as $\Psi(\vec{r}, t) = \phi(r)|\Psi\rangle$, where $|\Psi\rangle$ is the collective spin state of all atoms. The Hamiltonian reduces to

$$H = \tilde{c}S^2 + pS_z + qQ_{zz} \quad (5.3)$$

where, $\vec{S} = \sum_{i=1}^N \vec{F}_i$ and $Q_{zz} = \sum_{i=1}^N F_{zi}^2$. And $\tilde{c} = \frac{4\pi\hbar^2(a_2-a_0)}{3m} \int |\phi(\vec{r})|^4 d^3r$, with $a_{2,0}$ being the scattering radii. The spin state of each atom is a 3-dimensional complex vector, since it is in $F = 1$ level. Therefore, the collective spin state of N atoms, $|\Psi\rangle$ is a 3^N dimensional complex vector. Since the atoms are identical bosons in the same spatial mode, only those collective spin states which are symmetric under the exchange of atoms are permissible. The symmetric subspace of the 3^N dimensional space is an $\frac{(N+1)(N+1)}{2}$ dimensional space. The set of common eigenstates of S_z and Q_{zz} is a basis of this space:

$$\{|N_{-1}, N_0, N_{+1}\rangle : N_{-1} + N_0 + N_{+1} = N\} \quad (5.4)$$

The state $|N_{-1}, N_0, N_{+1}\rangle$ is simultaneously an eigenstate of Q_{zz} as well as an eigenstate of S_z with eigenvalues $N_{+1} + N_{-1}$ and $N_{+1} - N_{-1}$ respectively. This state is obtained by symmetrization:

$$|N_{-1}, N_0, N_{+1}\rangle = |-1, -1 \dots, 0, 0 \dots, +1, +1 \dots\rangle_{sym} \quad (5.5)$$

Another basis for the same space is the set of simultaneous eigenstates of S^2 and S_z :

$$\{|S; m\rangle : S \in \{N, N - 2 \dots\} \& m \in \{-S, -S + 1 \dots S\}\} \quad (5.6)$$

$|S; m\rangle$ is a simultaneous eigenstate of S_z and S^2 with eigenvalues m and $S(S+1)$ respecti-

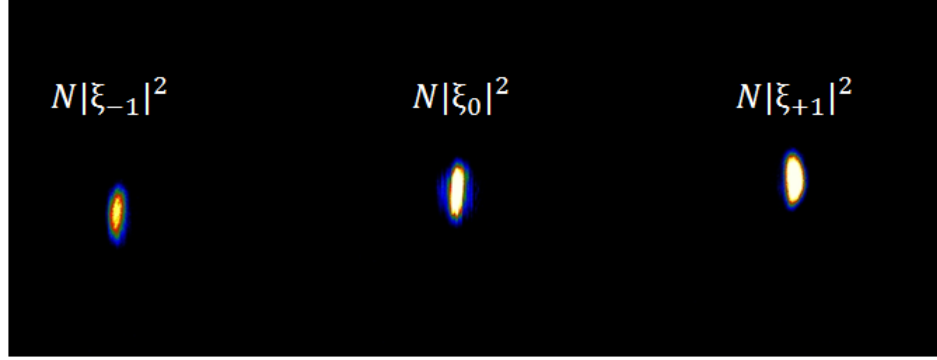


Figure 5.1: **Stern-Gerlach Measurement:** An example image of the atoms after a Stern-Gerlach separation. For a system of N atoms in a state ψ and $\xi_0 = \langle 0|\psi\rangle$, $\xi_{\pm 1} = \langle \pm 1|\psi\rangle$, the atoms numbers are expected to be $N|\xi_{\pm 1}|^2$ and $N|\xi_0|^2$.

vely. These are the well known Dicke states.

5.2 State Preparation and Stern-Gerlach Measurements

The ultracold cloud can be prepared in the $|0\rangle$ state, that is, the $m = 0$ Zeeman sub level of the $F = 1$ manifold, or in the $|-1\rangle$ state, by using a magnetic field gradient during the evaporative cooling.

Under a sufficiently strong field gradient, $m = 0$ would be the ground state of the system and the atoms would all cool down to this state. In this experiment, we initiate every experimental shot with the ultracold cloud prepared in the $|0\rangle$ state. The magnetic field gradient is produced by a pair of coils in an anti-Helmholtz configuration, which we refer to as the *gradient coils*.

The atom cloud is imaged using a fluorescence imaging technique [79]. The number of atoms in the cloud can be estimated from the counts recorded on the camera sensor.

The predominant measurement technique used in our experiment is a Stern-Gerlach measurement. The gradient coils are switched on again, at the end of the experiment, during the time of flight, when the optical trap is turned off and the atoms let to fall freely under gravity for a duration of about 20 ms. The gradient field separates the cloud into three spatially resolved clouds, consisting of those atoms that collapsed into the $|\pm\rangle$ and

$|0\rangle$ states respectively. The fluorescence image would then have three well resolved clouds, and we can estimate the atom number in each of them. For a system of N atoms in a state ψ , such a measurement would result in the three numbers $N|\langle \pm 1 | \psi \rangle|^2$ and $N|\langle 0 | \psi \rangle|^2$. In the next section, we summarize the control operations on the atoms.

5.3 Controlling the Spin of Rubidium Atoms

We use the $F = 1$ hyperfine level of ^{87}Rb atoms as the spin-1 system to observe this geometric phase. In order to induce a loop inside the Bloch sphere, one has to be able to arbitrarily control the spin vector of a spin-1 system. An arbitrary control entails an arbitrary rotation of the spin vector and an arbitrary resizing of the spin vector. In the next two sections, we describe the experimental techniques used to control the spin of ^{87}Rb atoms and provide experimental data to illustrate them, together with the effects of decoherence. We also discuss some of the techniques used to measure and control the ambient magnetic field in the system.

5.3.1 Rotating the Spin Vector

The Zeeman splitting of the $F = 1$ manifold of ^{87}Rb atoms is 702.4Hz/mG. As a result, magnetic fields as small as 1 mG can have an observable effect on the system within the timescale of 1 ms. Therefore, to suppress the effect of small magnetic fields in random direction produced by eddy currents during the experiment, we always have a sufficiently large ambient magnetic field during the experiment. In the experiment observing geometric phases, we use an ambient field of 20 mG in the z -direction. In section – we show how the ambient field is measured and controlled to a precision of < 1 mG.

At 20 mG field, the Larmor frequency is 14 kHz. Therefore, the quantum state of the system is always rotating about the z -axis at 14 kHz. All of our experiments are done in a frame rotating along with the quantum state. The spin vector can be rotated about an axis in the $x - y$ plane using a magnetic field oscillating at 14 kHz, also known as an *RF magnetic*

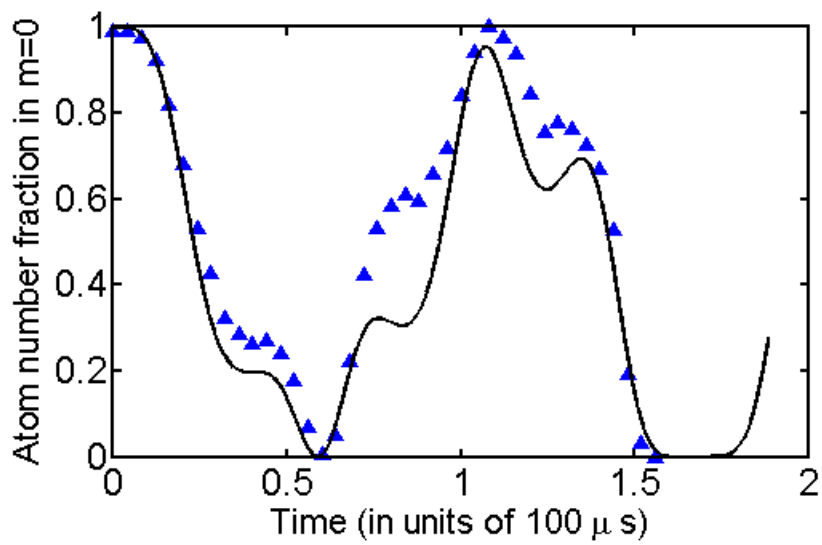


Figure 5.2: **Breakdown of RWA:** Owing to the small bias field, the Larmor rate is comparable to the RF Rabi rate. In the rotating wave approximation is not valid in such a regime [80]. The above data shows an RF Rabi under a broken RWA. The solid curve is a fit of the data to the exact solution of the Schrödinger equation, without using the RWA.

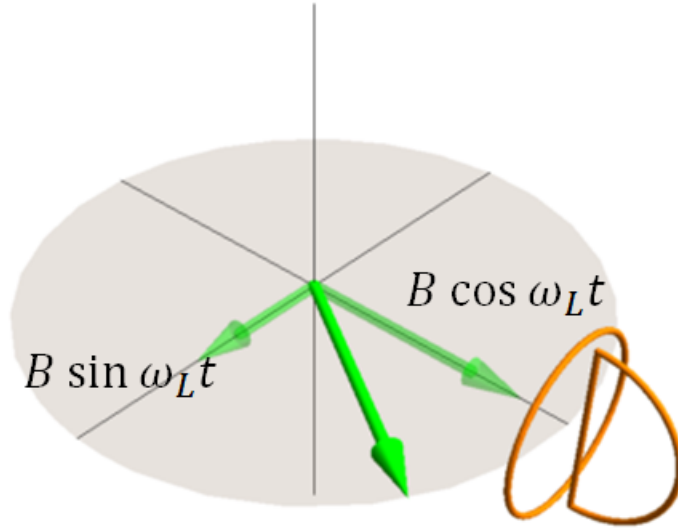


Figure 5.3: **The “OD” system of coils:** The two coils arranged in an OD format driven out of phase can produce a rotating magnetic field. The “O” coil produces a field parallel to its axis, and the straight part of the “D” coil produces a field in the orthogonal direction. When they are driven out of phase and the current amplitude is adjusted so as to produce fields of equal magnitude, the set up produces a rotating magnetic field.

field, under the rotating wave approximation (RWA). However, the validity of RWA rests on the assumption that the RF Rabi rate, i.e., the strength of the magnetic field is much smaller than the Larmor rate [80]. However, with a field of 20 mG and a Larmor rate of 14 kHz, we would not be satisfying this criterion. Therefore, our working regime is in the broken RWA, as also suggested by the data shown in Fig. 5.2.

Starting with a pure ultracold cloud prepared in the $m = 0$ Zeeman sublevel of the $F = 1$ manifold, an oscillating field was pulsed on with an ambient field of 20 mG, followed by a measurement of the atom population in $m = 0$ level using the Stern-Gerlach setup. The Larmor rate in this data was $\omega_L = 14$ kHz and the RF Rabi rate, i.e., the strength of the oscillating field was $\Omega \approx 10$ kHz. Thus, the ratio $\frac{\Omega}{\omega_L}$ is too large for the RWA to be valid [81, 82].

In order to fix the broken RWA, we introduced a second magnetic field, also oscillating

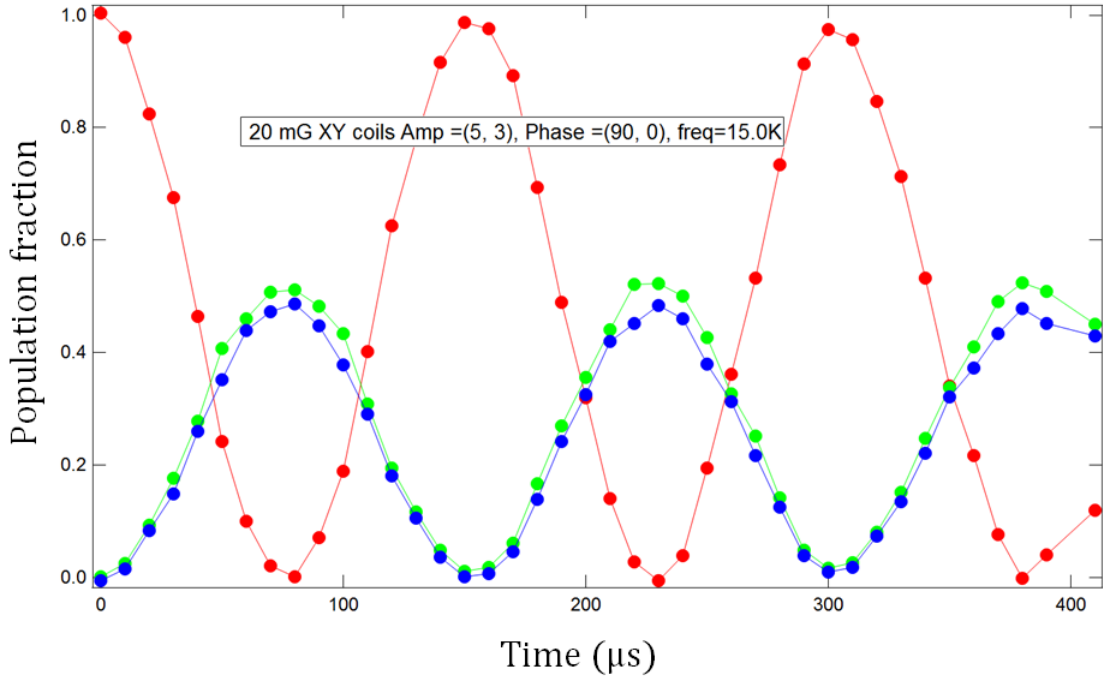


Figure 5.4: **RF Rabi from the OD coils:** The Rabi oscillations induced by a rotating magnetic field produced by the OD coils at 20 mG ambient field. The red data set shows the population in $m = 0$ Zeeman sub level. The green and the blue data sets are the populations in the $m = \pm 1$ Zeeman sub levels. The two coils were driven at 15 kHz out of phase, with peak-to-peak amplitudes 5V and 3V respectively, so as to balance the amplitudes of the produced fields. The scale on the x-axis is μs .

at 14 kHz, but out of phase with the first rotating field and orthogonal to it. When the two oscillating fields have the same strength, together, they produce a rotating magnetic field. Using a system of two coils, which we refer to as an “OD” system of coils (Fig. 5.3). Fig. 5.4 shows data set taken at 20 mG ambient field, with a rotating magnetic field generated by the OD coils.

The axis about which the spin vector of the atoms is rotated is determined by the initial phase of the two oscillating fields. The angle of rotation is determined by the pulse length. Therefore, such a rotating field can be used to rotate the system about any axis in the $x - y$ plane by any angle. This set of rotations generate $SO(3)$ (see appendix). Thus, the spin vector can be arbitrarily rotated using this technique.

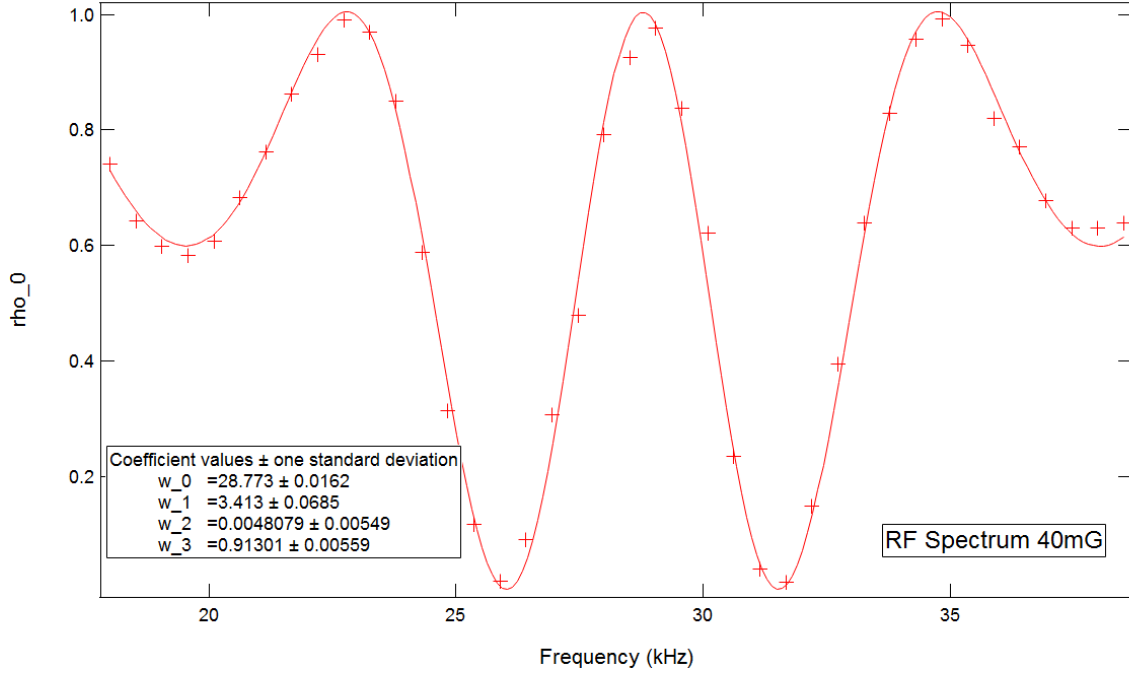


Figure 5.5: **RF Spectrum:** An experimentally obtained data set of the RF spectrum using the OD coils at an ambient field of 40 mG. The solid curve is the best fit. The fit parameters are indicated in the inset. The parameters are ω_0 (kHz), Ω (kHz), a background offset and T ($1/\pi$ ms) respectively.

The same OD system of coils can be used to measure an RF spectrum. By fixing the pulse length of the rotating field to the value that corresponds to a π rotation and varying the frequency of the rotating field, followed by a Stern-Gerlach measurement of the spin populations, we obtain an RF spectrum. Theoretically, the spin-1 RF spectrum is described by:

$$\rho_0 = \left(1 - \frac{\Omega^2}{\Omega^2 + (\omega_0 - \omega)^2} \left(1 - \cos \left(T \sqrt{\Omega^2 + (\omega_0 - \omega)^2} \right) \right) \right)^2 \quad (5.7)$$

Here, ρ_0 is the population of the $m = 0$ Zeeman sublevel. Ω is the strength of the rotating magnetic field. ω_0 is the Larmor frequency corresponding to the ambient magnetic field, i.e., the resonant frequency. ω is the frequency of the rotating field and T is the pulse length. See appendix for a derivation of this expression. Fig. 5.5 shows an example data set of the RF spectrum.

5.3.2 Resizing the Spin Vector

In this section we describe the theory and the experimental technique used to resize the spin vector. The basic idea behind resizing the spin vector is that changing the phase of $m = 0$ state relative to $m = \pm 1$. For instance, the spin vector of a nematic state, can be advanced by advancing the phase of $m = 0$ state relative to $m = \pm 1$. A typical nematic state can be written as $\psi = \frac{e^{i\phi}}{\sqrt{2}} \sin \theta | + 1 \rangle + \cos \theta | 0 \rangle - \frac{e^{-i\phi}}{\sqrt{2}} \sin \theta | - 1 \rangle$. The spin vector this state is $\vec{S} = (0, 0, 0)$. If the $|0\rangle$ is subjected to a phase shift of α relative to $|\pm 1\rangle$, the state would then be $\psi = \frac{e^{i\phi}}{\sqrt{2}} \sin \theta | + 1 \rangle + e^{i\alpha} \cos \theta | 0 \rangle - \frac{e^{-i\phi}}{\sqrt{2}} \sin \theta | - 1 \rangle$ and its spin vector would be $\vec{S} = (\sin \alpha \sin 2\theta \cos \phi, \sin \alpha \sin 2\theta \sin \phi, 0)$. It has a length $\sin 2\theta \sin \alpha$.

Therefore, the length of the spin vector of nematic states can be advanced by inducing a phase shift on the $m = 0$ component of the spin vector. A detuned microwave transition between $|F = 1, m = 0\rangle$ and $|F = 2, m = 0\rangle$ can be used to induce such a phase shift. A microwave π pulse with a detuning δ and microwave Rabi rate Ω induced a phase shift of

$$\alpha = \pi \left(1 + \frac{\delta}{\sqrt{\delta^2 + \Omega^2}} \right) \quad (5.8)$$

The angle θ in the above mentioned state ψ is essentially the angle of RF rotation of the state $|0\rangle$, in which we initiate our ultracold cloud. The length of the spin vector can be controlled using this angle and the detuning of the microwave. In the next section, we show a typical dataset, illustrating the resizing of the spin vector.

5.3.3 Measuring the Larmor Rotation

A non-zero spin vector in the $x - y$ plane can be measuring by rotating it up to the z -axis and measuring the magnetization in the z - axis. However, the spin vector in the $x - y$ plane is always rotating at the Larmor frequency. Therefore, one needs a Ramsey sequence to measure the Larmor rotation of the spin vector about the z -axis. Below is a typical Ramsey protocol that we use to observe the Larmor rotation and demonstrate the resizing

of the spin vector.

1. Start with a purified the ultracold cloud in which all atoms are in the state $\psi_1 = |0\rangle$.
2. Apply an RF pulse corresponding to a rotation by θ . This changes the state of the atoms to $\psi_2 = \frac{e^{-i\omega_L t}}{\sqrt{2}} \sin \theta | + 1 \rangle + \cos \theta | 0 \rangle - \frac{e^{i\omega_L t}}{\sqrt{2}} \sin \theta | - 1 \rangle$, in the lab frame. Here, ω_L is the Larmor frequency.
3. Apply a microwave π pulse, detuned such that it induces a phase shift of $\alpha = \pi/2$ to the $|0\rangle$ state. The state of the atoms would then be $\psi_3 = \frac{e^{-i\omega_L t}}{\sqrt{2}} \sin \theta | + 1 \rangle + i \cos \theta | 0 \rangle - \frac{e^{-i\omega_L t}}{\sqrt{2}} \sin \theta | - 1 \rangle$. This corresponds top a spin vector of length $\sin 2\theta$.
4. Let the system Larmor precess for a duration T (Ramsey wait time).
5. Apply an RF pulse corresponding to a rotation by $\pi/2$.
6. Stern-Gerlach measurement, extracting the magnetization in the z - direction.

This protocol applied with a varying Ramsey wait time (T) would produce an oscillating magnetization in the z - direction. The data is expected to be described by

$$\langle S_z \rangle (T) = \sin 2\theta \cos(\omega_L T + \phi) \quad (5.9)$$

By varying T and fitting the resulting data to the above function, we recover the length $\sin 2\theta$ of the spin vector and the Larmor frequency ω_L . Fig. 5.6 shows a typical data set obtained at a 20 mG ambient field, for various values of θ .

This illustrates the technique used to resize the spin vector. In the next section, we describe how the ambient field is measured.

5.4 Magnetic Field Measurements

In this section, we describe the theory behind measurement of the ambient magnetic field. We show a typical experimental data taken during the process of magnetic field measure-

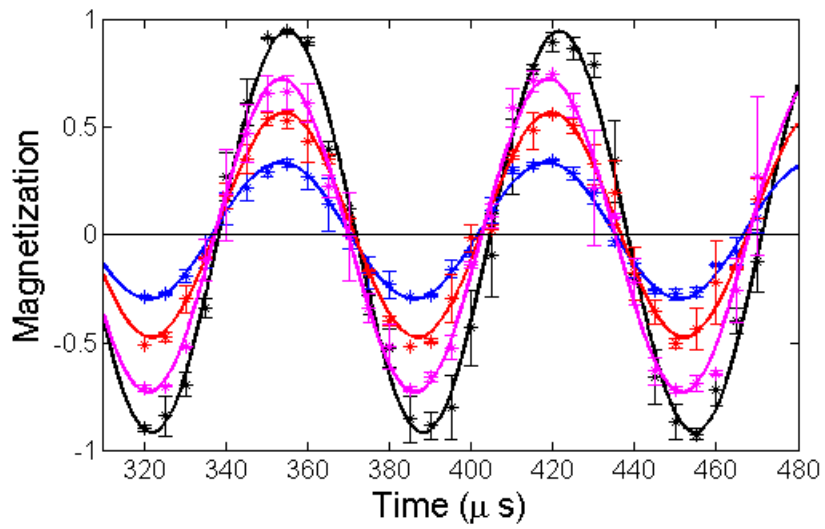


Figure 5.6: **Larmor Rotation:** Four data sets obtained through a Ramsey sequence discussed above. The amplitude of the oscillation of $\langle S_z \rangle$ is related to the initial tilt angle. The data sets in the four different colors corresponds to four different tilt angles, $\theta = \pi/16, \pi/12, \pi/6$ and $\pi/4$.

ment.

The hyperfine splitting between the $|F = 1, m = 0\rangle$ and the $|F = 2, m = 0\rangle$ is magnetically insensitive and is equal to $\Delta_0 = 6.834682$ GHz. They are also known as the clock states. The gap between $|F = 1, m = 0\rangle$ and the $|F = 2, m = +1\rangle$, however, is magnetically sensitive and is given by $\Delta_0 - |B| \times 702.4$, where $|B| = \sqrt{B_x^2 + B_y^2 + B_z^2}$ is the magnitude of the ambient field $B = (B_x, B_y, B_z)$ in mG and the 702.4 corresponds to the Zeeman splitting, 702.4 Hz/mG. By measuring a spectrum for this transition, we can obtain the magnitude of the ambient field, but not the direction. The analytical form of the spectrum is

$$\rho_{+1}(\omega) = \Omega^2 \left(\frac{\sin \left(T \sqrt{\Omega^2 + (\omega - \omega_0)^2} \right)}{\sqrt{\Omega^2 + (\omega - \omega_0)^2}} \right)^2 \quad (5.10)$$

Here, T is the microwave pulse length, Ω is the microwave Rabi rate, $\omega_0 = |B| \times 702.4$ is the resonant detuning and ω is the applied detuning. ρ_+ is the population fraction in $|F = 2, m = +1\rangle$, measured using a Stern-Gerlach.

An ambient field is the result of several sources of magnetic field such as the earth's field, various coils in the experimental set up, eddy currents, etc. In order to compensate for the ambient field, and to be able to apply any desired ambient field, we use a system of three pairs of Helmholtz coils which we refer to as *trim coils*, arranged along three orthogonal axes. By controlling the current running through these coils, we measure and manipulate the ambient magnetic field. In the next two sections, we detail how the magnetic field and its noise are measured.

5.4.1 Microwave Spectroscopy

The current running through the trim coils is controlled by an analog control channel. The current is linear in the voltage set at the control channel. The magnetic field produced by the trim coil is also linear in the current running through them. Therefore, the three control voltages, v_x, v_y, v_z linearly control the ambient magnetic field. Let us assume that the linear

conversion factors are α_x , α_y and α_z . These factors are to be experimentally determined.

As we mentioned before, using a microwave spectrum we can obtain the magnitude of the ambient field, but not the direction. In order to obtain the direction, we measure the magnitude of the ambient field with three different known offsets, applied by the three trim coils. We can determine all the three components of the ambient field this way. Quantitatively, if the ambient field is $B = (B_x, B_y, B_z)$ and a control voltage v_x is applied on the x -trim coil, the net field would be $B' = (B_x + \alpha_x v_x, B_y, B_z)$. The microwave spectrum corresponding to this setting would return a resonance peak at the magnitude of this net field. That is, the microwave resonance, ω_0 would be given by

$$\omega_0^2(v_x) = (v_x^2 \alpha_x^2 + 2\alpha_x v_x B_x + B_x^2 + B_y^2 + B_z^2) \times 702.4^2 \quad (5.11)$$

Note that this function is quadratic in v_x , which is a control parameter. The coefficients α_x , B_x and $B_y^2 + B_z^2$ can be obtained by varying v_x and fitting the obtained resonant frequencies to a parabola. By repeating this process, we can extract B_y and B_z .

Below, we illustrate this idea with an example experimental data set. Fig. 5.7 shows a set of spectra and the corresponding fit functions. Fig. 5.8 shows the corresponding parabolic fit.

Using the same technique, we measure the other two components of the magnetic field and the corresponding conversion factors α_x and α_y . Using these parameters, we can apply any magnetic field of our choice.

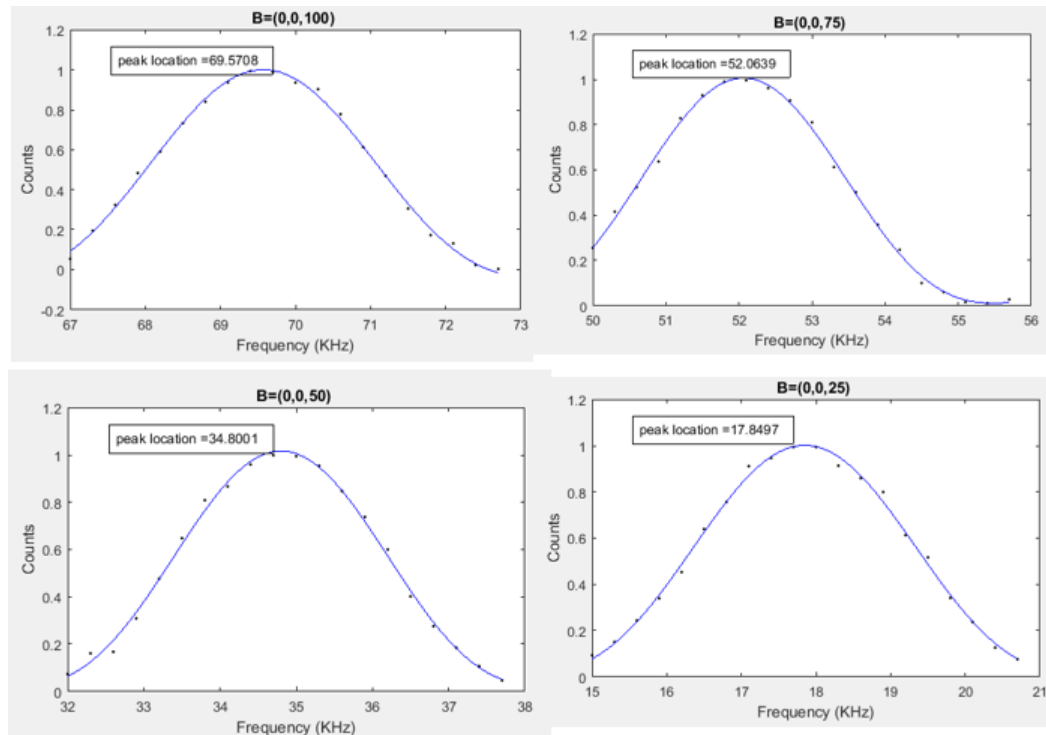


Figure 5.7: **Microwave Spectra:** A typical set of microwave spectra taken during a measurement of the z - component of the magnetic field. The four data sets correspond to four different values of v_z . The data is fit to Eq. 5.10 and the resonance peak is obtained.

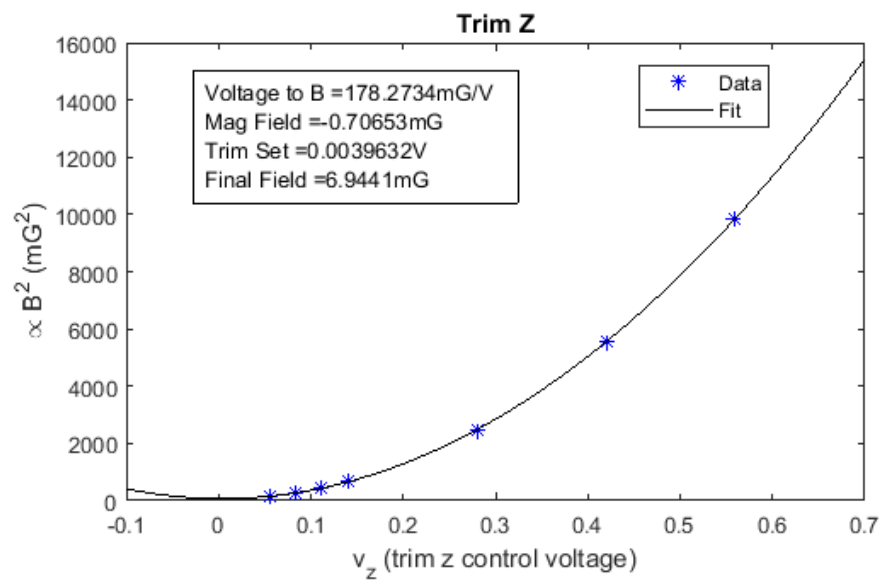


Figure 5.8: **Measuring the magnetic field:** A typical data set of the resonance peaks for various values of v_z , obtained from the fits shown in Fig. 5.7. The solid curve is fit function of the form Eq. 5.11. The fit parameters are shown in the inset. The four parameters are α_z , B_z , $-B_z/\alpha_z$ and $\sqrt{B_x^2 + B_y^2}$ in that order.

CHAPTER 6

OUR EXPERIMENT

In this chapter, we describe the experiment observing the non-Abelian geometric phases of singular loops. The material in this chapter is also available in ref. [61]. We begin with a discussion of the loops that we induce in the lab, and their geometric phase properties. Following which, we describe how these loops are induced in the lab, using the techniques outlined in chapter 5. Finally, we present the observed data.

6.1 The Loops Induced in the Lab

As discussed in chapter 4, the most non-trivial properties of our geometric phase are displayed by singular loops, i.e., those that pass through the center of the Bloch sphere. In particular, their geometric phase is non-Abelian. Accordingly, we choose a set of singular loops that are also easy to induce in the lab. Fig. 6.1 shows the set of loops that we induce in the lab. They all start and end at the center. And they are formed out of radial segments and arcs, and are therefore easy to induce in the lab with our control operations.

Before proceeding to describe the experimental sequence, we detail the geometric phase, generalized solid angle and their derivation for these loops. Recall that parallel transport of the ellipsoid (or the chord) along $\vec{S}(t)$ is a loop in the space of quantum states, which we may write $\psi(t) \equiv (\vec{S}, \pm \hat{u}(t))$, where, $\hat{u}(t)$ is a unit vector in space chosen such that it is always normal to \vec{S} and the length of $\psi(t)$ under the Fubini-Study metric is minimized. This is described by the following differential equation on $\hat{u}(t)$, as described in Chapter 3 :

$$\frac{d}{dt} \hat{u}(t) = - \left(\frac{d}{dt} \frac{\vec{S}(t)}{|\vec{S}(t)|} \cdot \hat{u}(t) \right) \frac{\vec{S}(t)}{|\vec{S}(t)|} \quad (6.1)$$

The corresponding geometric phase, i.e., the $SO(3)$ operator R is the solution to the

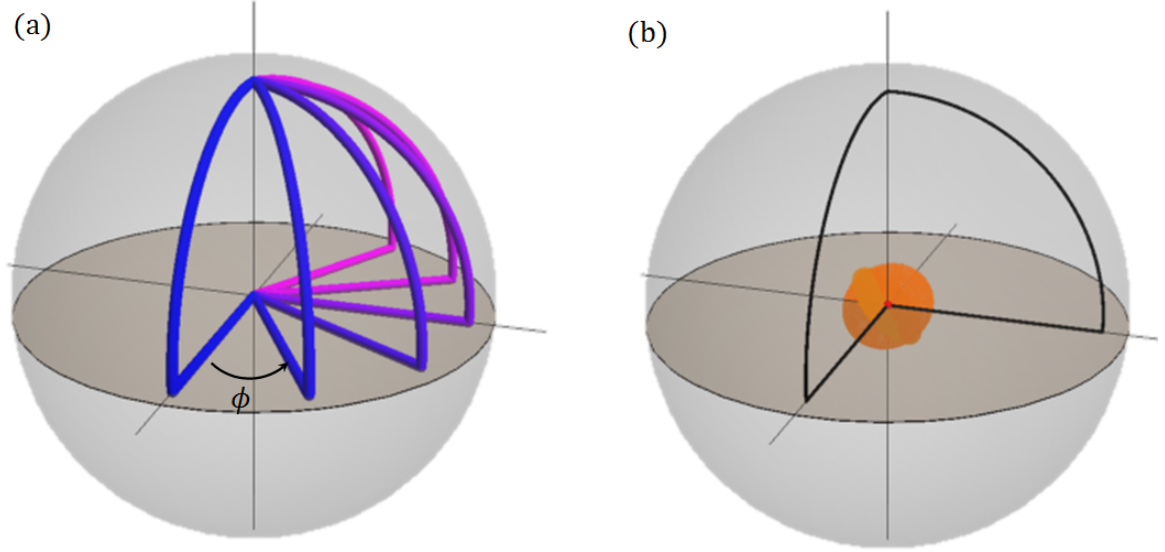


Figure 6.1: **Singular Loops Induced in the Lab:** (a) shows a set of loops that start and end at the center of the Bloch sphere. These are the loops we induce in the lab. (b) shows the orientations of an ellipsoid at the center before and after parallel transport along one of these loops. Note that the ellipsoid degenerates into a disk at the center of the Bloch sphere.

following differential equation.

$$\frac{d}{dt}X(t) = \left(\frac{d\hat{v}(t)}{dt} \hat{v}(t)^T - \hat{v}(t) \frac{d\hat{v}(t)^T}{dt} \right) X \quad (6.2)$$

$$X(0) = 1$$

As in chapter 3, $X(t)$ is a path in $SO(3)$ and $\frac{\vec{S}(t)}{|\vec{S}(t)|} = \hat{v}(t)$. The solution to this equation provides $X(t)$ and, the geometric phase of $\vec{S}(t)$ is given by $R = X(t_{final})$. Finally, the generalized solid angle is given by $\cos^{-1}(\hat{k} \cdot R\hat{k})$, where \hat{k} is some vector normal to both $\hat{v}(0)$ and $\hat{v}(t_{final})$.

Assuming that the loop goes out upto a radius r and with the parameter $t_{final} = 1$ it can

be parametrized as:

$$\vec{S}(t) = \begin{cases} (4rt, 0, 0) : 0 \leq t \leq 1/4 \\ (r \cos(2\pi(t - 1/4)), 0, r \sin(2\pi(t - 1/4))) : \\ 1/4 \leq t \leq 1/2 \\ (r \sin \phi \sin(2\pi(t - 1/2)), r \cos \phi \sin(2\pi(t - 1/2)), \\ r \cos(2\pi(t - 1/2))) : 1/2 \leq t \leq 3/4 \\ (0, 4r(1 - t), 0) : 3/4 \leq t \leq 1 \end{cases}$$

It is convenient to calculate $\hat{v}(t) = \frac{\vec{S}(t)}{|\vec{S}(t)|}$:

$$\hat{v}(t) = \begin{cases} (1, 0, 0) : 0 \leq t \leq 1/4 \\ (\cos(2\pi(t - 1/4)), 0, \sin(2\pi(t - 1/4))) : 1/4 \leq t \leq 1/2 \\ (\sin \phi \sin(2\pi(t - 1/2)), \cos \phi \sin(2\pi(t - 1/2)), \\ \cos(2\pi(t - 1/2))) : 1/2 \leq t \leq 3/4 \\ (0, 1, 0) : 3/4 \leq t \leq 1 \end{cases}$$

The solution to Eq. 6.2 are:

$$X(t) = \begin{cases} 1 : 0 \leq t \leq 1/4 \\ R_y(-2\pi(t - 1/4)) : 1/4 \leq t \leq 1/2 \\ R_z(\phi - \pi/2)R_x(-2\pi(t - 1/2))R_z(\pi/2 - \phi)R_y(-\pi/2) : \\ 1/2 \leq t \leq 3/4 \\ R_z(\phi)R_x(-\phi) : 3/4 \leq t \leq 1 \end{cases}$$

The geometric phase is $R = X(1) = R_z(\phi)R_x(-\phi)$. Explicitly, this is a 3×3 matrix:

$$R = \begin{pmatrix} \cos \phi & \sin \phi \cos \phi & 0 \\ -\sin \phi & \cos^2 \phi & -\sin \phi \cos \phi \\ 0 & \sin \phi & \cos \phi \end{pmatrix} \quad (6.3)$$

The generalized solid angle is obtained using $\hat{k} = \hat{z}$ (this is the only choice, normal to both $\hat{v}(0)$ and $\hat{v}(1)$), $\cos^{-1}(\hat{z} \cdot R\hat{z}) = \phi$.

6.2 Geometric Phase Shift and Amplitude Shift

The geometric phase, R acts on the ellipsoid at the center and changes its orientation. The ellipsoid undergoes this transformation in orientation, after it is parallel transported long one of these loops. Recall that the ellipsoid degenerates into a disk at the center of the Bloch sphere (see Fig. 6.1 (b)). Thus, in order to observe this geometric phase, we need to measure the change in orientation of the disk. Two angular parameters — the azimuthal angle of the tilted disk, and the tilt angle of the disk with respect to the $x - y$ plane characterize the orientation of the disk. Owing to the ambient field, which is set at 20 mG for this experiment, as described in chapter 5, the disk is always spinning at 14 kHz about the z -axis. Therefore, as the tilted disk spins, the uncertainty in S_x , i.e., $\langle S_x^2 \rangle$ oscillates at twice the Larmor frequency. The amplitude of this oscillation represents the tilt angle of the disk and the phase of this oscillation represents the azimuthal angle of this disk in the rotating frame.

Quantitatively, a disk with a tilt angle θ_{tilt} and an azimuthal angle ξ is represented by the quantum state vector $\psi = \frac{e^{-i(\omega_L t + \xi)}}{\sqrt{2}} \sin \theta_{tilt} | + 1 \rangle + \cos \theta_{tilt} | 0 \rangle - \frac{e^{i(\omega_L t + \xi)}}{\sqrt{2}} \sin \theta_{tilt} | - 1 \rangle$, in the lab frame. Here, ω_L is the Larmor frequency. The expectation value $\langle S_x^2 \rangle$ for this

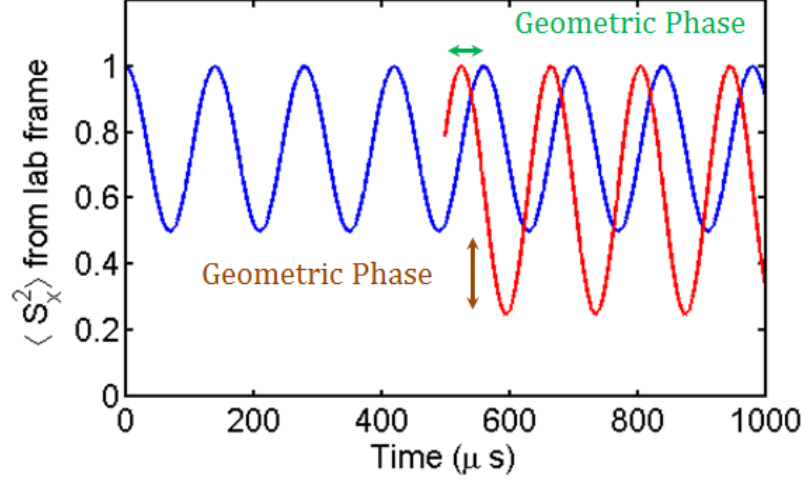


Figure 6.2: **Amplitude and Phase Shifts:** The blue curve shows the Larmor oscillation of $\langle S_x^2 \rangle$ (see Eq. 6.4), for some orientation of the disk. The red curve shows the Larmor oscillation of $\langle S_x^2 \rangle$, for the same disk, after being parallel transported along one of the loops that we induce. The change in the orientation of the disk (see Fig. 6.1(b)) manifests as a phase shift and an amplitude shift.

state is

$$\langle S_x^2 \rangle(t) = \frac{1 + \cos^2 \theta_{\text{tilt}}}{2} - \frac{\sin^2 \theta_{\text{tilt}}}{2} \cos(2\omega_L t + 2\xi) \quad (6.4)$$

The amplitude of this oscillation provides information about the tilt angle θ_{tilt} and the phase provides information about the azimuthal angle of the disk. In the geometric phase experiment, we are concerned with the change in these two angles, or equivalently, a shift in the amplitude and the phase of this oscillation. In the next section, we detail the experimental sequence and the data, observing the phase shift and the amplitude shift.

6.3 The Experiment and Data

We begin with an ultracold cloud prepared in the $|0\rangle$ state, as described in chapter 5. This is represented by a disk sitting flat at the center of the Bloch sphere. We then introduce a tilt angle, θ_{tilt} to the disk, by applying an RF field with a pulse length corresponding to a rotation by θ_{tilt} . This is the initial state in the loop. We follow this up with a transport

of the spin vector along one of the loops shown in Fig. 6.1, using a sequence of RF and microwave pulses, illustrated in Fig. 6.3. Finally, after the spin vector has been brought back to the center, we allow the final disk to precess around for a duration T and then we measure S_x^2 by applying an additional RF pulse that rotates the x axis to the z axis, followed by a Stern-Gerlach measurement, that reveals S_z^2 , which is equivalent to S_x^2 before the final RF rotation.

We repeat this sequence for various T and obtain the Larmor oscillation of S_x^2 and we refer to this data as “total phase data”. In order to obtain the geometric phase shift and the amplitude shift, we need to compare this Larmor oscillation with that of a disk that has not been parallel transported along the loop. This would be second data set as “dynamical phase data”. We use these two data sets to study the phase shift and the amplitude shift arising due to geometric phases. In the next two sections, we provide details of these two experiments.

6.3.1 Geometric Phase Shift

From Eq. 6.3, it follows that the geometric phase shift depends on ϕ , the angle included in the loop (Fig. 6.1(a)). In order to experimentally observe the phase shift for various values of ϕ , we set the tilt angle θ_{tilt} to $\pi/4$ and take data sets for six values of ϕ , $\{0, \pi/6, \pi/3, \pi/2, 2\pi/3, 5\pi/6\}$. For each of these tilt angles, we obtain two Larmor precession data sets — one for dynamical phase, without inducing the full loop and the other for geometric phase. We then obtain fit functions of the form $A \cos(\omega_L t + \xi) + B$ with parameters A, ω, ξ and B . The difference between the fit parameter values of ξ for the dynamical and the geometrical phase data sets is the geometric phase shift corresponding to the angle ϕ . We repeat this process for all the six angles and then compare the dependency of the phase shift with ϕ . Theoretically, the geometric phase shift is expected to be 2ϕ . Fig. 6.4 – 6.9 show the data and fit for the six values of ϕ . Fig. 6.10 shows the comparison between theory and experiment, of the dependence of the phase shift on ϕ .

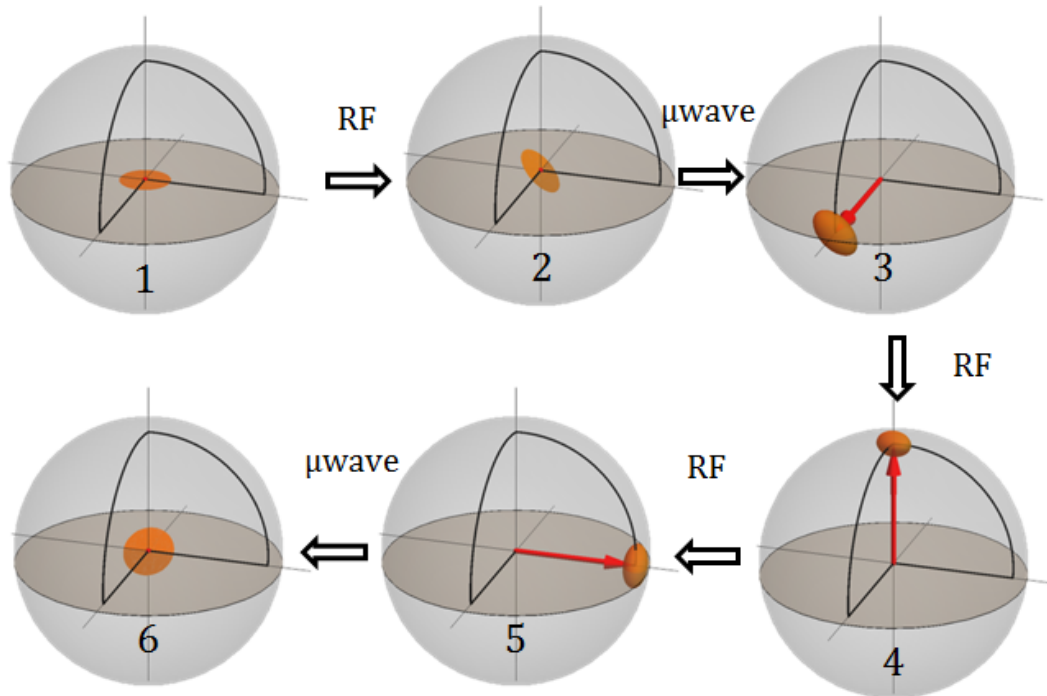


Figure 6.3: **The Experimental Sequence:** The system is prepared in the state $|0\rangle$, represented by a disk sitting flat at the center of the Bloch sphere (1 in the above figure). We use an RF pulse to tilt the disk by a desired angle. Images 2 through 6 illustrate the induction of a loop using a sequence of RF and microwave pulses. Finally a measurement of S_x^2 is made using a combination of RF and Stern-Gerlach separation.

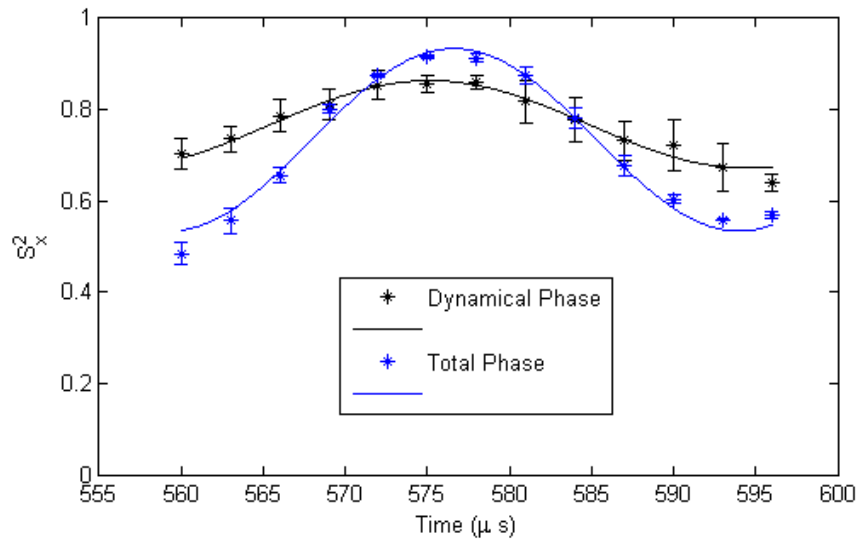


Figure 6.4: **Geometric Phase Shift:** $\phi = 0$

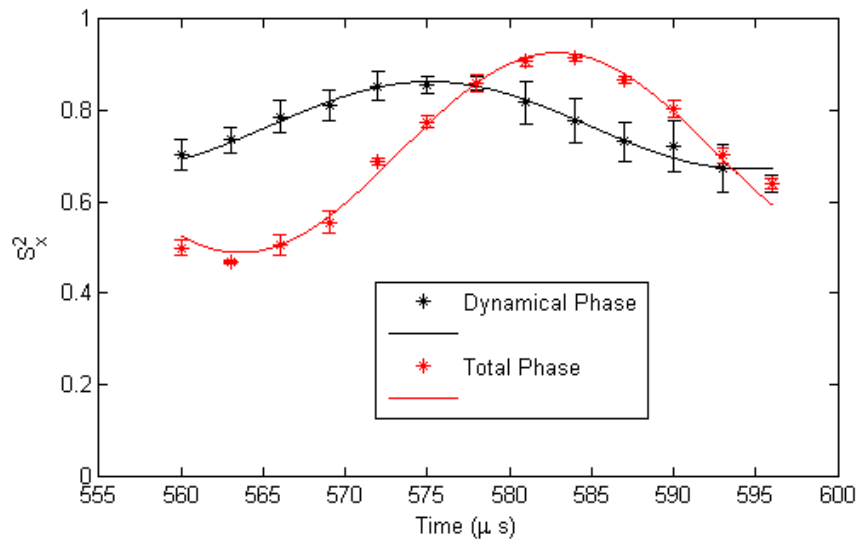


Figure 6.5: **Geometric Phase Shift:** $\phi = \frac{\pi}{6}$

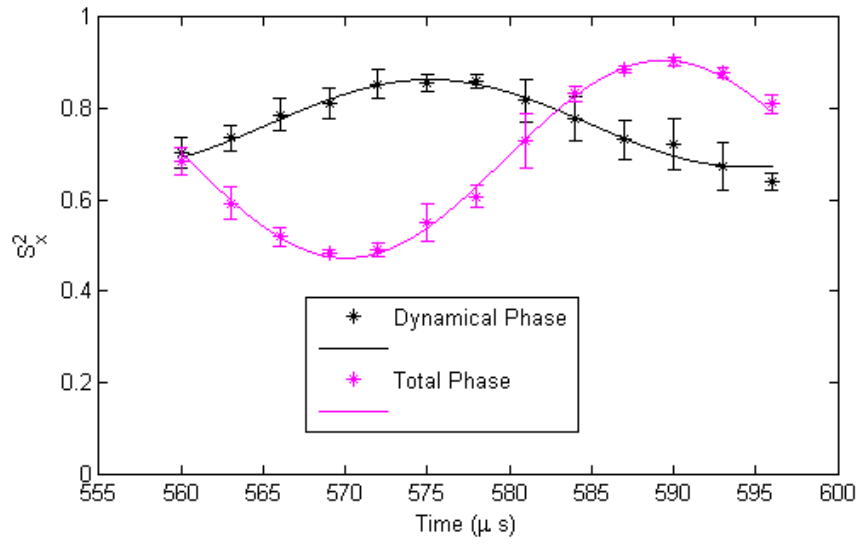


Figure 6.6: **Geometric Phase Shift:** $\phi = \frac{\pi}{3}$

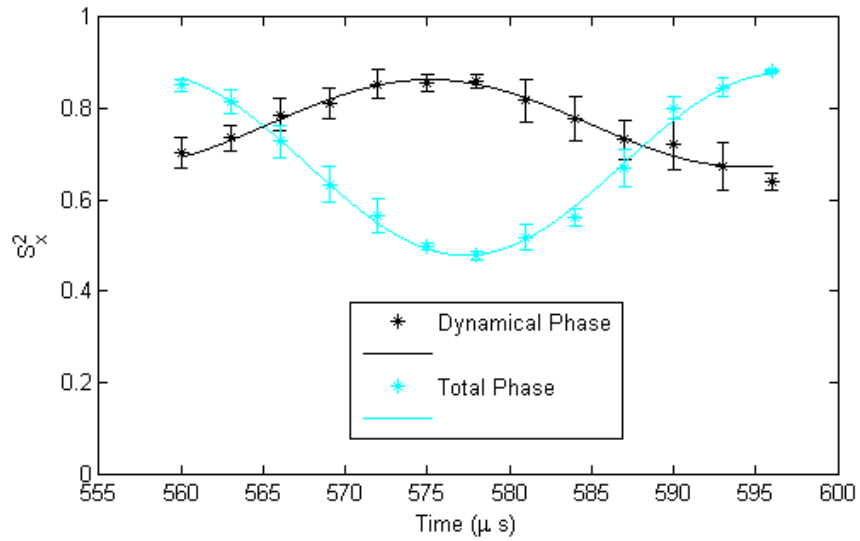


Figure 6.7: **Geometric Phase Shift:** $\phi = \frac{\pi}{2}$

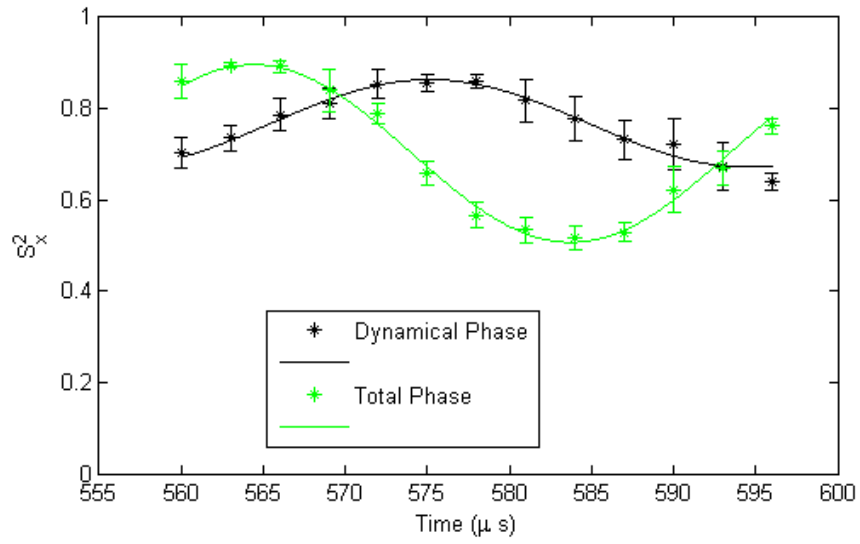


Figure 6.8: **Geometric Phase Shift:** $\phi = \frac{2\pi}{3}$

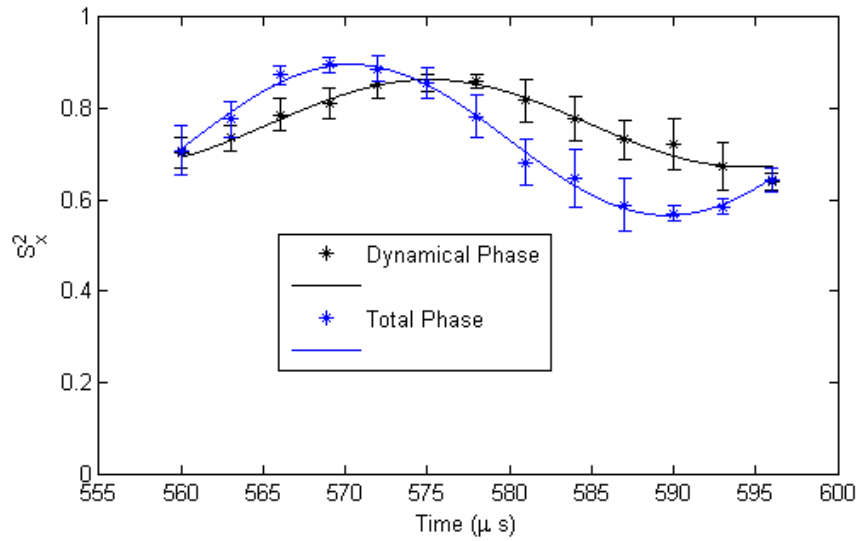


Figure 6.9: **Geometric Phase Shift:** $\phi = \frac{5\pi}{6}$

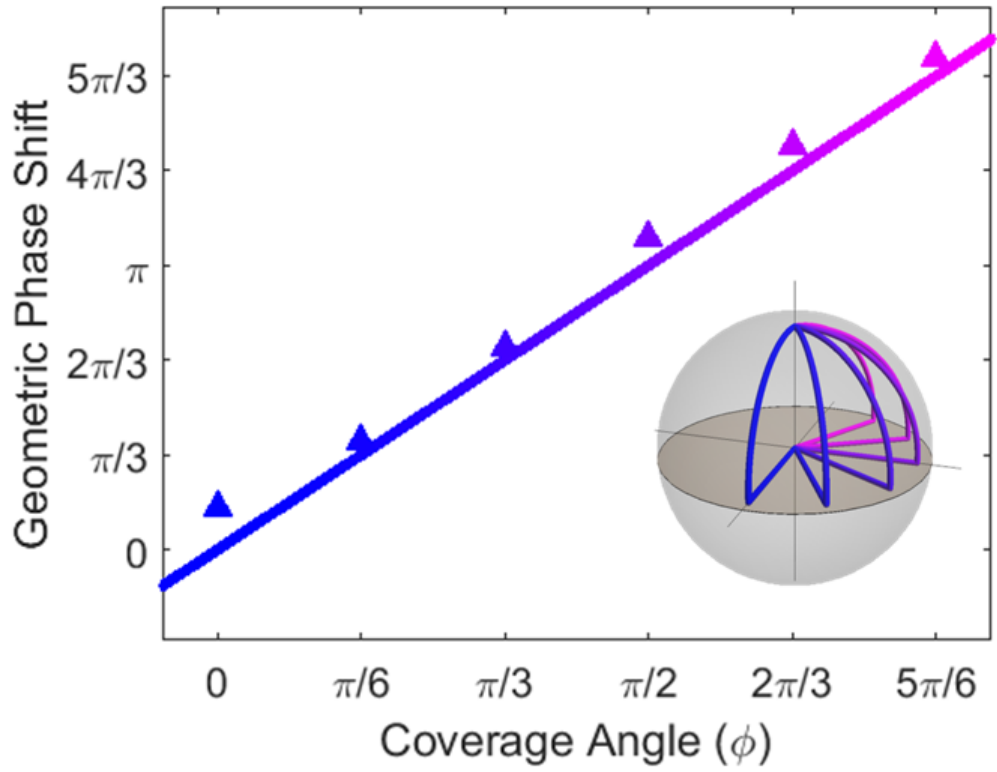


Figure 6.10: **Geometric Phase Shift:** The geometric phase shift for different values of the coverage angle (ϕ). The continuous line shows the theoretical geometric phase shift, i.e., 2ϕ . The inset shows the loops corresponding to the different values of ϕ used in the experiment.

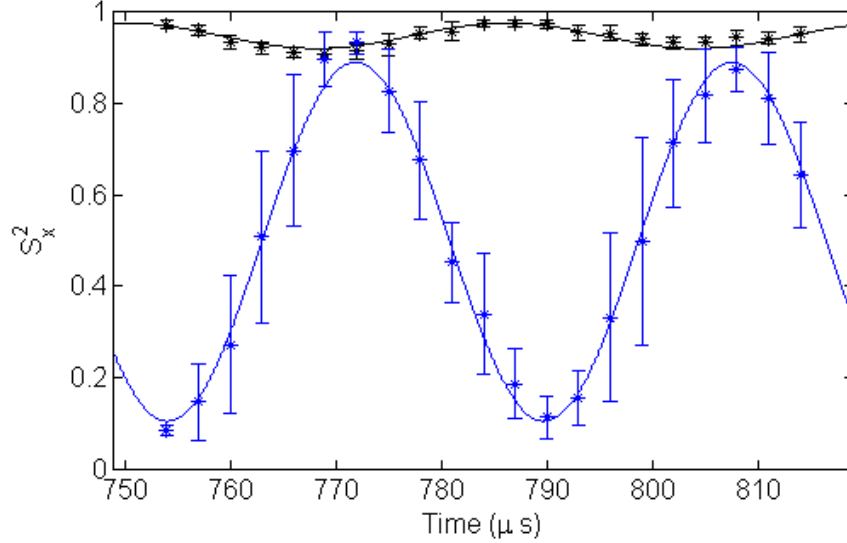


Figure 6.11: **Geometric Amplitude Shift:** $\theta_{tilt} = \pi/12$.

6.3.2 Geometric Amplitude Shift

It follows from Eq. 6.3 that the amplitude shift depends on θ_{tilt} . Therefore, in order to observe the geometric amplitude shift, we fix the angle ϕ to $\pi/4$, that is, we choose one of the loops shown in Fig. 6.1(a). We then choose five different values of θ_{tilt} , $\{\pi/12, \pi/6, \pi/4, \pi/3, 5\pi/12\}$, and obtain the two data sets for Larmor precession for each of these tilt angles, similar to the previous case. This time however, we compare the fit parameter A , that corresponds to the amplitude of the two data sets. The difference between the two amplitudes is the amplitude shift. We then obtain the amplitude shift for all of the five angles θ_{tilt} . We compare the dependence of the amplitude shift with the theoretical expression $-\frac{1}{2} \cos 2\theta_{tilt}$. Fig. 6.11 – 6.15 show the data and fit for the five values of θ_{tilt} . Fig. 6.16 shows the comparison between theory and experiment, of the dependence of the amplitude shift on θ_{tilt} .

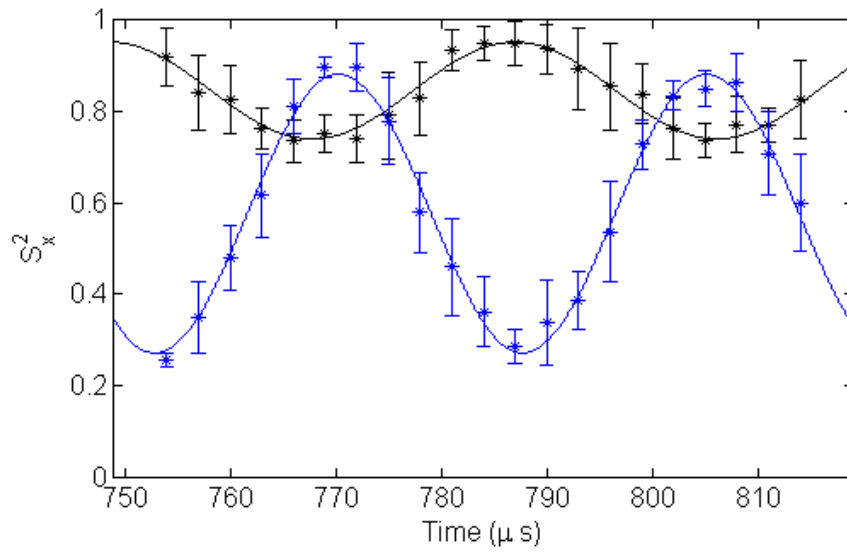


Figure 6.12: **Geometric Amplitude Shift:** $\theta_{tilt} = \pi/6$.

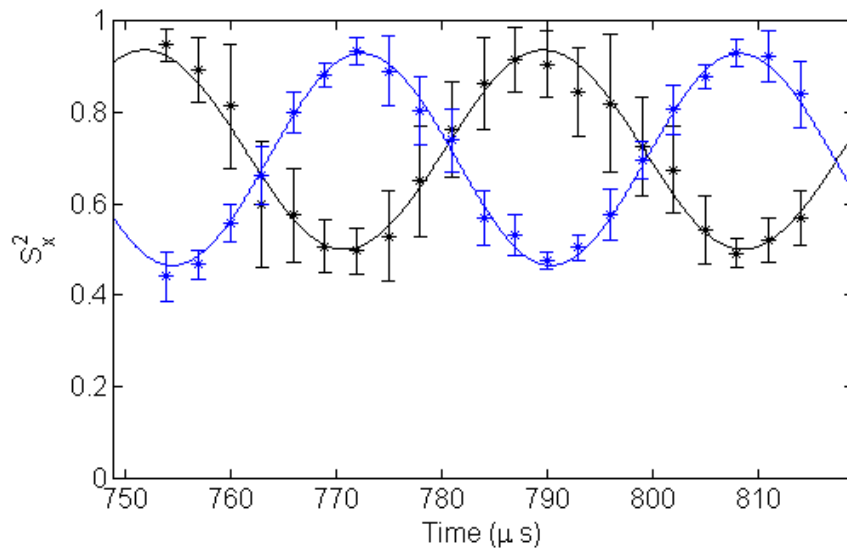


Figure 6.13: **Geometric Amplitude Shift:** $\theta_{tilt} = \pi/4$.

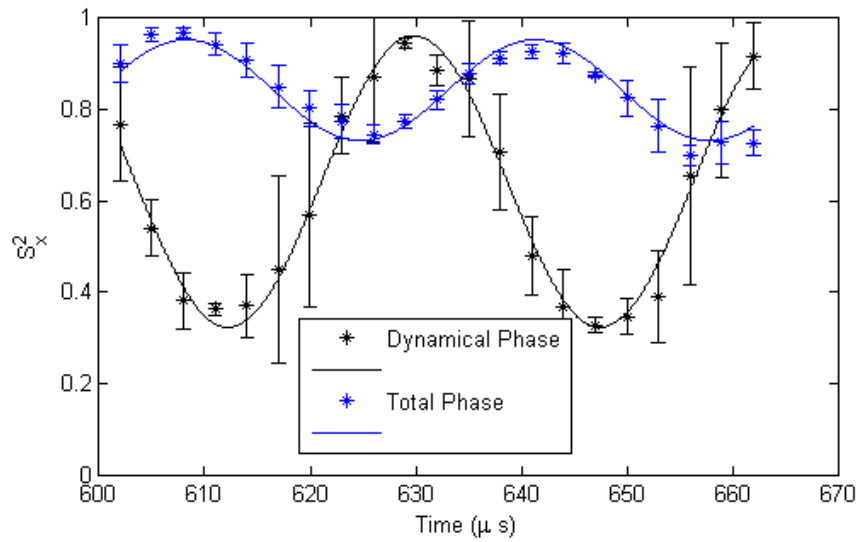


Figure 6.14: **Geometric Amplitude Shift:** $\theta_{tilt} = \pi/3$.

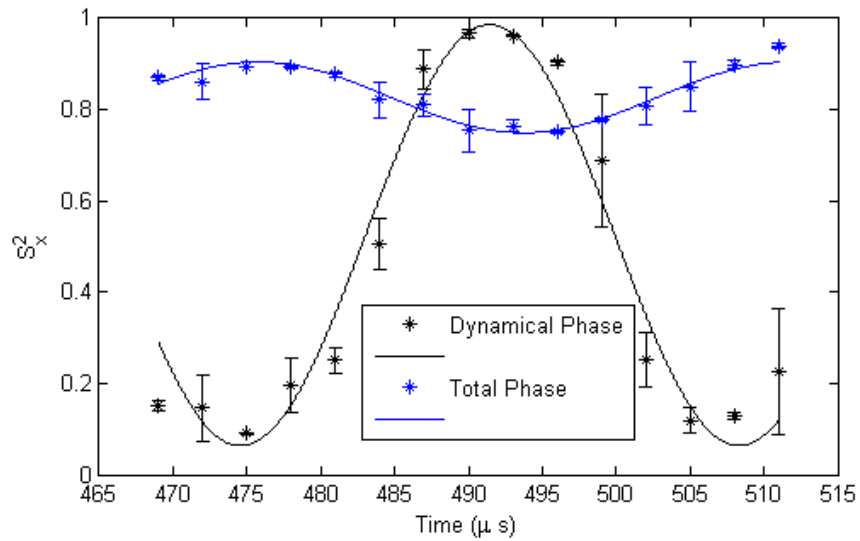


Figure 6.15: **Geometric Amplitude Shift:** $\theta_{tilt} = 5\pi/12$.

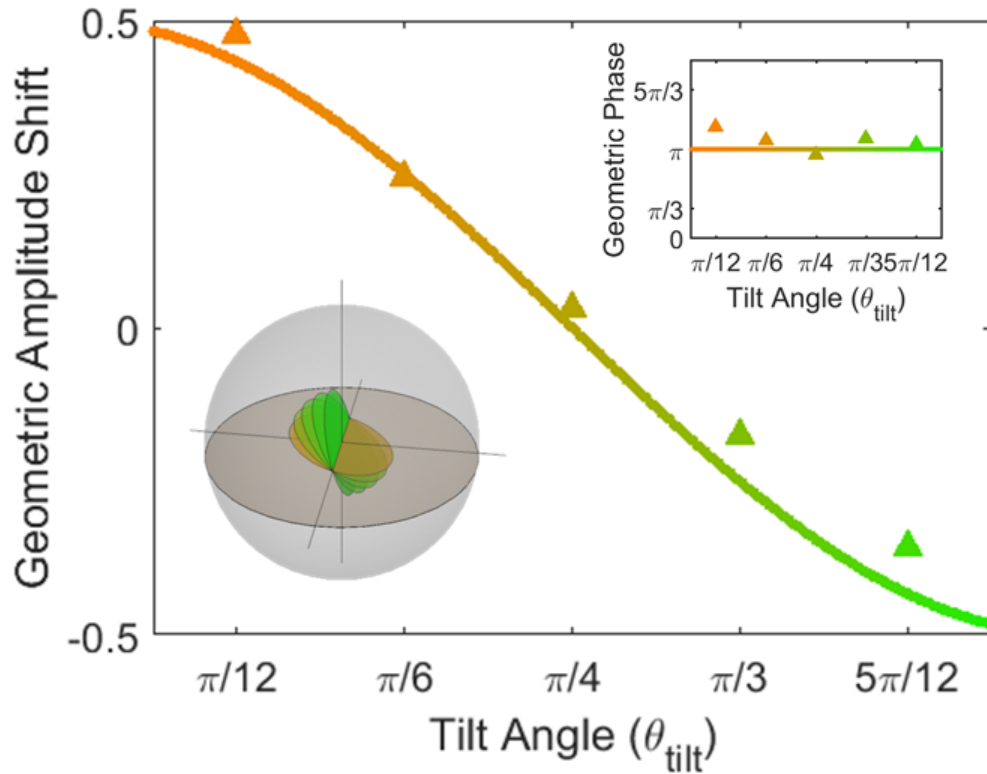


Figure 6.16: **Geometric Amplitude Shift:** A comparison with theory of the experimentally observed geometric amplitude shifts. The theoretical value of this amplitude shift is $\frac{1}{2} \cos 2\theta_{\text{tilt}}$ (continuous curve). The triangular markers show the experimentally observed amplitude shifts for different tilt angles. The inset shows the geometric phase shifts for these five tilt angles and the continuous line shows the corresponding theoretical value, i.e., π . The bottom inset shows the disks (magnified) at the starting point with different tilt angles used in the experiment.

CHAPTER 7

ARBITRARY CONTROL AND PROJECTION VALUED MEASUREMENTS OF SPIN-1 SYSTEMS

In this chapter, we theoretically develop a technique that uses only microwave/lasers to induce an arbitrary unitary operator upon a spin-1 quantum system. We further show that this technique can be used to implement an arbitrary projection valued measurement on a spin-1 quantum system. Arbitrary PVM can be used to design a single shot tomography, i.e., a tomography of the spin-1 atom cloud that does not need reloading of the atoms for additional measurements. Single shot tomography can be used to study the robustness of topologically protected states. This technique can be implemented in a BEC with the existing technology. The core idea behind this technique is a generalization of the well known Λ transitions for two level atoms. We begin with an overview of the latter in the next section and develop the theory behind the technique in the following sections.

7.1 Lambda Transitions

The lie group $SU(2)$ is the set of unitary control operations on a two level system. An arbitrary $SU(2)$ operator can be induced on a two level atom using the so called Λ transition, which employs a third excited state. Let us assume that the two levels are $|g_1\rangle$ and $|g_2\rangle$ and the third level is $|e\rangle$. We denote the energy gaps between $|g_i\rangle$ and $|e\rangle$ by ω_i for $i = 1, 2$. A Λ transition is a pair of coherently oscillating fields that couple $|e\rangle$ with $|g_1\rangle$ and $|g_2\rangle$, with the relative strengths, relative phase and detuning of the two fields designed so as to induce a given unitary $U \in SU(2)$ on the subspace spanned by $\{|g_1\rangle, |g_2\rangle\}$. Any unitary can be induced by choosing the appropriate strengths and frequencies of the oscillating fields. To prove this, we begin by solving the Schrödinger equation for the system and obtaining the unitary operator corresponding to the time evolution. The Hamiltonian of the atom, with

two oscillating fields is

$$H = \begin{pmatrix} 0 & 0 & 0 \\ 0 & -\omega_1 & 0 \\ 0 & 0 & -\omega_2 \end{pmatrix} + \begin{pmatrix} 0 & \frac{1}{2}\Omega_1 e^{-i\omega'_1 t} & \frac{1}{2}\Omega_2 e^{-i\omega'_2 t} \\ \frac{1}{2}\Omega_1^* e^{i\omega'_1 t} & 0 & 0 \\ \frac{1}{2}\Omega_2^* e^{i\omega'_2 t} & 0 & 0 \end{pmatrix} \quad (7.1)$$

Where, Ω_i are the complex amplitudes of the two fields, and ω'_i are their frequencies. Note that the second term in the above Hamiltonian can be written as

$$\begin{pmatrix} 0 & \frac{\Omega_1}{2} e^{-i\omega'_1 t} & \frac{\Omega_2}{2} e^{-i\omega'_2 t} \\ \frac{\Omega_1^*}{2} e^{i\omega'_1 t} & 0 & 0 \\ \frac{\Omega_2^*}{2} e^{i\omega'_2 t} & 0 & 0 \end{pmatrix} = \begin{pmatrix} 1 & 0 & 0 \\ 0 & e^{i\omega'_1 t} & 0 \\ 0 & 0 & e^{i\omega'_2 t} \end{pmatrix} \begin{pmatrix} 0 & \frac{\Omega_1}{2} & \frac{\Omega_2}{2} \\ \frac{\Omega_1^*}{2} & 0 & 0 \\ \frac{\Omega_2^*}{2} & 0 & 0 \end{pmatrix} \begin{pmatrix} 1 & 0 & 0 \\ 0 & e^{-i\omega'_1 t} & 0 \\ 0 & 0 & e^{-i\omega'_2 t} \end{pmatrix} \quad (7.2)$$

We can therefore consider a rotating frame where the Hamiltonian is time independent. In such a frame,

$$H = \begin{pmatrix} 0 & \frac{1}{2}\Omega_1 & \frac{1}{2}\Omega_2 \\ \frac{1}{2}\Omega_1^* & -\delta_1 & 0 \\ \frac{1}{2}\Omega_2^* & 0 & -\delta_2 \end{pmatrix} \quad (7.3)$$

Here, $\delta_i = \omega_i - \omega'_i$. Considering only those cases where $\delta_1 = \delta_2 = \delta$ is found to suffice to induce an arbitrary $SU(2)$ operator. Under this condition, we may rewrite the effective Hamiltonian as

$$H = \begin{pmatrix} \delta & \frac{1}{2}\Omega_1 & \frac{1}{2}\Omega_2 \\ \frac{1}{2}\Omega_1^* & 0 & 0 \\ \frac{1}{2}\Omega_2^* & 0 & 0 \end{pmatrix} \quad (7.4)$$

The unitary induced by this Hamiltonian, in the rotating frame is $U = e^{-iHt}$. The simplest way of evaluating this unitary is to determine the spectral decomposition, i.e., eigenstructure of H . It is straightforward to see that one of the eigenvalues of H is zero and the

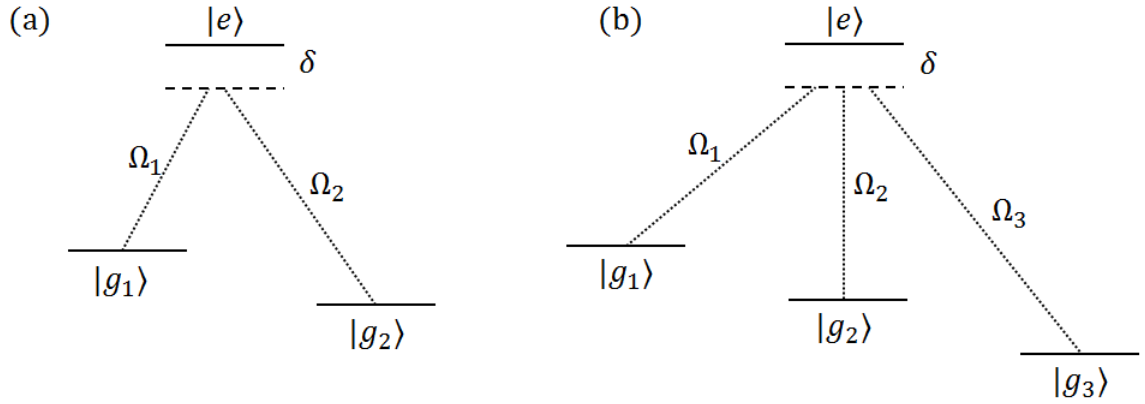


Figure 7.1: **Lambda and tripod transitions:** (a) shows the setting in a Λ transition and (b) shows the setting in a tripod transition.

corresponding eigenstate, also known as the *dark state* $|D\rangle$, is given by

$$|D\rangle = \frac{1}{\Omega} (\Omega_2|g_1\rangle - \Omega_1|g_2\rangle) \quad (7.5)$$

Where $|\Omega_1|^2 + |\Omega_2|^2 = \Omega^2$. Note that this state lies in the subspace spanned by $\{|g_1\rangle, |g_2\rangle\}$.

We refer to the state orthogonal to the dark state, within this subspace, as the *bright state*;

it is given by $|B\rangle = \frac{1}{\Omega}(\Omega_1^*|g_1\rangle + \Omega_2^*|g_2\rangle)$. The other two eigenstates of H are

$$\begin{aligned} |\psi_+\rangle &= \cos\frac{\theta}{2}|e\rangle + \sin\frac{\theta}{2}|B\rangle \\ |\psi_-\rangle &= \sin\frac{\theta}{2}|e\rangle - \cos\frac{\theta}{2}|B\rangle \end{aligned} \quad (7.6)$$

Where, the angle θ is defined by $\sin\theta = \frac{\Omega}{\sqrt{\Omega^2 + \delta^2}}$ and $\cos\theta = \frac{\delta}{\sqrt{\Omega^2 + \delta^2}}$. The eigenvalues are $\lambda_{\pm} = \frac{\delta}{2} \pm \frac{\sqrt{\delta^2 + \Omega^2}}{2}$. The bright state can be written as

$$|B\rangle = \sin\frac{\theta}{2}|\psi_+\rangle - \cos\frac{\theta}{2}|\psi_-\rangle \quad (7.7)$$

Thus, we can understand the action of the unitary e^{-iHt} on a vector within the subspace spanned by $\{|g_1\rangle, |g_2\rangle\}$, or, equivalently the subspace spanned by $\{|D\rangle, |B\rangle\}$. More preci-

sely,

$$\begin{aligned} e^{-iHt}|D\rangle &= |D\rangle \\ e^{-iHt}|B\rangle &= e^{-i\lambda+t} \sin \frac{\theta}{2} |\psi_+\rangle - e^{-i\lambda-t} \cos \frac{\theta}{2} |\psi_-\rangle \end{aligned} \quad (7.8)$$

Note that while $|D\rangle$ remains unchanged, the time evolution of $|B\rangle$ excites atoms to the level $|e\rangle$. In the basis $\{|D\rangle, |B\rangle, |e\rangle\}$, the above equation can be rewritten as

$$e^{-iHt}|B\rangle = \left(\sin^2 \frac{\theta}{2} e^{-i\lambda+t} + \cos^2 \frac{\theta}{2} e^{-i\lambda-t} \right) |B\rangle + \cos \frac{\theta}{2} \sin \frac{\theta}{2} (e^{-i\lambda+t} - e^{-i\lambda-t}) |e\rangle \quad (7.9)$$

There are some special values of t at which the population in the excited state $|e\rangle$ disappear. These are precisely, $t_n = \frac{2n\pi}{\sqrt{\delta^2 + \Omega^2}}$, when $e^{-i\lambda+t} = e^{-i\lambda-t}$. These are interesting because, at such times, the subspace spanned by $\{|D\rangle, |B\rangle\}$ remains invariant under the propagator — this propagator acts as an $U(2)$ operator over this subspace. The action of this $U(2)$ operator is captured by:

$$\begin{aligned} e^{-iHt_n}|D\rangle &= |D\rangle \\ e^{-iHt_n}|B\rangle &= e^{-in\pi} e^{-i\frac{n\pi\delta}{\sqrt{\delta^2 + \Omega^2}}} |B\rangle \end{aligned} \quad (7.10)$$

Thus, the two oscillating fields pulsed on for a duration t_n has the effect of selectively imparting a phase shift on the bright state $|D\rangle$. The phase shift and the state $|D\rangle$ can both be arbitrarily controlled. This freedom, in effect, covers the entire of $SU(2)$, as we describe below.

The product of the eigenvalues of an element of $U \in SU(2)$ is always unity. Therefore, in its eigenbasis, the matrix representing U can be written as

$$U = \begin{pmatrix} e^{-i\phi} & 0 \\ 0 & e^{i\phi} \end{pmatrix} \quad (7.11)$$

If the eigenstates of U are $|\psi_1\rangle$ and $|\psi_2\rangle$, then, $U|\psi_1\rangle = e^{-i\phi}|\psi_1\rangle$ and $U|\psi_2\rangle = e^{i\phi}|\psi_2\rangle$. By choosing Ω_1 and Ω_2 such that $|D\rangle = |\psi_2\rangle$ and the detuning δ such that the phase shift $-n\pi(1 + \frac{\delta}{\sqrt{\delta^2 + \Omega^2}}) = 2\phi$ for some conveniently chosen n , we generate a unitary e^{-iHt_n} related to U as $e^{-iHt_n} = e^{i\phi}U$, i.e., differing only by a global phase factor.

Thus, up to a global phase factor, an arbitrary $SU(2)$ operator can be induced by choosing Ω_1, Ω_2 and δ appropriately. In ref. [83], it has been shown that this scheme is holonomic, i.e., the induced $SU(2)$ operator can be viewed as the Wilczek-Zee phase of an appropriate loop. In the next section we show that this idea is generalizable to all higher dimensional system.

7.2 Tripod Transition

We show that for a three level atom, with energy eigenstates $|g_1\rangle, |g_2\rangle$ and $|g_3\rangle$, an available excited state $|e\rangle$, we can induce an arbitrary $SU(3)$ operator, using three coherently oscillating fields. We refer to this scheme as a *tripod* transition. Further we show that in an n level atom with an excited state available, an arbitrary $SU(n)$ operator can be induced using n coherently oscillating fields. The same setting — n coherently oscillating fields can be used to perform an arbitrary projection valued measurement on the system.

We set up this case similar to the previous section: the gap between $|g_i\rangle$ and $|e\rangle$ is ω_i , and the three rotating fields have amplitudes Ω_1, Ω_2 and Ω_3 . They are all detuned from the respective resonances by the same value δ . Eq. 7.4, for this case would be:

$$H = \begin{pmatrix} \delta & \frac{1}{2}\Omega_1 & \frac{1}{2}\Omega_2 & \frac{1}{2}\Omega_3 \\ \frac{1}{2}\Omega_1^* & 0 & 0 & 0 \\ \frac{1}{2}\Omega_2^* & 0 & 0 & 0 \\ \frac{1}{2}\Omega_3^* & 0 & 0 & 0 \end{pmatrix} \quad (7.12)$$

This system also has a bright state and is given by

$$|B\rangle = \frac{1}{\Omega} (\Omega_1^*|g_1\rangle + \Omega_2^*|g_2\rangle + \Omega_3^*|g_3\rangle) \quad (7.13)$$

Here, $\Omega^2 = |\Omega_1|^2 + |\Omega_2|^2 + |\Omega_3|^2$. In contrast with the previous case, this system has two dark states, $|D_1\rangle$ and $|D_2\rangle$, both orthogonal to the bright state. The rest of the arguments is similar and the propagator e^{-iHt_n} is characterized by

$$\begin{aligned} e^{-iHt_n}|D_{1,2}\rangle &= |D_{1,2}\rangle \\ e^{-iHt_n}|B\rangle &= e^{-in\pi} e^{-i\frac{n\pi\delta}{\sqrt{\delta^2+\Omega^2}}} |B\rangle \end{aligned} \quad (7.14)$$

Thus, e^{-iHt_n} is an element of $U(3)$ with two of its eigenvalues equal. In its eigenbasis, it can be written as

$$e^{-iHt_n} = \begin{pmatrix} 1 & 0 & 0 \\ 0 & 1 & 0 \\ 0 & 0 & e^{-i\left(n\pi + \frac{n\pi\delta}{\sqrt{\delta^2+\Omega^2}}\right)} \end{pmatrix} \quad (7.15)$$

An arbitrary unitary $U \in U(3)$, in its eigenbasis can be written as

$$U = \begin{pmatrix} e^{i\phi_1} & 0 & 0 \\ 0 & e^{i\phi_2} & 0 \\ 0 & 0 & e^{i\phi_3} \end{pmatrix} \quad (7.16)$$

It can be factored as

$$U = \begin{pmatrix} e^{i\phi_1} & 0 & 0 \\ 0 & 1 & 0 \\ 0 & 0 & 1 \end{pmatrix} \begin{pmatrix} 1 & 0 & 0 \\ 0 & e^{i\phi_2} & 0 \\ 0 & 0 & 1 \end{pmatrix} \begin{pmatrix} 1 & 0 & 0 \\ 0 & 1 & 0 \\ 0 & 0 & e^{i\phi_3} \end{pmatrix} \quad (7.17)$$

In other words, every element of $U(3)$ is a product of unitaries with two of its eigenvalues equal to 1, and can be individually induced using a tripod transition. Therefore, a set of

three tripod transitions in succession can be used to induce an arbitrary unitary; a set of two tripod transitions in succession can be used to induce an arbitrary element of $SU(3)$. Experimentally, such a scheme has been recently implemented in ref. [84]. It is straightforward to see that this technique generalized beyond three level systems. In the next section, we show that a modified version of this technique can be used to perform an arbitrary PVM on the system.

7.3 Arbitrary Projection Valued Measurements

In a system of N three level atoms, in a state $|\psi\rangle$, measuring the population in the state $|g_1\rangle$ would return $N|\langle g_1|\psi\rangle|^2$. This is called measuring a projection of the state onto $|g_1\rangle$. More generally, this would be called a one-dimensional projection valued measurement (PVM). Measuring the population in $|g_2\rangle$ would return $N|\langle g_2|\psi\rangle|^2$ and is another example of a 1-dimensional PVM. There are infinitely many 1-d PVMs; for instance, if we could measure a projection onto the state $\frac{|g_1\rangle - |g_3\rangle}{\sqrt{2}}$, that would return $N|\langle \frac{|g_1\rangle - |g_3\rangle}{\sqrt{2}}|\psi\rangle|^2$, and would also be an example of a 1-d PVM. More generally, corresponding to every normalized state $c_1|g_1\rangle + c_2|g_2\rangle + c_3|g_3\rangle$, there is a 1-d PVM. The set of the most general form of measurement, known as a positive operator valued measures (POVMs) is a convex set and its extreme points are precisely the 1-d PVMs. Therefore, it can be generated by the 1-d PVMs. Accordingly, measuring an arbitrary 1-d PVM would be a useful technique.

In this section, we show how to perform an arbitrary PVM on a three level system using a tripod transition. Indeed, this technique can also be generalized to higher dimensional systems. We return to the time evolution of the bright and the dark states under three coherently oscillating fields:

$$\begin{aligned}
e^{-iHt}|D_{1,2}\rangle &= |D_{1,2}\rangle \\
e^{-iHt}|B\rangle &= \left(\sin^2 \frac{\theta}{2} e^{-i\lambda_+ t} + \cos^2 \frac{\theta}{2} e^{-i\lambda_- t} \right) |B\rangle + \cos \frac{\theta}{2} \sin \frac{\theta}{2} (e^{-i\lambda_+ t} - e^{-i\lambda_- t}) |e\rangle
\end{aligned}
\tag{7.18}$$

Recall that θ is defined by $\sin \theta = \frac{\Omega}{\sqrt{\Omega^2 + \delta^2}}$ and $\cos \theta = \frac{\delta}{\sqrt{\Omega^2 + \delta^2}}$. In contrast with the previous two sections, in this section, we choose the special times t'_n at which the coefficient of $|B\rangle$ in the above equation vanishes. This is possible only if $|\sin \frac{\theta}{2}| = |\cos \frac{\theta}{2}|$, that is, when $\delta = 0$. The special times are $t'_n = \frac{(2n+1)\pi}{\Omega}$, and the action of $e^{-iHt'_n}$ is described by

$$\begin{aligned} e^{-iHt'_n} |D_{1,2}\rangle &= |D_{1,2}\rangle \\ e^{-iHt'_n} |B\rangle &= e^{i(2n+1)\frac{\pi}{2}} |e\rangle \end{aligned} \tag{7.19}$$

Thus, the unitary propagator selectively transfers the state $|B\rangle$ to $|e\rangle$. This means, if we pulse on a tripod field for a duration t'_n on a system of N atoms in a state $|\psi\rangle$, and measure the number of atoms in the excited state $|e\rangle$, the result would be $N|\langle B|\psi\rangle|^2$ — a 1-d PVM, that projects onto $|B\rangle$. The bright state can be chosen to be arbitrary, it is given by $|B\rangle = \frac{1}{\Omega}(\Omega_1^*|g_1\rangle + \Omega_2^*|g_2\rangle + \Omega_3^*|g_3\rangle)$. We can design any 1-d PVM by appropriately choosing the relative strengths and phases of the three oscillating fields.

As is clear, this idea works for an n -level atoms for any n . While this technique is itself quite valuable, in the next section, we show that it can be used to design a protocol for a *single-shot tomography*.

7.4 Single Shot Tomography

In ultracold atoms, the standard Stern-Gerlach measurement is destructive. That is, it destroys the state after revealing the populations in the respective Zeeman sublevels. Subsequently, in order to measure any other parameter, such as the relative phase between the Zeeman sublevels, one has to reload the atoms in the trap, reinitiate them in the same state. Thus, a tomography would require multiple re-initiations i.e., multiple experimental *shots*. This precludes demonstration of the stability of certain topological quantum numbers to random noise, since the latter cannot be duplicated during the re-initiation. In the PVM protocol described above, while the bright state is destroyed during a measurement, the

dark states remains unaffected and can be subjected to a subsequent PVM, extracting a second parameter of the system. Based on this idea, we develop two examples of a single-shot tomography protocol where, given a sufficiently large number of atoms, one can perform a tomography with a single experimental shot.

7.4.1 Protocol -1 : single shot tomography of nematic states.

In this protocol, we consider nematic states; i.e., the states with a zero spin vector, discussed in chapter 1 and show how a tomography of such states can be performed using a single shot. Nematic states are a two parameter family and can be parametrized as $\psi = \frac{e^{-i\phi}}{\sqrt{2}} \sin \theta | - 1 \rangle + \cos \theta | 0 \rangle - \frac{e^{-i\phi}}{\sqrt{2}} \sin \theta | + 1 \rangle$ with $0 \leq \phi \leq 2\pi$ and $0 \leq \theta \leq \pi$. The three unknown parameters of the system are the total number of atoms N , and the angles θ, ϕ . We provide the following protocol, using a tripod based PVM, to extract all the three parameters in a single shot:

1. A 1-d PVM that projects onto $|B_1\rangle = | - 1 \rangle$. This measurement would return $\alpha_1 = \frac{N}{2} \sin^2 \theta = N |\langle B_1 | \psi \rangle|^2$ and leave the remaining $\frac{N}{2}(1 + \cos^2 \theta)$ atoms in the state $\psi_1 = \cos \theta | 0 \rangle - \frac{e^{-i\phi}}{\sqrt{2}} \sin \theta | + 1 \rangle$, which is in the dark state manifold for this PVM.
2. A 1-d PVM that projects onto $|B_2\rangle = \frac{1}{\sqrt{2}}(| - 1 \rangle - | 0 \rangle)$. The outcome of this measurement would be $\alpha_2 = N |\frac{e^{-i\phi}}{\sqrt{2}} \sin \theta - \cos \theta|^2$ and leaves the remaining atoms $N |\frac{e^{-i\phi}}{\sqrt{2}} \sin \theta - \cos \theta|^2$ in the orthogonal state $\psi_2 = \frac{1}{\sqrt{2}}(| - 1 \rangle + | 0 \rangle)$
3. A measurement of the remaining number of atoms, revealing $\alpha_3 = N |\frac{e^{-i\phi}}{\sqrt{2}} \sin \theta - \cos \theta|^2$.

Using α_1, α_2 and α_3 , one can recover the three parameters N, θ and ϕ . It is straightforward to see that

$$\begin{aligned} N &= \alpha_1 + \alpha_2 + \alpha_3 \\ \cos \theta &= \sqrt{1 - \frac{2\alpha_1}{N}} \\ \cos \phi &= \frac{\alpha_3 - \alpha_2}{4\sqrt{\alpha_1(N - 2\alpha_1)}} \end{aligned} \quad (7.20)$$

Thus, without having to re-initiate the atoms in the same state, we can extract all the unknowns of the system, provided it is in a nematic state. Note that this protocol does not use a Stern-Gerlach separation at any stage. In the next section, we develop a more general protocol that uses Stern-Gerlach to perform a single-shot tomography of arbitrary states.

7.4.2 Protocol-2 : single shot tomography of arbitrary states.

This protocol is more general than the previous one — it can be used on any state, not necessarily nematic states. Given that \mathbb{CP}^2 is a four dimensional manifold, i.e., an arbitrary spin-1 state has four unknowns, a tomography experiment needs to extract five unknown parameters, including the total number of atoms, N . The basic idea is similar to the previous protocol. However, it uses tripod transitions with pulse lengths that are half of t'_n , those used in a 1-d PVM. Such tripod pulses transfer only half the population in the bright state to the excited state $|e\rangle$, leaving the other half behind.

Let us assume that the quantum state is $\psi = z_{-1}| - 1\rangle + z_0|0\rangle + z_{+1}| + 1\rangle$ with $|z_{-1}|^2 + |z_0|^2 + |z_{+1}|^2 = 1$ and that the system has N atoms. The unknowns are N, z_0, z_{-1} and z_{+1} . In the following protocol, we show how all of these parameters can be extracted in a single experimental shot.

1. A tripod transition with a bright state $|B_1\rangle = | - 1\rangle$, and a pulse length of $t'_1/2$, transferring only half the number of atoms in $|B_1\rangle$ to $|e\rangle$, followed by a destructive measurement of the population in $|e\rangle$. The outcome of this measurement would be

$$\alpha_1 = \frac{N}{2}|z_{-1}|^2.$$

2. A tripod transition with a bright state $|B_2\rangle = |0\rangle$, and a pulse length of $t'_1/2$, followed by a destructive measurement of the population in $|e\rangle$. The outcome of this measurement would be $\alpha_2 = \frac{N}{2}|z_0|^2$.
3. A tripod transition with a bright state $|B_3\rangle = |+1\rangle$, and a pulse length of $t'_1/2$, followed by a destructive measurement of the population in $|e\rangle$. The outcome of this measurement would be $\alpha_3 = \frac{N}{2}|z_{+1}|^2$. At this point, the system has $\frac{N}{2}$, in the same state ψ , that we started with. The only remaining unknowns are the relative phases between z_0 and z_{+1} and between z_0 and z_{-1} .
4. A 1-d PVM with a bright state $|B_4\rangle = \frac{1}{\sqrt{2}}(|-1\rangle - |0\rangle)$. The outcome would be $\alpha_4 = \frac{N}{4}|z_0 - z_{-1}|^2$.
5. A 1-d PVM with a bright state $|B_5\rangle = \frac{1}{\sqrt{2}}(|+1\rangle - |0\rangle)$ with an outcome α_5 .

The total number of atoms would be $N = 2(\alpha_1 + \alpha_2 + \alpha_3)$. The magnitudes $|z_0|$, $|z_{+1}|$ and $|z_{-1}|$ can also be extracted from α_1 , α_2 and α_3 . The relative phases between z_0 and z_{+1} and between z_0 and z_{-1} can be retrieved from α_4 and α_5 . Thus, if N is sufficiently large, we can extract the full spin-1 quantum state without re-initiating the system.

This is a useful technique, because it allows up to measure any observable, by writing it as a sum of 1-d PVMs, in particular, some unconventional operators such as Q_{xx} , Q_{xy} etc. The same technique can be used to perform a single-shot tomography of mixed spin-1 quantum states as well, that is, the 3×3 density matrix can be reconstructed after a set of measurements in a single shot. Reconstructing a density matrix in a single shot can have several applications like measuring the entanglement entropy of an interacting many-body state. If the atoms in the BEC are entangled, the corresponding reduced density matrix can be reconstructed in a single shot using the techniques discussed above. The Von-Neumann entropy of this density matrix will be a measure of the entanglement in the system, having avoided any effects from shot-to-shot fluctuations.

CHAPTER 8

STAIRCASE IN A BEC

In this chapter, we describe a phenomena that arises in a spin-1 BEC due to interacting between the atoms. The work represented in this chapter is also available in ref. [6].

In the integer quantum Hall effect, the Hall conductivity changes discretely to continuous tuning of the magnetic field [85, 86]. In general, when a system responds discretely to a continuous change of a control parameter, a staircase structure appears in its response function, which is a distinctive characteristic of quantization. Such phenomenon is significant on two counts. First, one can stabilize the system on a step of the staircase, that is, the flat region between two discrete jumps. Second, these stable states are potentially topological and may carry topological invariants of the system's phase space. The quantum Hall effect has been observed in fermionic two-dimensional (2D) electron gases [87, 88].

Bosonic analogues of quantum Hall states have been predicted to exist in rotating, weakly interacting Bose-Einstein condensates (BEC)[89, 90, 91, 92, 93, 94, 95]. A spinless, non-interacting, rotating BEC in a harmonic trap is characterized by Landau levels, similar to a 2D electron gas in a magnetic field [89]. For a rotating BEC, the trap frequency plays the role of the effective magnetic field and the corresponding lowest Landau level is degenerate in the angular momentum about the axis of rotation. This means that there are multiple angular momentum eigenstates within the lowest Landau level, thus, a weak interaction in the system may select one of these angular momentum eigenstates as the ground state of the system depending on the ratio of the interaction strength and the cyclotron frequency [89, 90]. Thus, the system's angular momentum responds discretely to continuous tuning of the effective magnetic field, in analogy with the quantum Hall effect. Recently, such phenomena has been predicted even in a spin-1 BEC [91] and a pseudo spin-1/2 BEC[94].

For the bosonic examples discussed above, the interaction plays a pivotal role in the

emergent angular momentum staircase as a function of the effective magnetic field. Two other quantum phenomena that also arise from interactions are squeezing and many body entanglement. Spin squeezed states have been prepared in bosonic systems [96, 97, 98, 99, 100, 101, 102, 103] and used to enhance the precision in a measurement, for example, of the applied magnetic field. They are characterized by noise in the transverse spin component that is lower than any classical state and are generally prepared with the help of an interaction term in the Hamiltonian. Two of the most common modes of preparing squeezed states, one-axis twisting and two-axis counter twisting, involve interactions [104].

We show three examples of spin-squeezing Hamiltonians, realizable in spin-1/2 and spin-1 BECs, that are characterized by a staircase response in the magnetization. First we show this for one-axis twisting Hamiltonian. Second, we demonstrate that an interacting ferromagnetic spin-1 BEC, where spin-nematic squeezing has been demonstrated [100], also displays a staircase. Third, we consider an interacting anti-ferromagnetic spin-1 BEC, where a staircase is also obtained in the direction of the magnetization. The first two examples are mesoscopic, while the third is a macroscopic phenomenon. We also propose experiments to observe these effects.

8.1 The One-axis Twisting Hamiltonian

8.1.1 Staircase in Magnetization and Entanglement Entropy

First, we consider a pseudo spin-1/2 BEC under the one-axis twisting Hamiltonian, $H = \chi S_z^2$, where S_z is the total spin operator in the z -direction and χ represents the strength of two body interactions in the system [104]. By applying a magnetic field p in the z -direction, we obtain a staircase structure in the ground state magnetization of the Hamiltonian, $H = \chi S_z^2 - p S_z$. We use units where $\hbar = 1$, S_z is dimensionless, χ and p are frequencies. The eigenstates of S_z are also eigenstates of this Hamiltonian. The energy of the eigenstate with a magnetization m is $E_m = \chi m^2 - pm$, for $m = -\frac{N}{2}, -\frac{N}{2} + 1, \dots, \frac{N}{2}$, where N is the number of atoms in the condensate. By minimizing the energy, we obtain the ground state

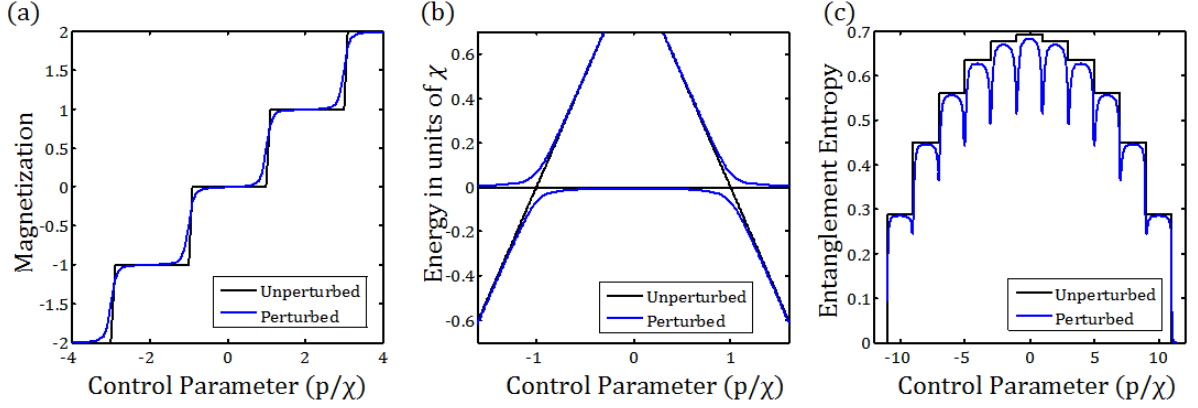


Figure 8.1: Staircase in the one-axis twisting Hamiltonian: (a) Shows the ground state magnetization as a function of the strength of the applied field p for constant interaction χ in the one-axis twisting Hamiltonian $H = \chi S_z^2 - p S_z$, with (blue curve) and without (black curve) the perturbation ϵS_x . (b) Shows the corresponding ground state and the first excited state energies around the level crossings between $m = -1$ and $m = 0$, as well as $m = 0$ and $m = +1$. In the absence of the perturbation, there are true level crossings, but when the perturbation is added, gaps open and thereby smooth the staircase. The term ϵS_x is also responsible for changing the system's magnetization, which is otherwise conserved. (c) Shows the entanglement entropy of the local ground state as a function of the control parameter p/χ . The black curve shows the entanglement without the perturbation as written in Eq.8.1, while the blue curve shows the entanglement with the perturbation for $\frac{\epsilon}{\chi} = 0.02$.

magnetization $m_{gs} = \lfloor \frac{p}{2\chi} \rfloor$, where $\lfloor x \rfloor$ represents the integer closest to x . Here, $\frac{p}{\chi}$ plays the role of the control parameter to which the magnetization responds discretely. The initial step of the magnetization staircase occurs when $\frac{p}{\chi} < -N$, with magnetization $m_{gs} = -\frac{N}{2}$, while the final step occurs when $\frac{p}{\chi} > N$, with magnetization $m_{gs} = \frac{N}{2}$. In between, the m_{gs} responds discretely to continuous variation of p as shown in Fig. 8.1(a).

Every step in this staircase is a distinct quantum state and every jump corresponds to a level crossing. The eigenenergies in the vicinity of a level crossing are shown in Fig. 8.1(b). Notice that this is a true level crossing, even when the system size is small, that is, it is not an avoided level crossing. Consequently, in order to observe this effect, one has to facilitate each jump in the staircase by opening up a gap at the level crossing. This can be done by adding a weak field ϵ in the x -direction leading to the Hamiltonian $H = \chi S_z^2 - p S_z - \epsilon S_x$, where ϵ is also in units of Hz. The resulting energy gaps for crossings between states with $m_{gs} = -1$ and $m_{gs} = 0$, as well as $m_{gs} = 0$ and $m_{gs} = +1$ are shown in Fig. 8.1(b). The

term ϵS_x also smoothes out the staircase in Fig. 8.1(a) and is responsible for changing the system's magnetization, which is otherwise conserved.

The quantum states in this magnetization staircase are related to the familiar Dicke ladder [105], where transitions between neighboring total angular momentum states of atoms can occur coherently leading to superradiance. An experiment where the control parameter $\frac{p}{\chi}$ is slowly swept from $-N$ to N would induce a transfer of the atom population between the spin states, one atom at a time. Furthermore, this is also a way of deterministically producing all the Dicke states in this ladder, most of which are highly entangled [106, 107]. In an experiment, the system can be initialized at $m = -\frac{N}{2}$ or $m = \frac{N}{2}$, where it is completely unentangled. As the control parameter $\frac{p}{\chi}$ is tuned, the magnetization m increases in integer steps and the corresponding entanglement entropy also steps up, peaking at $m = 0$, see Fig. 8.1(c). The entanglement entropy for magnetization m , in terms of the magnetization per atom, $\mu = \frac{m}{N}$, is given by

$$\mathcal{E} = -\left(\frac{1}{2} - \mu\right) \log\left(\frac{1}{2} - \mu\right) - \left(\frac{1}{2} + \mu\right) \log\left(\frac{1}{2} + \mu\right). \quad (8.1)$$

The perturbation ϵS_x , that was added to maintain adiabaticity at the level crossing, also perturbs the entanglement entropy, as shown in Fig. 8.1(c). The large dips in the entanglement entropy that appear at the level crossings are characteristic of a singular perturbation on the degenerate ground state space. Indeed, at the level crossing between magnetizations m and $m + 1$, the unperturbed ground state is a two dimensional space spanned by the eigenstates $\{|m\rangle, |m + 1\rangle\}$ of S_z with eigenvalues m and $m + 1$, respectively. The perturbation breaks this degeneracy and picks one state from this space as the ground state. For instance, with an ϵS_x perturbation, the ground state is $\frac{|m\rangle - |m+1\rangle}{\sqrt{2}}$, independent of ϵ . This state has a lower entanglement entropy than $|m\rangle$ and $|m + 1\rangle$, and it corresponds to the dip in the blue curve in Fig. 8.1(c). Thus, when $\epsilon \rightarrow 0$, the blue curve approaches the black curve at every point, excluding the level crossings.

The role of the interaction term χS_z^2 lies in introducing convexity into the energy functional. The energy, $E_m = \chi(m^2 - m\frac{p}{\chi})$ is a convex function in the discrete variable m and the control parameter $\frac{p}{\chi}$ contributes a linear term in this function. The minima of a convex function can be shifted by adding a linear term, however these shifts are discontinuous since the variable is discrete. This is the primary characteristic of the ground state energy of Hamiltonian which results in a staircase phenomena. Next, we use this observation to identify a staircase in the magnetization of a ferromagnetic spin-1 BEC, as a second example.

8.1.2 Experimental Considerations

There are several experimental systems where spin squeezing has been demonstrated using the one-axis twisting Hamiltonian including trapped ion systems [96, 101], Bose-Einstein condensates [108], double well [97], cavity systems [109, 98, 110, 111] and BECs in a chip trap [112, 112]. A ~ 3 atom detection limit has been demonstrated in a chip trap recently [113]. Moreover, single site detection has been established in quantum simulators that use neutral atoms [114] and ions [115]. The Hamiltonian discussed above can also be implemented in such systems [116].

Below, we discuss briefly how the effects of particle loss, detection and phase noise can be studied and we identify experimental systems that minimize these effects.

We begin with particle loss. In order to avoid the smearing out of the staircase due to particle loss, one has to design an adiabatic ramp that takes a shorter time than the particle loss time scale. The best way to design such a ramp is to maintain a constant Landau-Zener parameter throughout the ramp, following the method described in ref. [117]. We illustrate this idea using the first example from the manuscript. Let us consider the step that takes the magnetization from $m = 0$ to $m = 1$, at $p/\chi = 1$. The Hamiltonian $H = \chi S_z^2 - p S_z - \epsilon S_x$,

truncated to the relevant two dimensional subspace is

$$H = \begin{pmatrix} 0 & c\epsilon \\ c\epsilon & \chi - p \end{pmatrix} \quad (8.2)$$

Here, $c = \frac{1}{2}\sqrt{N(N+1)}$ and N is the number of atoms. The energy gap between the ground state and the excited state of the Hamiltonian above is $\Delta = \sqrt{(\chi - p)^2 + 4c^2\epsilon^2}$.

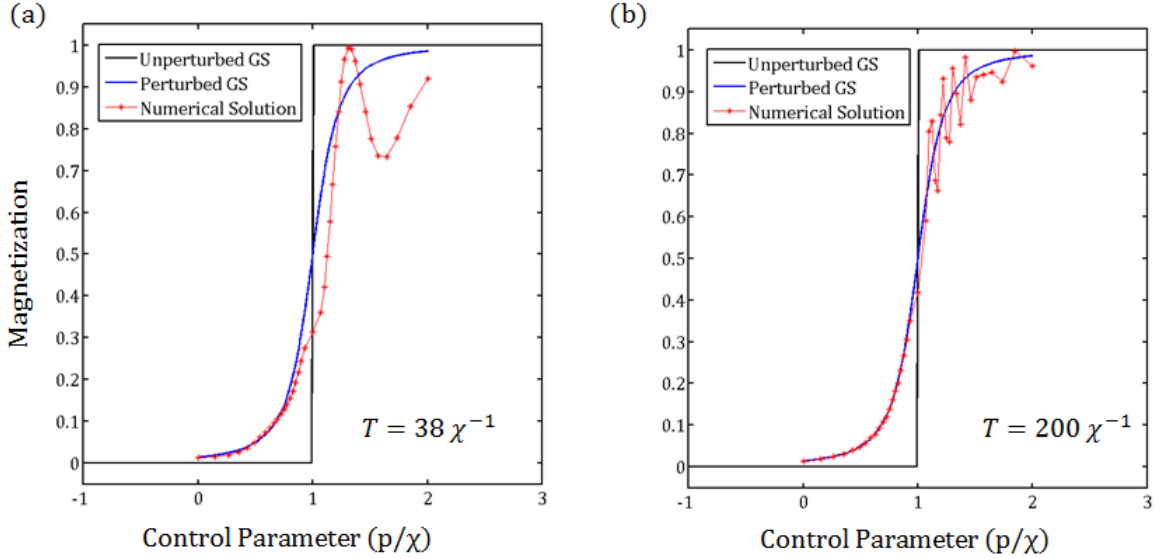


Figure 8.2: **Adiabatic ramps:** (a) shows a numerical solution for the magnetization an optimal adiabatic ramp that takes a total time of $T = 38\chi^{-1}$ (red curve), compared with the ground state magnetization (blue curve). Here, $c\epsilon = 0.12\chi$ and $\Gamma = 6$. (b) shows a numerical solution for the magnetization with $\Gamma = 31$, $c\epsilon = 0.12\chi$ and the resulting time is $T = 200\chi^{-1}$.

The control parameter p is to be ramped from 0 to 2χ , so as to maintain adiabaticity to the extent possible. The key idea is to adapt the rate of the ramp to be fast when the gap Δ is large and slow when the gap is small. More precisely, we keep the Landau-Zener parameter Γ , a measure of adiabaticity, constant throughout the ramp [118],

$$\Gamma = \frac{\Delta^2}{d\Delta/dt} = \frac{((\chi - p)^2 + 4c^2\epsilon^2)^{3/2}}{(p - \chi)dp/dt}. \quad (8.3)$$

The ramp $p(t)$ is the solution to the differential equation obtained by keeping Γ constant. The total time it takes to change p from 0 to 2χ is

$$T = \int_0^{2\chi} \frac{dp}{dp/dt} = \frac{\Gamma}{c\epsilon} - \frac{2\Gamma}{\sqrt{\chi^2 + 4c^2\epsilon^2}} \approx \frac{\Gamma}{c\epsilon} - \frac{2\Gamma}{\chi}. \quad (8.4)$$

The perturbation parameter ϵ quantifies how closely the ground state magnetization follows a staircase structure — a large ϵ would smooth out the staircase completely. The parameter Γ quantifies how closely the state of the system follows the ground state of the local Hamiltonian. In Fig. 8.2(a) we show a numerical solution for the magnetization with $\Gamma = 6$ and $c\epsilon = 0.12\chi$. With this set of parameter values, $T = 38\chi^{-1}$. In Fig. 8.2(b) we show a numerical solution for $\Gamma \approx 31$ and $T = 200\chi^{-1}$. When $p/\chi > 1$, the fast oscillation of the magnetization about the ground state value is caused by non-adiabaticity. These oscillations represent an excitation of the system above the ground state caused due to a non-adiabaticity at the level crossing $p/\chi = 1$. They disappear in the limit of $T \gg \chi^{-1}$.

In order to avoid particle loss, the time T has to be small compared to the time scale of particle loss. This consideration reveals that Feshbach resonance induced interactions are unfavorable to observe this effect — while increasing the interaction strength χ , Feshbach resonance simultaneously decreases the timescale of particle loss (see page 21 of [119]). However, BECs in an atom chip trap are much more promising in this regard [112]. Interaction strengths up to $\chi \sim 3$ Hz can be induced in such systems [120]. Using the parameters of Fig. 8.2(a), $T \approx 13$ s when $\chi = 3$ Hz, which near the limit, but below the typical trap lifetimes (15-20 s), which can also be increased using better vacuum.

In the same system, detection noise levels up to ~ 3 atoms have been reported [113]. Therefore one can observe the staircase feature in atom chip traps after a moderate enhancement of detection noise and trap lifetime.

Moreover, quantum simulators that use neutral atoms [114] and ions [115] have been successfully used to observe mesoscopic effects with single site resolution. Similar Hamiltonians can be simulated in these systems [116] with interaction strengths as large as

$\chi \approx 0.5\text{KHz}$ [115], allowing for better adiabatic ramps.

The typical interaction strength in the second example representing a ferromagnetic spin-1 BEC is $|c| \sim 10 \text{ Hz}$ [117]. This allows for adiabatic ramps up to $T \lesssim 100|c|^{-1}$ which is well within the particle loss timescale.

Finally, phase noise would not directly impact an adiabatic (or a nearly adiabatic) evolution, because such ramps keep the system near the ground state throughout. The effective number of dynamical cycles completed by the system during the adiabatic ramp is given by $n = \int_{t=0}^{t=T} \Delta(t) dt$. For the ramps described above, that keep a constant Landau-Zener parameter, this number is $n = 2\Gamma \log(\chi/c\epsilon)$. It is 24 for the parameters in Fig. 8.2(a) and about 120 for the parameters in Fig. 8.2(b). In fact adiabatic ramps with length 40 s have been demonstrated in spin-1 ferromagnetic BECs [117]. With an interaction strength of $|c| \sim 10 \text{ Hz}$, this would correspond to a similar number of cycles.

8.1.3 Computing the Entanglement Entropy

A Bosonic many-body state has a unique single atom reduced density matrix, due to its symmetry. Therefore, a convenient measure of many-body entanglement of such states is the Von Neumann entropy of the single atom reduced density matrix. The following simple observation helps us determine the single atom reduced density matrix ρ corresponding to a many-body pure state $|\psi\rangle$ and evaluate its entanglement entropy: If \hat{o} is a single atom observable operator and $\hat{O} = \sum_{i=1}^N \hat{o}_i$ is the corresponding many-body observable, then

$$\text{Tr}(\rho\hat{o}) = \frac{1}{N} \langle \psi | \hat{O} | \psi \rangle. \quad (8.5)$$

For instance, the spin operator along the x -axis for a single, spin-1/2 atom is $L_x = \frac{1}{2}\sigma_x$ in units of \hbar , where σ_x is the Pauli matrix. While the many-body spin operator along the x -axis is simply given by $S_x = \frac{1}{2} \sum_{i=1}^N \sigma_{xi}$. The symmetry of the many-body state $|\psi\rangle$ ensures that $\text{Tr}(\rho\sigma_x) = \frac{2}{N} \langle \psi | S_x | \psi \rangle$. The reduced density matrix ρ can be reconstructed

using the expectation values of a few different observables.

We illustrate this idea with an example. Let us consider the ground state of the one-axis twisting Hamiltonian $H = \chi S_z^2 - p S_z$, where S_z is the many-body spin operator along the z -axis. The ground state $|\psi\rangle$ of this Hamiltonian is an eigenstate of S_z with a magnetization given by $m = \left\lfloor \frac{p}{2\chi} \right\rfloor$, the integer closest to $\frac{p}{2\chi}$. It follows from Eq. 8.5 that the single atom reduced density matrix ρ of $|\psi\rangle$ has spin expectation values

$$\begin{aligned}\mathrm{Tr}(\sigma_x \rho) &= \frac{2}{N} \langle \psi | S_x | \psi \rangle = 0 \\ \mathrm{Tr}(\sigma_y \rho) &= \frac{2}{N} \langle \psi | S_y | \psi \rangle = 0 \\ \mathrm{Tr}(\sigma_z \rho) &= \frac{2}{N} \langle \psi | S_z | \psi \rangle = \frac{2m}{N}.\end{aligned}\tag{8.6}$$

Using the spin expectation values given above, we may reconstruct the density matrix ρ as

$$\rho = \frac{1}{2} \left(\mathbf{1} + \frac{2m}{N} \sigma_z \right) = \begin{pmatrix} \frac{1}{2} + \frac{m}{N} & 0 \\ 0 & \frac{1}{2} - \frac{m}{N} \end{pmatrix}.\tag{8.7}$$

The Von Neumann entropy of this state is $\mathcal{E} = -\mathrm{Tr}[\rho \log(\rho)]$.

Next, we consider the perturbed Hamiltonian $H = \chi S_z^2 - p S_z - \epsilon S_x$. In the absence of the ϵS_x perturbation, a level crossing occurs at $\frac{p}{2\chi} = m + 1/2$. Without loss of generality, we may assume that $m \leq \frac{p}{2\chi} \leq m + 1$. The ground state magnetization is m when $\frac{p}{2\chi} < m + \frac{1}{2}$ and it is $m + 1$ when $\frac{p}{2\chi} > m + \frac{1}{2}$. Accordingly, it is convenient to use $\delta = \frac{p}{2\chi} - m - \frac{1}{2}$ as a function of the control parameter $\frac{p}{\chi}$. The range of δ is $[-1/2, 1/2]$ and the magnetization switches from m to $m + 1$ when δ crosses zero. The ground state, in the presence of the ϵS_x perturbation is a superposition of $|m\rangle$ and $|m + 1\rangle$, the eigenstates of S_z with eigenvalues m and $m + 1$ respectively

$$|\psi\rangle = u|m\rangle + v|m + 1\rangle.\tag{8.8}$$

The coefficients u and v depend on δ and are given by

$$\begin{aligned} u &= \sqrt{\frac{1}{2} \left(1 - \frac{\delta}{\sqrt{\delta^2 + C_m^2 \frac{\epsilon^2}{4\chi^2}}} \right)} \\ v &= \sqrt{\frac{1}{2} \left(1 + \frac{\delta}{\sqrt{\delta^2 + C_m^2 \frac{\epsilon^2}{4\chi^2}}} \right)}. \end{aligned} \quad (8.9)$$

Here, C_m is the relevant Clebsch-Gordon coefficient, $C_m = \sqrt{(N/2 - m)(N/2 + m + 1)}$.

It is now straightforward to compute the spin expectation values

$$\begin{aligned} \text{Tr}(\sigma_x \rho) &= \frac{2}{N} \langle \psi | S_x | \psi \rangle = \frac{2uvC_m}{N} \\ \text{Tr}(\sigma_y \rho) &= \frac{2}{N} \langle \psi | S_y | \psi \rangle = 0 \\ \text{Tr}(\sigma_z \rho) &= \frac{2}{N} \langle \psi | S_z | \psi \rangle = \frac{2}{N} (m + v^2), \end{aligned} \quad (8.10)$$

which can be used to obtain the reduced density matrix

$$\rho = \begin{pmatrix} \frac{1}{2} + \frac{m+v^2}{N} & \frac{uvC_m}{N} \\ \frac{uvC_m}{N} & \frac{1}{2} - \frac{m+v^2}{N} \end{pmatrix}. \quad (8.11)$$

The off diagonal terms are the largest when $\delta = 0$ that is, when the control parameter $\frac{p}{\chi} = 2m + 1$. Correspondingly, the Von Neumann entropy of the density matrix defined in Eq. 8.11, has a dip at odd values of $\frac{p}{\chi}$, as shown in Fig. 8.1(c).

8.2 Staircase in a ferromagnetic spin-1 BEC.

Recall that under the single mode approximation, the Hamiltonian of our system (spin-1 ferromagnetic BEC) is, Here, V_T is the dipole trapping potential, the interaction between pairs of atoms is modeled by a δ function potential and it involves two s-wave scattering lengths, a_0 and a_2 , corresponding to the possible total spin of the two interacting atoms,

both of which are in the spin-1 state. In addition, the relevant Landé g-factor is g_F and L_{zi} is the spin operator for the i -th atom. The hyperfine splitting between the $F = 1$ and $F = 2$ levels is Δ . Assuming that the trap is sufficiently tight, one can approximate the ground state by a product of a spatial wave function common to all spin modes and a collective N -atom spin state. This is also known as the single mode approximation (SMA). Under SMA, the spin part of the Hamiltonian is

$$H = cS^2 + qQ_{zz} - pS_z, \quad (8.12)$$

where $c < 0$ is the interaction strength, given by $c = \frac{4\pi\hbar^2(a_2-a_0)}{3m} \int |\phi(\mathbf{r})|^4 d\mathbf{r}$, where $\phi(\mathbf{r})$ is the common spatial wave function. The total spin operator of all the atoms is S^2 , the strength of the quadratic Zeeman term is $q = \frac{\mu_B^2}{\hbar^2\Delta}$ and the linear Zeeman contribution is $p = \mu_B g_F B_z$. The collective spin and second rank tensor operators are $S_z = \sum_{i=1}^N L_{zi}$ and $Q_{zz} = \sum_{i=1}^N L_{zi}^2$, respectively. This Hamiltonian has been used to produce spin-nematic squeezed states [100].

We show that the quadratic Zeeman effect induces an energy that is convex in the system's magnetization and therefore, with c and q fixed to appropriate values, we can obtain an analogous staircase in this system. The Hamiltonian commutes with S_z and therefore, it has simultaneous eigenstates with the latter. Let us denote these eigenstates by $|n, m\rangle$, with

$$\begin{aligned} (cS^2 + qQ_{zz})|n, m\rangle &= \lambda_{nm}|n, m\rangle \\ S_z|n, m\rangle &= m|n, m\rangle \end{aligned} \quad (8.13)$$

The eigenenergy of this state is $E_{nm} = \lambda_{nm} - pm$. Obtaining the ground state involves a simultaneous minimization over n and m . We define the function E_m as the minimal value of E_{nm} over all n , corresponding to the ground state energy of the Hamiltonian for fixed magnetization. The global ground state is obtained by minimizing E_m over m . The

Zeeman term p contributes a linear term to E_m leading to

$$E_m = \min_n \{ \lambda_{nm} - pm \} = \min_n \{ \lambda_{nm} \} - pm \quad (8.14)$$

We use $|c|$ as our energy unit, and show in Fig. 8.3 that E_m is a convex function of m . Consequently, the ground state magnetization varies through discrete values of m , when the control parameter $p/|c|$ is tuned. When $q \ll |c|$, the energy $E_m \approx -|c|N(N+1) - pm$ is linear in m and has a minimum at $m = \frac{N}{2}$. When $q \gg |c|$ and $q > p$, the energy $E_m \approx q|m| - pm$ has a minimum at $m = 0$. Upon variation of q between these two extremes, E_m must have a minimum between $m = 0$ and $m = \frac{N}{2}$, and must be a convex function of m as seen in Fig. 8.3 .

Thus, we obtain a similar staircase structure in the magnetization, when $\frac{p}{|c|}$ is varied adiabatically. Like the previous example, the flat areas in the staircase correspond to distinct quantum states and a discrete jump corresponds to a level crossing, which needs to be facilitated by opening up an energy gap. Again, this can be done by perturbing the Hamiltonian with a weak field in the x -direction ϵS_x . In typical experiments [100], $|c| \sim 10$ Hz and $q \sim 2|c|$, indicating that the emergence of the magnetization staircase is also accessible to existing techniques. Similar to the previous example, the entanglement entropy also has a staircase structure.

Both of the examples discussed so far are mesoscopic in the sense that the values of the control parameter corresponding to adjacent steps are separated by $\sim \frac{1}{N}$, where N is the number of atoms. Therefore, in the limit of large atom numbers, it is increasingly more difficult to resolve the different jumps. However, next we show that in an anti-ferromagnetic condensate, a similar staircase structure appears as a truly macroscopic manifestation, where, the jumps are macroscopically separated.

8.3 Staircase in an anti-ferromagnetic spin-1 BEC.

We consider a spin-1 anti-ferromagnetic BEC with an applied field p in the z -direction leading to the Hamiltonian $H = cS^2 - pS_z$, where $c > 0$ [121, 122]. For sufficiently small magnetic field, we can omit the quadratic Zeeman terms. The eigenstates of this Hamiltonian are the total spin states $|s, m\rangle$ with $-s \leq m \leq s$ and $s = 0, 2, 4, \dots, N$ (assuming N is even), due to bosonic symmetry. Here, s is the total spin of the system, that is, $S^2|s, m\rangle = s(s+1)|s, m\rangle$. The eigenenergy of $|s, m\rangle$ is $E_{sm} = cs(s+1) - pm$. When $p > 0$, the ground state has $m = +s$. In this case the energy

$$E_s = \min_m E_{sm} = cs^2 + (c - p)s \quad (8.15)$$

is a convex function in s . In contrast to previous examples, the control parameter is the coefficient c of the quadratic term instead of the field p in the linear Zeeman contribution.

The ground state value of s is the non-negative integer closest to $\frac{p-c}{2c}$. When $c = 0$, the ground state has $s = N$ and when $c \geq p$, it has $s = 0$. Because s has a staircase structure, so does the systems magnetization. The level crossings in this staircase occur at values of c given by

$$c_s = \frac{p}{2s-1}; \quad s = 2, 4, \dots, N. \quad (8.16)$$

The magnetization of the ground state is given by $\langle \vec{S} \rangle = (0, 0, s)$ and develops a staircase structure when c is tuned. We show now that by adding a suitable perturbation to the Hamiltonian, this staircase structure can be transferred to the *direction* of the magnetization.

Let us perturb the Hamiltonian by Q_{xz} , which is a quadratic variable given by $Q_{xz} = \sum_i \{L_{xi}, L_{zi}\}$ for a single atom. The Hamiltonian becomes $H = cS^2 - pS_z + \alpha Q_{xz}$. Within a given step in the staircase, $\frac{p}{2s+1} < c < \frac{p}{2s-1}$, we use first order perturbation theory

to obtain the ground state

$$|\psi_s\rangle = |s, s\rangle + \frac{\alpha}{p} q_s |s, s-1\rangle \quad (8.17)$$

from the unperturbed ground state $|s, s\rangle$. Here, $q_s = \langle s, s | Q_{xz} | s, s-1 \rangle = \frac{\sqrt{2s}}{4} \left(\frac{2N+3}{2s+3} \right)$ is the relevant matrix element. In this case, the magnetization

$$\langle \vec{S} \rangle = s \hat{z} + \frac{\alpha}{p} \sqrt{2s} q_s \hat{x} \quad (8.18)$$

is tilted away from the z -axis with a polar angle given by

$$\theta_s = \arctan \left(\frac{\alpha \sqrt{2s} q_s}{ps} \right). \quad (8.19)$$

This angle has a staircase structure with c as the control parameter as shown in Fig. 8.4. Similar to the previous examples, the flat regions of the staircase are distinct quantum states and the associated level crossings need to be facilitated by the opening of a gap created by a perturbation of the type ϵQ_{xx} , (here, $Q_{xx} = \sum_{i=1}^N L_{xi}^2$) that introduces an overlap between states $|s, s\rangle$ and $|s \pm 2, s \pm 2\rangle$. Good candidates to observe this effect experimentally are ^{23}Na condensates. Typically, $c \sim 20\text{Hz}$ [123] with a macroscopic number of $N = 10^5$ atoms. The steps in Fig. 8.4, corresponding to $s = 1, 2, 3$, are separated by a few hertz on the c axis and they are independent of the number of atoms. Therefore, this effect is macroscopic and also observable within the existing experimental systems.

8.3.1 Computing the Matrix Element q_s

Next, we show how the expression for the matrix element $q_s = \langle s, s-1 | Q_{xz} | s, s \rangle$ used in Eq. [8] is derived. The space of symmetric states of N spin-1 atoms has $\frac{(N+1)(N+2)}{2}$ dimensions. A convenient basis for this space is given by the normalized number states, defined as $|N_+, N_0, N_-\rangle = (a_{-1}^\dagger)^{N_-} (a_0^\dagger)^{N_0} (a_{+1}^\dagger)^{N_+} |\text{vac}\rangle$, where a_i^\dagger is the creation operator

for the i -th mode, $|\text{vac}\rangle$ is the vacuum state, with no atoms, and $N = N_+ + N_0 + N_-$ is the total number of atoms.

An alternative basis, also of relevance in the present context is given by the coupled spin states $|s, m\rangle$ with $-s \leq m \leq s$ and $s = N, N-2, \dots, s_{min}$. When N is even, the minimum value of s is $s_{min} = 0$ and when N is odd, $s_{min} = 1$. These states are the simultaneous eigenstates of the total spin operators S^2 and S_z with eigenvalues given by $S^2|s, m\rangle = s(s+1)|s, m\rangle$ and $S_z|s, m\rangle = m|s, m\rangle$.

To evaluate the matrix element of interest, $q_s = \langle s, s-1|Q_{xz}|s, s\rangle$, we need to determine the action of the operator Q_{xz} on the state $|s, s\rangle$ or the state $|s, s-1\rangle$. However, it is easier to determine the action of this operator on the number states

$$\begin{aligned} Q_{xz}|N_+, N_0, N_-\rangle = & \\ & c_1|N_+ + 1, N_0 - 1, N_-\rangle - c_2|N_+, N_0 + 1, N_- - 1\rangle \\ & + c_3|N_+ - 1, N_0 + 1, N_-\rangle - c_4|N_+, N_0 - 1, N_- + 1\rangle, \end{aligned} \quad (8.20)$$

where the coefficients are given by $c_1 = \sqrt{\frac{(N_++1)N_0}{2}}$, $c_2 = \sqrt{\frac{(N_0+1)N_-}{2}}$, $c_3 = \sqrt{\frac{N_+(N_0+1)}{2}}$ and $c_4 = \sqrt{\frac{N_0(N_-+1)}{2}}$. The result shown in Eq. 8.20 follows from the definition of the many-body operator $Q_{xz} = \sum_{i=1}^N \{L_{xi}, L_{zi}\}$ and the matrix form of the single-atom operator

$$\{L_{xi}, L_{zi}\} = \frac{1}{\sqrt{2}} \begin{pmatrix} 0 & 1 & 0 \\ 1 & 0 & -1 \\ 0 & -1 & 0 \end{pmatrix}. \quad (8.21)$$

The matrix element $\langle s, s-1|Q_{xz}|s, s\rangle$ can be computed by expressing the coupled spin states $|s, m\rangle$ in the number state basis. Noting that $S_z|s, m\rangle = m|s, m\rangle$ and $S_z|N_+, N_0, N_-\rangle = (N_+ - N_-)|N_+, N_0, N_-\rangle$, the overlap $\langle s, m|N_+, N_0, N_-\rangle$ vanishes unless $N_+ - N_- = m$.

Therefore, we may write

$$|s, s\rangle = \sum_{k=0}^{\frac{N-s}{2}} A_k |k + s, N - 2k - s, k\rangle \quad (8.22)$$

Since $|s, s - 1\rangle = \frac{1}{\sqrt{2s}} S_- |s, s\rangle$ where S_- is the lowering operator, it suffices to determine A_k in order to evaluate the matrix element q_s . The coefficients A_k can be evaluated using the observation that the raising operator S_+ annihilates the state $|s, s\rangle$, that is $S_+ |s, s\rangle = 0$. Using the relation

$$\begin{aligned} S_+ |N_+, N_0, N_-\rangle = \\ c_1 |N_+ + 1, N_0 - 1, N_-\rangle + c_2 |N_+, N_0 + 1, N_- - 1\rangle \end{aligned} \quad (8.23)$$

in conjunction with $S_+ |s, s\rangle = 0$ gives the recursive relation

$$A_{k+1} = A_k \sqrt{\frac{(k + s + 1)(N - 2k - s)}{(k + 1)(N - 2k - s - 1)}}. \quad (8.24)$$

Solving for A_k for $k > 0$ we obtain

$$A_k = A_0 \sqrt{\frac{(k + s)!(N - 2k - s - 1)!!}{k!(N - 2k - s)!!}}, \quad (8.25)$$

where A_0 is obtained from the normalization condition $\sum_k A_k^2 = 1$. It is useful to make the connection with hypergeometric functions here by noticing that the squares of the coefficients A_k are generated by a hypergeometric function,

$$\sum_{k=0}^{\frac{N-s}{2}} \frac{A_k^2}{A_0^2} x^k = {}_2F_1 \left(-\frac{(N-s)}{2}, s + 1; -\frac{(N-s-1)}{2}, x \right). \quad (8.26)$$

This follows from the observation that the above recursion relation on the coefficients A_k

is also the recursion between consecutive terms of a hypergeometric series:

$$A_{k+1}^2 = A_k^2 \frac{\left(-\frac{(N-s)}{2} + k\right) (s+1+k)}{\left(-\frac{(N-s-1)}{2} + k\right)} \frac{1}{(k+1)}. \quad (8.27)$$

This gives a simple expression for the first coefficient

$$A_0 = \frac{1}{\sqrt{{}_2F_1\left(-\frac{(N-s)}{2}, s+1; -\frac{(N-s-1)}{2}, 1\right)}}. \quad (8.28)$$

In fact, there is a closed-form expression for this particular evaluation of hypergeometric functions where the first argument is a negative integer,

$${}_2F_1(-n, b; c, 1) = \frac{(c-b)(c-b+1)\cdots(c-b+n-1)}{c(c+1)\cdots(c+n-1)} \quad (8.29)$$

Noting that $\frac{(N-s)}{2}$ is always an integer, Eqs. 8.25 and 8.28 together give us all the A_k coefficients.

We are now ready to evaluate the matrix element q_s , which can also be written as

$$q_s = \frac{1}{\sqrt{2s}} \langle s, s | Q_{xz} S_- | s, s \rangle \quad (8.30)$$

This expression can be viewed as an overlap between the vectors, $|\psi_1\rangle = Q_{xz}|s, s\rangle$ and $|\psi_2\rangle = S_-|s, s\rangle$, scaled by a factor of $\frac{1}{\sqrt{2s}}$. Besides Eq. 8.20, another expression that is useful to evaluate this overlap is

$$\begin{aligned} S_- |N_+, N_0, N_-\rangle = \\ c_3 |N_+ - 1, N_0 + 1, N_-\rangle + c_4 |N_+, N_0 - 1, N_- + 1\rangle, \end{aligned} \quad (8.31)$$

which shows the action of the lowering operator on a number state. Starting from the expansion of the state $|s, s\rangle$ in the number basis given in Eq. 8.22, and using the action

of Q_{xz} on a number state given in Eq. 8.20 we may expand $|\psi_1\rangle$ in the number basis. Similarly, $|\psi_2\rangle$ can be expanded in the number basis using Eq. 8.31. The overlap $\langle\psi_1|\psi_2\rangle$ can be written in terms of the coefficients A_k as

$$\sqrt{2sq_s} = \langle\psi_1|\psi_2\rangle = \sum_{k=0}^{\frac{N-s}{2}} s(N-2k-s+\frac{1}{2})A_k^2. \quad (8.32)$$

The evaluation of this quantity requires a crucial sum $\sum_k kA_k^2$, which is obtained by taking a derivative of Eq. 8.26:

$$\begin{aligned} \sum_{k=0}^{\frac{N-s}{2}} k \frac{A_k^2}{A_0^2} &= \\ \left[\frac{d}{dx} {}_2F_1 \left(-\frac{(N-s)}{2}, s+1; -\frac{(N-s-1)}{2}, x \right) \right]_{x=1}. \end{aligned} \quad (8.33)$$

The derivative of a hypergeometric function can also be written in terms of a hypergeometric function as

$$\begin{aligned} \frac{d}{dx} {}_2F_1 \left(-\frac{(N-s)}{2}, s+1; -\frac{(N-s-1)}{2}, x \right) &= \\ C_{N,s} {}_2F_1 \left(-\frac{(N-s-2)}{2}, s+2; -\frac{(N-s-3)}{2}, x \right), \end{aligned} \quad (8.34)$$

which is a standard relation. In this expression the coefficient $C_{N,s}$ depends on total number of atoms N and the total spin s as

$$C_{N,s} = \frac{(s+1) \binom{N-s}{2}}{\binom{N-s-1}{2}}. \quad (8.35)$$

We now use Eq. 8.29 to evaluate this expression at $x = 1$ and obtain the desired sum of the series

$$\sum_{k=0}^{\frac{N-s}{2}} kA_k^2 = \frac{(N-s)(s+1)}{2s+3}, \quad (8.36)$$

which leads to the final result for the matrix element

$$q_s = \frac{\sqrt{2s}}{4} \left(\frac{2N + 3}{2s + 3} \right), \quad (8.37)$$

that we used to determine the staircase in the tilt angle of the spin vector shown in Fig. 3(b).

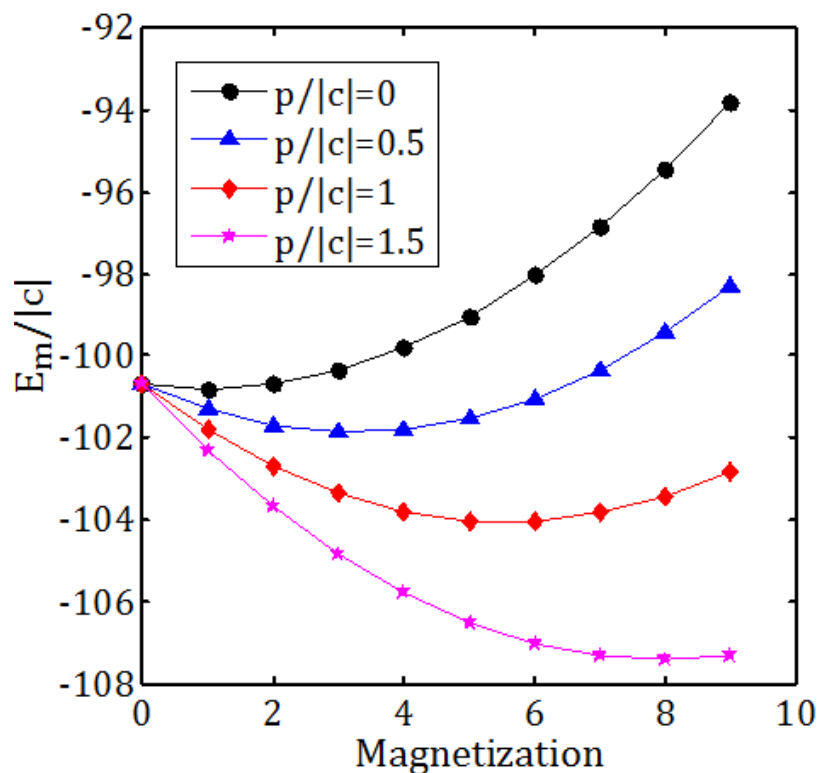


Figure 8.3: **Convexity of the energy:** The minimum energy eigenvalue E_m of the ferromagnetic Hamiltonian $H = cS^2 + qQ_{zz} - pS_z$ is a convex function of the magnetization m . For the purpose of this illustration, we have used $N = 10$. The minima of these curves correspond to the ground state magnetization. Because p is the coefficient of a linear term in m , changing it has the effect of shifting the minimum. The four values of $p/|c|$ have their minima at different values of m , leading to a staircase response of the ground state magnetization as $p/|c|$ is changed.

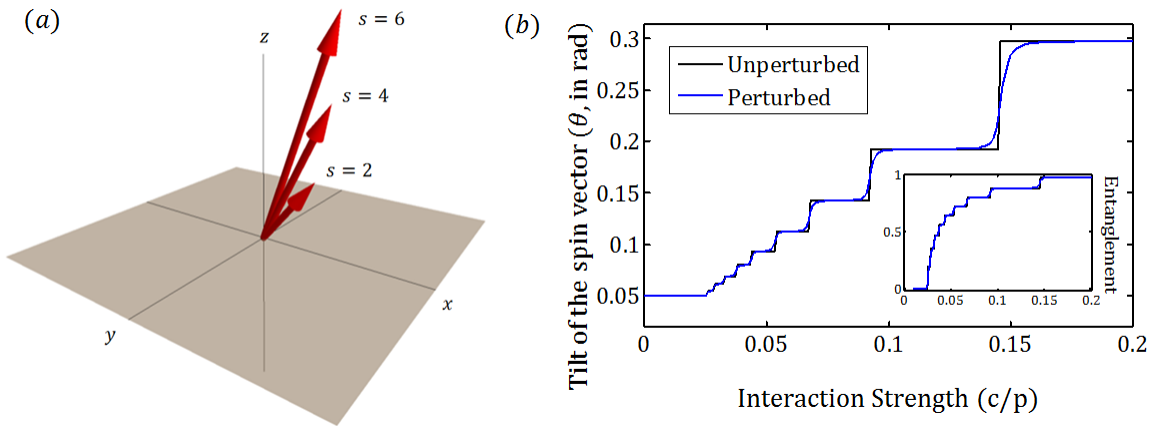


Figure 8.4: **Staircase in the magnetization direction:** (a) shows the ground state magnetization vector of an anti-ferromagnetic condensate with Hamiltonian $H = cS^2 + pS_x + \alpha Q_{xz}$, for three different values of c with $N = 100$. The last term in the Hamiltonian induces the tilting of the magnetization vector by specific angles, depending on where the system is on the staircase. (b) shows the tilt angle for $N = 20$ as a function of c/p , a staircase, but in contrast with the previous examples, this time it is not only in the magnitude of magnetization, but also in the direction. The blue curve shows the smoothed staircase after adding an ϵQ_{xx} perturbation, with $\epsilon = 0.02p$. The inset shows the ground state entanglement entropy as a function of the control parameter. In both (a) and (b), $\alpha = 0.1p$.

CHAPTER 9

ENTANGLEMENT IN A BEC

One of the consequences of the s-wave scattering interaction of an ^{87}Rb BEC is that the atoms evolve into a many-body entangled state. Entanglement has several interesting and useful features. For instance, one of the aspects of entanglement is squeezing [124], which can be applied in sub shot-noise metrology. Characterizing and quantifying the entanglement in the many body entangled state that is generated out of evolution under the interacting Hamiltonian of a BEC has been an active area of research [125, 126].

In this chapter, we outline a new approach towards characterizing mixed state entanglement of many body systems, based on techniques imported from *real algebraic geometry*. This work, in its complete form, has been reported in a separate thesis [4] and therefore we provide a very brief outline here.

9.1 Many Body Entanglement

An N -atom mixed state ρ is said to be separable if it can be written as a convex sum of product states. That is,

$$\rho = \sum_i \mu_i \rho_{i,1} \otimes \rho_{i,2} \otimes \cdots \otimes \rho_{i,N} \quad (9.1)$$

where, $\rho_{i,k}$ is a density matrix corresponding to the state of the k -th atom and μ_i are weights satisfying $\sum_i \mu_i = 1$. If a density matrix is not separable, we say that it is entangled. The difficulty with characterizing the entanglement of a many-body system is two fold — the problem of deciding whether a given density matrix is entangled or not is known to be NP-hard, and further, it is experimentally unfeasible at the moment to even measure the full density matrix of a many-body system.

Therefore, recent work have focused on a slightly different problem — given a subset of

observables measured in the lab, which do not constitute a full state tomography, what can be said regarding the entanglement of the underlying system? For instance, if the many-body observables S_x, S_y, S_z and $\Delta S_x^2, \Delta S_y^2, \Delta S_z^2$ have been measured experimentally on a potentially entangled BEC, can we estimate the entanglement of the system using the set of measured quantities? This question was partially answered in ref. [125, 126], where a smaller subset of the observables, namely, $S_x^2 + S_y^2$ and ΔS_z^2 were used to obtain entanglement measures.

In this work, we consider the more general problem that uses all of the six observables mentioned above. We show that this problem is deeply connected the well known *truncated K-moment problem* (TKMP) in real algebraic geometry, and utilize the standard results in TKMP to solve the problem at hand. We begin with a brief overview of TKMPs.

9.2 Truncated K-Moment Problem

The problem of deciding whether a set of numbers are moments of a probability distribution is known as the *moment problem*. A variant of the moment problem, where only a truncated set of moments are known is called the *truncated moment problem*. If the probability distribution is constrained to be defined over a compact set K , then the corresponding truncated moment problem is called the truncated K-moment problem or TKMP. The standard moment problem for probability distributions defined over \mathbb{R} is known as the *Hamburger moment problem*. For probability distributions defined over $[0, \infty)$ the moment problem is known as the *Stieltjes moment problem*. The moment problem for probability distributions defined over $K = [0, 1]$ is known as Hausdorff moment problem. These standard examples have a complete solution [127].

The problem of deciding whether a quantum state is entangled or not is naturally related to TKMP. Indeed, the elements of the density matrix of a separable state are moments of some underlying probability distribution, represented by the weights μ_i in Eq. 9.1, which can, in general be assumed as a continuous measure. Therefore, deciding whether a density

matrix is entangled is a TKMP. Further, deciding whether a set of observables represent an entangled state is also a TKMP. We illustrate this point with the simple case of entanglement of a pair of spin-1/2 atoms.

9.2.1 An Example

We consider a composite system of a pair of two-level atoms. A general mixed state of such a system is represented by a 4×4 density matrix. We use superscripts A and B to indicate the two subsystems and we use ρ^{AB} to represent the density matrix of the composite system.

A mixed state of two spin-1/2 systems is said to be separable, iff the corresponding density matrix ρ_S^{AB} can be written as a convex sum of product states, according to Eq. 9.1

$$\rho_S^{AB} = \sum_{i=1}^n \mu_i \rho_i^A \otimes \rho_i^B \quad (9.2)$$

The subscript S is used to indicate that the state is separable. ρ_i^A and ρ_i^B are 2×2 density matrices representing mixed states of the subsystems A and B respectively. $\mu_i > 0$ are weights satisfying $\sum_{i=1}^n \mu_i = 1$. A density matrix that does not admit such a resolution is called an entangled state.

A 2×2 density matrix is represented by a point inside the Bloch ball, \mathbb{B} . Indeed, a 2×2 density matrix can be written in terms of the Pauli matrices

$$\rho = \frac{1}{2}(\mathbf{1} + \mathbf{u} \cdot \boldsymbol{\sigma}) = \frac{1}{2}(\mathbf{1} + u_x \sigma_x + u_y \sigma_y + u_z \sigma_z) \quad (9.3)$$

Here, $\mathbf{u} = (u_x, u_y, u_z)$ is a point in \mathbb{B} . The 2×2 identity matrix is represented by $\mathbf{1}$. σ_x , σ_y and σ_z are the Pauli matrices defined as

$$\sigma_x = \begin{pmatrix} 0 & 1 \\ 1 & 0 \end{pmatrix}; \quad \sigma_y = \begin{pmatrix} 0 & -i \\ i & 0 \end{pmatrix}; \quad \sigma_z = \begin{pmatrix} 1 & 0 \\ 0 & -1 \end{pmatrix} \quad (9.4)$$

Therefore the definition of a separable state can be expressed as

$$\rho_S^{AB} = \frac{1}{4} \sum_{i=1}^n \mu_i (\mathbf{1} + \mathbf{u}_i \cdot \sigma^A) \otimes (\mathbf{1} + \mathbf{v}_i \cdot \sigma^B) \quad (9.5)$$

σ^A and σ^B are the Pauli pseudo vectors corresponding to subsystems A and B respectively. An equivalent definition of separable states is obtained by replacing the sum by an integral and the weights μ_i by a continuous measure μ defined over $\mathbb{B} \times \mathbb{B}$. That is, a state is separable iff there exists a measure μ defined over $\mathbb{B} \times \mathbb{B}$ such that the corresponding density matrix ρ_S^{AB} can be written as

$$\rho_S^{AB} = \frac{1}{4} \int_{\mathbb{B} \times \mathbb{B}} d\mu (\mathbf{1} + \mathbf{u} \cdot \sigma^A) \otimes (\mathbf{1} + \mathbf{v} \cdot \sigma^B) \quad (9.6)$$

The integral is carried out over $(\mathbf{u}, \mathbf{v}) \in \mathbb{B} \times \mathbb{B}$.

The Pauli basis for 2×2 density matrices can be extended to 4×4 density matrices. Indeed every 4×4 density matrix can be written as

$$\rho^{AB} = \frac{1}{4} \left(\mathbf{1} \otimes \mathbf{1} + \mathbf{p} \cdot \sigma^A \otimes \mathbf{1} + \mathbf{1} \otimes \sigma^B \cdot \mathbf{q} + \sum_{\alpha, \beta=x, y, z} t_{\alpha\beta} \sigma_\alpha^A \otimes \sigma_\beta^B \right) \quad (9.7)$$

Here, $\mathbf{p}, \mathbf{q} \in \mathbb{R}^3$ represent the vector polarization and t is a 3×3 matrix representing the correlations. Indeed, the components of $\mathbf{p} = (p_x, p_y, p_z)$, $\mathbf{q} = (q_x, q_y, q_z)$ and t are the expectation values of the respective observables.

$$\begin{aligned} p_\alpha &= \text{Tr}(\rho^{AB} \sigma_\alpha^A \otimes \mathbf{1}) \\ q_\beta &= \text{Tr}(\rho^{AB} \mathbf{1} \otimes \sigma_\beta^B) \\ t_{\alpha\beta} &= \text{Tr}(\rho^{AB} \sigma_\alpha^A \otimes \sigma_\beta^B) \end{aligned} \quad (9.8)$$

For $\alpha, \beta = x, y, z$. Every 4×4 density matrix is uniquely characterized by this set of observable expectation values. The definition of a separable state can be formulated in

terms of these expectation values. A state ρ^{AB} with parameters \mathbf{p} , \mathbf{q} and t is separable iff there exists a measure μ defined over $\mathbb{B} \times \mathbb{B}$ such that

$$\begin{aligned} p_\alpha &= \int_{\mathbb{B} \times \mathbb{B}} u_\alpha d\mu \\ q_\beta &= \int_{\mathbb{B} \times \mathbb{B}} v_\beta d\mu \\ t_{\alpha\beta} &= \int_{\mathbb{B} \times \mathbb{B}} u_\alpha v_\beta d\mu \end{aligned} \quad (9.9)$$

where u_α are the components of the vector $\mathbf{u} \in \mathbb{B}$ and v_β are the components of the vector $\mathbf{v} \in \mathbb{B}$, that are integrated over. In other words, the state ρ^{AB} is separable iff \mathbf{p} , \mathbf{q} and t are the moments of some measure μ defined on $\mathbb{B} \times \mathbb{B}$. This follows from the following simple observation:

$$(\mathbf{1} + \mathbf{u} \cdot \sigma^A) \otimes (\mathbf{1} + \mathbf{v} \cdot \sigma^B) = \mathbf{1} \otimes \mathbf{1} + \mathbf{u} \cdot \sigma^A \otimes \mathbf{1} + \mathbf{1} \otimes \sigma^B \cdot \mathbf{v} + \sum_{\alpha, \beta=x, y, z} u_\alpha v_\beta \sigma_\alpha^A \otimes \sigma_\beta^B. \quad (9.10)$$

Therefore, the problem of deciding whether a given density matrix ρ^{AB} is separable or entangled can be reformulated as a truncated K -moment problem. This particular example has a complete solution and is known as the *positive partial transpose* criterion [128].

9.3 The Problem Statement

Let us consider a system of N spin-1/2 bosons. The problem that we can considering is the following: given a set of experimentally observed parameters $\{\langle S_x \rangle, \langle S_y \rangle, \langle S_z \rangle, \langle S_x^2 \rangle, \langle S_y^2 \rangle, \langle S_z^2 \rangle\}$, what can we say about the entanglement of the system? In order to formulate this problem as a TKMP, let us consider these observable expectation values for a separable state. The density matrix of a separable state can be written as $\int \rho_1 \otimes \dots \otimes \rho_N d\mu$. More precisely, we may write it as,

$$\rho = \int d\mu (1 + \mathbf{x}_1 \cdot \sigma) \otimes \dots \otimes (1 + \mathbf{x}_N \cdot \sigma) \quad (9.11)$$

where, $\mathbf{x}_i = (x_1, y_i, z_i)$ is a point inside the Bloch sphere, corresponding to the mixed state ρ_i and $\sigma = (\sigma_x, \sigma_y, \sigma_z)$ is the pseudovector of Pauli matrices. And μ is a measured defined over $\mathbb{B} \times \cdots \times \mathbb{B}$.

The observables listed above would then be

$$\begin{aligned}
\langle S_x \rangle &= \int (x_1 + \cdots + x_N) d\mu \\
\langle S_y \rangle &= \int (y_1 + \cdots + y_N) d\mu \\
\langle S_z \rangle &= \int (z_1 + \cdots + z_N) d\mu \\
\langle S_x^2 \rangle &= N + \int \sum_{i \neq j} x_i x_j d\mu \\
\langle S_y^2 \rangle &= N + \int \sum_{i \neq j} y_i y_j d\mu \\
\langle S_z^2 \rangle &= N + \int \sum_{i \neq j} z_i z_j d\mu
\end{aligned} \tag{9.12}$$

Thus, the problem of determining the entanglement of the system based on the six experimentally measured numbers $\{\langle S_x \rangle, \langle S_y \rangle, \langle S_z \rangle, \langle S_x^2 \rangle, \langle S_y^2 \rangle, \langle S_z^2 \rangle\}$ is a TKMP. Using the standard techniques from real algebraic geometry, we have developed asymptotically tight criteria for entanglement using these six observables, i.e., criteria that become tight in limit of large number of atoms, $N \rightarrow \infty$. The technical details of the criterion can be found in ref. [4].

CHAPTER 10

CONCLUSIONS AND OUTLOOK

In this chapter, we conclude with a set of technical applications, conceptual applications to other areas in physics and possible further advancements of the results presented in this thesis. We begin with geometric phases:

10.1 Geometric Phase

We have developed a new geometric phase for spin-1 (and higher) systems and experimentally studied a class of singular loops and observed their geometric phase accumulated in the spin fluctuation tensor. Singular loops are redolent of critical points of a phase transition. For instance, in a system of spin-1/2 fermions in a 1-dimensional Kitaev chain, the ground state at the critical point is represented by a Singular loop inside the Bloch sphere [129]. In the momentum basis, the ground state is a loop on the Bloch sphere. At finite temperature, however, the ground state is mixed and is represented by a loop inside the Bloch sphere. A phase transition in this system is characterized by a discontinuous change in the solid angle of the loop representing the ground state, or equivalently, in the number of windings of this loop around the center of the Bloch sphere. In ref. [129], it has been shown that the critical point of the transition from zero to one winding is a singular loop, where the ground state passes through the center. We hope that our development of geometric phases for such loops plays a role in understanding such critical behavior.

Furthermore, Berry's geometric phase has been used to study the topological charge of spin textures such as skyrmions, which are predominantly defined for spin-1/2 systems, where the spin vector is confined to the surface of the Bloch sphere. As is clear from chapter 1 and 2, the spin vector of a spin-1 system can be anywhere on or inside the Bloch ball and therefore, this opens up a larger class of skyrmion-like topological states. A study

of such states is a meaningful extension of our work.

The geometric phase developed in chapter 4 can be generalized to higher spins. The quantum state space of a spin- S system is the well known complex projective space $\mathbb{C}\mathbb{P}^{2S}$. In general, there is a well defined map from $\mathbb{C}\mathbb{P}^n$ to the Bloch ball, \mathbb{B} , which also represents the expectation value of the spin vector. One can accordingly define a horizontal lift in $\mathbb{C}\mathbb{P}^n$ for a loop in \mathbb{B} , using the Fubini-Study metric on $\mathbb{C}\mathbb{P}^n$. We make the following conjecture regarding the resulting geometric phase:

10.1.1 A Conjecture

If γ is a liftable loop in \mathbb{B} , and $\tilde{\gamma}$ is its horizontal lift in $\mathbb{C}\mathbb{P}^n$, and $R \in SO(3)$ is its geometric phase (defined by lifting it to $\mathbb{C}\mathbb{P}^2$), then the end point of the lift in $\mathbb{C}\mathbb{P}^n$ are related as: $\tilde{\gamma}(1) = \mathcal{D}(R)\tilde{\gamma}(0)$, where $\mathcal{D}(R) \in SU(n+1)$ is the representation of R in $SU(n+1)$.

This conjecture suggests that although the higher rank spin fluctuation tensors (i.e., operators of the form S_x^3 etc) are independent operators for higher spin systems, they do not carry any more geometric phase information than the second rank fluctuation tensor. We hope to be able to prove this conjecture mathematically.

10.2 Arbitrary Control and PVM

The technique of arbitrary control has been implemented in a system of Strontium atoms and can also be implemented in an ultracold cloud of Rubidium atoms. Experimental implementation of this technique opens up two broad areas of research

10.2.1 Dressed Hamiltonians

The tripod scheme can be used to add arbitrary non-interacting terms to the Hamiltonian of a BEC. This includes quadratic terms like Q_{xy}, Q_{yy} etc. This opens up a very large class of Hamiltonians that can be studied using a spin-1 BEC.

10.2.2 Single shot tomography of reduced density matrices

As described in chapter 7, the technique used in 1D PVMs can be applied to design single-shot tomography protocols, which have the unique advantage that the atoms do not need to be reloaded, thereby eliminating the shot-to-shot fluctuations from the measurement. This allows us to extract the reduced density matrix of a many-body system.

10.3 Staircase Phenomena in a BEC

We have described three examples where atomic ensembles described by different spin-squeezing Hamiltonians display a staircase structure in their magnetizations as a response to the external tuning of a continuous control parameter. This phenomena can be observed in spin-1 ferromagnetic ^{87}Rb and anti-ferromagnetic ^{23}Na condensates, using current experimental techniques. Maintaining adiabaticity is crucial for such experiments. Indeed, any deviation from adiabaticity would result in superpositions of quantum states that would smear out the staircase. Nevertheless, as we show in chapter 8, observing this effect is within the limitations of many of the existing physical systems. Observing this phenomena can also lead to high precision magnetometers.

10.4 Many Body Entanglement

The technique developed in ref.[4] is general — it invokes a very fundamental connection between the two fields, many body entanglement and real algebraic geometry. The same technique can be used to develop entanglement criteria for spin-1 systems and more generally, entanglement criteria for spatially separated modes of condensates. The resulting criteria can be readily applied experimentally in a BEC.

Appendices

APPENDIX A
SOME FORMULAE FOR SPIN-1 SYSTEMS

In this appendix, we provide a set of useful formulae pertaining to the dynamics of three level atoms, and their derivation. We also provide a few techniques of working with 3×3 matrices, some of which are generalizable to higher dimensions. We begin a set of basic properties of 3×3 Hermitian matrices.

A.1 Hermitian Matrices

A 3×3 matrix X is Hermitian iff it satisfies $X^\dagger = X$. It is straightforward to see that this constraint leave 9 free parameters. That is, the space of 3×3 Hermitian operators is a 9 dimensional vector space. Quantum mechanical observables and Hamiltonians are largely represented by Hermitian operators. Therefore this 9 dimensional space is central to the study of spin-1 physics. There are two standard set of basis vectors for this vector space. One of them is the so-called Gell Mann matrices together with the identity I , given by:

$$\begin{aligned}
 g_1 &= \frac{1}{2} \begin{pmatrix} 0 & 1 & 0 \\ 1 & 0 & 0 \\ 0 & 0 & 0 \end{pmatrix}; g_2 = \frac{1}{2} \begin{pmatrix} 0 & -i & 0 \\ i & 0 & 0 \\ 0 & 0 & 0 \end{pmatrix}; g_3 = \frac{1}{2} \begin{pmatrix} 1 & 0 & 0 \\ 0 & -1 & 0 \\ 0 & 0 & 0 \end{pmatrix} \\
 g_4 &= \frac{1}{2} \begin{pmatrix} 0 & 0 & 1 \\ 0 & 0 & 0 \\ 1 & 0 & 0 \end{pmatrix}; g_5 = \frac{1}{2} \begin{pmatrix} 0 & 0 & -i \\ 0 & 0 & 0 \\ i & 0 & 0 \end{pmatrix}; g_6 = \frac{1}{2} \begin{pmatrix} 0 & 0 & 0 \\ 0 & 0 & 1 \\ 0 & 1 & 0 \end{pmatrix} \\
 g_7 &= \frac{1}{2} \begin{pmatrix} 0 & 0 & 0 \\ 0 & 0 & -i \\ 0 & i & 0 \end{pmatrix}; g_8 = \frac{1}{2\sqrt{3}} \begin{pmatrix} 1 & 0 & 0 \\ 0 & 1 & 0 \\ 0 & 0 & -2 \end{pmatrix}
 \end{aligned} \tag{A.1}$$

An alternate basis is given by the identity I , the three spin operators S_x, S_y, S_z and the five nematic operators, $\{S_i, S_j\}$:

$$S_x = \frac{1}{\sqrt{2}} \begin{pmatrix} 0 & 1 & 0 \\ 1 & 0 & 1 \\ 0 & 1 & 0 \end{pmatrix}; S_y = \frac{1}{\sqrt{2}} \begin{pmatrix} 0 & -i & 0 \\ i & 0 & -i \\ 0 & i & 0 \end{pmatrix}; S_z = \begin{pmatrix} 1 & 0 & 0 \\ 0 & 0 & 0 \\ 0 & 0 & -1 \end{pmatrix} \quad (\text{A.2})$$

And

$$S_x^2 = \frac{1}{2} \begin{pmatrix} 1 & 0 & 1 \\ 0 & 2 & 0 \\ 1 & 0 & 1 \end{pmatrix}; S_y^2 = \frac{1}{2} \begin{pmatrix} 1 & 0 & -1 \\ 0 & 2 & 0 \\ -1 & 0 & 1 \end{pmatrix}; S_z^2 = \begin{pmatrix} 1 & 0 & 0 \\ 0 & 0 & 0 \\ 0 & 0 & 1 \end{pmatrix}$$

$$\{S_x, S_y\} = \begin{pmatrix} 0 & 0 & -i \\ 0 & 0 & 0 \\ i & 0 & 0 \end{pmatrix}; \{S_y, S_z\} = \frac{1}{\sqrt{2}} \begin{pmatrix} 0 & -i & 0 \\ i & 0 & i \\ 0 & -i & 0 \end{pmatrix}; \{S_x, S_z\} = \frac{1}{\sqrt{2}} \begin{pmatrix} 0 & 1 & 0 \\ 1 & 0 & -1 \\ 0 & -1 & 0 \end{pmatrix} \quad (\text{A.3})$$

Note that $S_x^2 + S_y^2 + S_z^2 = 2I$ and therefore, only five out of the six quadratic operators above are independent. The nine operators generate the unitary group $U(3)$. That is every $U \in U(3)$ can be written as $U = \exp\{iX\}$, where X is a 3×3 Hermitian. The eight operators other than the identity generate the special unitary group $SU(3)$. The three spin operators $\{S_x, S_y, S_z\}$ generate the $SO(3)$ subgroup of $SU(3)$.

The eigenvalues of the spin operators are $0, \pm 1$ and so are the eigenvalues of any operator of the form $S_{\hat{n}} = \vec{n} \cdot \vec{S}$ for some unit vector \hat{n} , i.e., the spin operator with any quantization direction. Thus, the characteristic equation of any such operator is $x^3 - x = 0$, of which the eigenvalues are roots. This, along with the Cayley-Hamilton theorem provides us with an important formula: $S_{\hat{n}}^3 - S_{\hat{n}} = 0$. In other words, $S_{\hat{n}}^3 = S_{\hat{n}}$, and this implies that all even

exponents of $S_{\hat{n}}$ are equal to each other and so are all odd exponents. That is,

$$\begin{aligned} S_{\hat{n}}^{2k+1} &= S_{\hat{n}} \\ S_{\hat{n}}^{2k} &= S_{\hat{n}}^2 \end{aligned} \tag{A.4}$$

This enables us to evaluate the unitaries generated by the spin operators, which we describe in the next section.

A.2 Unitaries Generated by the Spin Operators

In this section, we show how the matrix corresponding a unitary operator of the form $e^{i\theta S_{\hat{n}}}$ can be computed. For the case of spin-1/2 systems, unitaries of the form $e^{i\theta \vec{\sigma} \cdot \hat{n}}$ has a standard formula,

$$e^{i\theta \vec{\sigma} \cdot \hat{n}} = I \cos \frac{\theta}{2} + \vec{\sigma} \cdot \hat{n} \sin \frac{\theta}{2} \tag{A.5}$$

Here, $\vec{\sigma}$ is the pseudovector of Pauli matrices. The equivalent formula for spin-1 systems is

$$e^{i\theta S_{\hat{n}}} = I - S_{\hat{n}}^2 + S_{\hat{n}}^2 \cos \theta + i S_{\hat{n}} \sin \theta \tag{A.6}$$

This, like Eq. A.5 is derived using the Taylor expansion for $e^{i\theta S_{\hat{n}}}$:

$$e^{i\theta S_{\hat{n}}} = I + i\theta S_{\hat{n}} + \frac{1}{2!}(i\theta)^2(S_{\hat{n}})^2 + \frac{1}{3!}(i\theta)^3(S_{\hat{n}})^3 + \dots \tag{A.7}$$

We can now use Eq. A.4, to reduce the exponents of $S_{\hat{n}}$ that appear in the above equation. Doing so, we split the sum into two parts — the even powers of $S_{\hat{n}}$ all reduce to $S_{\hat{n}}^2$ and their coefficient would be $1 - \cos \theta$; the odd powers would be reduced to $S_{\hat{n}}$, with a coefficient equal to $\sin \theta$. Thus, we arrive at Eq. A.6. This expression is quite useful, as we show in the next section.

A.3 RF Spectrum

In this section, we use Eq. A.6 to derive expressions for the unitary that corresponds to an RF rotation and further use to derive the expression for an RF spectrum. For a system under a field in the z direction with a strength given by ω_0 , the Hamiltonian is $H = \omega_0 S_z$. Adding a second field normal to the z direction, rotating at a frequency ω , with a strength Ω makes the Hamiltonian $H = \omega_0 S_z + \Omega e^{-it\omega S_z} S_x e^{it\omega S_z}$. In the rotating frame this Hamiltonian is $H' = (\omega_0 - \omega) S_z + \Omega S_x$. This is the typical Hamiltonian for a spin-1 RF rotation. If the rotating field is pulsed on for a duration of T , the unitary that has been induced on the system, in the rotating frame is given by

$$U = e^{iH'T} = \exp\{iT(\Omega S_x + (\omega_0 - \omega) S_z)\} \quad (\text{A.8})$$

The operator $S = \frac{\Omega}{\sqrt{\Omega^2 + (\omega_0 - \omega)^2}} S_x + \frac{(\omega_0 - \omega)}{\sqrt{\Omega^2 + (\omega_0 - \omega)^2}} S_z$ is a spin operator, i.e., it is equal to $S_{\hat{n}}$ for unit vector $\hat{n} = \left(\frac{\Omega}{\sqrt{\Omega^2 + (\omega_0 - \omega)^2}}, 0, \frac{(\omega_0 - \omega)}{\sqrt{\Omega^2 + (\omega_0 - \omega)^2}} \right)$. Thus, we may write the unitary as

$$U = e^{i\theta S} = I - S^2 + S^2 \cos \theta + iS \sin \theta \quad (\text{A.9})$$

where, $\theta = T\sqrt{\Omega^2 + (\omega_0 - \omega)^2}$. The starting state is usually $|0\rangle$, i.e., the $m = 0$ state. Therefore, the population of the $m = 0$ state after the RF pulse is given by

$$\rho_0 = |\langle 0|U|0\rangle|^2 = \left(1 - \frac{\Omega^2}{\Omega^2 + (\omega_0 - \omega)^2} \left(1 - \cos \left(T\sqrt{\Omega^2 + (\omega_0 - \omega)^2} \right) \right) \right)^2 \quad (\text{A.10})$$

Thus we arrive at the expression for the RF spectrum.

REFERENCES

- [1] A. Uhlmann, “Parallel transport and “quantum holonomy” along density operators,” *Reports on Mathematical Physics*, vol. 24, no. 2, pp. 229–240, 1986.
- [2] A Uhlmann, “On Berry phases along mixtures of states,” *Annalen der Physik*, vol. 501, no. 1, pp. 63–69, 1989.
- [3] A. Uhlmann, “Geometric phases and related structures,” *Reports on Mathematical Physics*, vol. 36, no. 2, pp. 461–481, 1995.
- [4] H. M. Bharath, “Non-negative symmetric polynomials and entangled bosons,” Master’s thesis, School of Mathematics, Georgia Institute of Technology, Jul. 2018.
- [5] Bharath H. M., “Non-abelian geometric phases carried by the spin fluctuation tensor,” *Journal of Mathematical Physics*, vol. 59, no. 6, p. 062105, 2018.
- [6] H. M. Bharath, M. S. Chapman, and C. A. R. S. de Melo, “Staircase in magnetization and entanglement entropy of spin squeezed condensates,” *ArXiv e-prints 1804.03745*, Apr. 2018.
- [7] F. Bloch, “Nuclear induction,” *Phys. Rev.*, vol. 70, pp. 460–474, 7-8 1946.
- [8] I. Bengtsson and K. Życzkowski, *Geometry of Quantum States: An Introduction to Quantum Entanglement*. Cambridge University Press, 2006, ISBN: 978-0521891400.
- [9] M. V. Berry, “Quantal phase factors accompanying adiabatic changes,” *Proceedings of the Royal Society of London A: Mathematical, Physical and Engineering Sciences*, vol. 392, no. 1802, pp. 45–57, 1984.
- [10] B. Simon, “Holonomy, the quantum adiabatic theorem, and Berry’s phase,” *Phys. Rev. Lett.*, vol. 51, pp. 2167–2170, 24 1983.
- [11] E. Sjöqvist, A. K. Pati, A. Ekert, J. S. Anandan, M. Ericsson, D. K. L. Oi, and V. Vedral, “Geometric phases for mixed states in interferometry,” *Phys. Rev. Lett.*, vol. 85, pp. 2845–2849, 14 2000.
- [12] J. Samuel and R. Bhandari, “General setting for Berry’s phase,” *Phys. Rev. Lett.*, vol. 60, pp. 2339–2342, 23 1988.

- [13] S. Pancharatnam, “Generalized theory of interference, and its applications,” *Proceedings of the Indian Academy of Sciences - Section A*, vol. 44, no. 5, pp. 247–262, 1956.
- [14] Y. Aharonov and J. Anandan, “Phase change during a cyclic quantum evolution,” *Phys. Rev. Lett.*, vol. 58, pp. 1593–1596, 16 1987.
- [15] C. Miniatura, C. Sire, J. Baudon, and J. Bellissard, “Geometrical phase factor for a non-hermitian Hamiltonian,” *EPL (Europhysics Letters)*, vol. 13, no. 3, p. 199, 1990.
- [16] D. Chruscinski and A. Jamiolkowski, *Geometric Phases in Classical and Quantum Mechanics*, ser. Progress in Mathematical Physics. Birkhäuser Boston, 2004, ISBN: 9780817642822.
- [17] J. Anandan, J. Christian, and K. Wanelik, “Resource letter GPP-1: Geometric phases in physics,” *American Journal of Physics*, vol. 65, no. 3, pp. 180–185, 1997.
- [18] F. Wilczek and A. Shapere, *Geometric Phases in Physics*, ser. Advanced series in mathematical physics. World Scientific, 1989, ISBN: 9789971506216.
- [19] R. Y. Chiao and Y.-S. Wu, “Manifestations of Berry’s topological phase for the photon,” *Phys. Rev. Lett.*, vol. 57, pp. 933–936, 8 1986.
- [20] A. Tomita and R. Y. Chiao, “Observation of Berry’s topological phase by use of an optical fiber,” *Phys. Rev. Lett.*, vol. 57, pp. 937–940, 8 1986.
- [21] F. D. M. Haldane, “Path dependence of the geometric rotation of polarization in optical fibers,” *Opt. Lett.*, vol. 11, no. 11, pp. 730–732, 1986.
- [22] T. H. Chyba, R. Simon, L. J. Wang, and L. Mandel, “Measurement of the pancharatnam phase for a light beam,” *Opt. Lett.*, vol. 13, no. 7, pp. 562–564, 1988.
- [23] R. Bhandari, “Observation of non-integrable geometric phase on the poincar sphere,” *Physics Letters A*, vol. 133, no. 1, pp. 1–3, 1988.
- [24] R. Bhandari and J. Samuel, “Observation of topological phase by use of a laser interferometer,” *Phys. Rev. Lett.*, vol. 60, pp. 1211–1213, 13 1988.
- [25] R. Y. Chiao, A. Antaramian, K. M. Ganga, H. Jiao, S. R. Wilkinson, and H. Nathe, “Observation of a topological phase by means of a nonplanar mach-zehnder interferometer,” *Phys. Rev. Lett.*, vol. 60, pp. 1214–1217, 13 1988.
- [26] P. G. Kwiat and R. Y. Chiao, “Observation of a nonclassical Berry’s phase for the photon,” *Phys. Rev. Lett.*, vol. 66, pp. 588–591, 5 1991.

- [27] M. Segev, R. Solomon, and A. Yariv, “Manifestation of Berry’s phase in image-bearing optical beams,” *Phys. Rev. Lett.*, vol. 69, pp. 590–592, 4 1992.
- [28] P. Hariharan and M. Roy, “A geometric-phase interferometer,” *Journal of Modern Optics*, vol. 39, no. 9, pp. 1811–1815, 1992. eprint: <http://dx.doi.org/10.1080/09500349214551881>.
- [29] P. Hariharan, M. Roy, P. Robinson, and J. O’Byrne, “The geometric phase,” *Journal of Modern Optics*, vol. 40, no. 5, pp. 871–877, 1993. eprint: <http://dx.doi.org/10.1080/09500349314550881>.
- [30] P. Hariharan, K. G. Larkin, and M. Roy, “The geometric phase: Interferometric observations with white light,” *Journal of Modern Optics*, vol. 41, no. 4, pp. 663–667, 1994. eprint: <http://dx.doi.org/10.1080/09500349414550681>.
- [31] T. P. Grayson, J. R. Torgerson, and G. A. Barbosa, “Observation of a nonlocal pancharatnam phase shift in the process of induced coherence without induced emission,” *Phys. Rev. A*, vol. 49, pp. 626–628, 1 1994.
- [32] A. G. Wagh and V. C. Rakhecha, “On measuring the pancharatnam phase. I. interferometry,” *Physics Letters A*, vol. 197, no. 2, pp. 107–111, 1995.
- [33] A. Wagh and V. C. Rakhecha, “On measuring the pancharatnam phase. II. SU(2) polarimetry,” *Physics Letters A*, vol. 197, no. 2, pp. 112–115, 1995.
- [34] T. Bitter and D. Dubbers, “Manifestation of Berry’s topological phase in neutron spin rotation,” *Phys. Rev. Lett.*, vol. 59, pp. 251–254, 3 1987.
- [35] D. Dubbers, “Measurement of the Berry phase with polarized neutrons,” *Physica B+C*, vol. 151, no. 1, pp. 93–95, 1988.
- [36] H. Weinfurter and G. Badurek, “Measurement of Berry’s phase for noncyclic evolution,” *Phys. Rev. Lett.*, vol. 64, pp. 1318–1321, 12 1990.
- [37] D. Suter, G. C. Chingas, R. A. Harris, and A. Pines, “Berry’s phase in magnetic resonance,” *Molecular Physics*, vol. 61, no. 6, pp. 1327–1340, 1987.
- [38] R. Tycko, “Adiabatic rotational splittings and Berry’s phase in nuclear quadrupole resonance,” *Phys. Rev. Lett.*, vol. 58, pp. 2281–2284, 22 1987.
- [39] D. Suter, K. T. Mueller, and A. Pines, “Study of the Aharonov-Anandan quantum phase by NMR interferometry,” *Phys. Rev. Lett.*, vol. 60, pp. 1218–1220, 13 1988.

- [40] C. L. Webb, R. M. Godun, G. S. Summy, M. K. Oberthaler, P. D. Featonby, C. J. Foot, and K. Burnett, “Measurement of Berry’s phase using an atom interferometer,” *Phys. Rev. A*, vol. 60, R1783–R1786, 3 1999.
- [41] A. Morinaga, T. Aoki, and M. Yasuhara, “Dependence of Berry’s phase for atom on a sign of the g factor in the rotating magnetic field,” *Phys. Rev. A*, vol. 71, p. 054 101, 5 2005.
- [42] A. Morinaga, K. Toriyama, H. Narui, T. Aoki, and H. Imai, “Dependence of Berry’s phase on the sign of the g factor for conical rotation of a magnetic field, measured without any dynamical phase shift,” *Phys. Rev. A*, vol. 83, p. 052 109, 5 2011.
- [43] M. Ericsson, D. Achilles, J. T. Barreiro, D. Branning, N. A. Peters, and P. G. Kwiat, “Measurement of geometric phase for mixed states using single photon interferometry,” *Phys. Rev. Lett.*, vol. 94, p. 050 401, 5 2005.
- [44] J. Klepp, S. Sponar, Y. Hasegawa, E. Jericha, and G. Badurek, “Noncyclic pancharatanam phase for mixed state evolution in neutron polarimetry,” *Physics Letters A*, vol. 342, no. 12, pp. 48–52, 2005.
- [45] J. Klepp, S. Sponar, S. Filipp, M. Lettner, G. Badurek, and Y. Hasegawa, “Observation of nonadditive mixed-state phases with polarized neutrons,” *Phys. Rev. Lett.*, vol. 101, p. 150 404, 15 2008.
- [46] J. Du, P. Zou, M. Shi, L. C. Kwek, J.-W. Pan, C. H. Oh, A. Ekert, D. K. L. Oi, and M. Ericsson, “Observation of geometric phases for mixed states using NMR interferometry,” *Phys. Rev. Lett.*, vol. 91, p. 100 403, 10 2003.
- [47] A. Ghosh and A. Kumar, “Experimental measurement of mixed state geometric phase by quantum interferometry using NMR,” *Physics Letters A*, vol. 349, no. 14, pp. 27–36, 2006.
- [48] A. Morinaga and K. Nanri, “Noncyclic Berry phase and scalar aharonov-bohm phase for the spin-redirected evolution in an atom interferometer,” *Phys. Rev. A*, vol. 86, p. 022 105, 2 2012.
- [49] D. J. Richardson, A. I. Kilvington, K. Green, and S. K. Lamoreaux, “Demonstration of Berry’s phase using stored ultracold neutrons,” *Phys. Rev. Lett.*, vol. 61, pp. 2030–2033, 18 1988.
- [50] P. J. Leek, J. M. Fink, A. Blais, R. Bianchetti, M. Göppl, J. M. Gambetta, D. I. Schuster, L. Frunzio, R. J. Schoelkopf, and A. Wallraff, “Observation of Berry’s phase in a solid-state qubit,” *Science*, vol. 318, no. 5858, pp. 1889–1892, 2007.

- [51] J. Zhu, M. Shi, V. Vedral, X. Peng, D. Suter, and J. Du, “Experimental demonstration of a unified framework for mixed-state geometric phases,” *EPL (Europhysics Letters)*, vol. 94, no. 2, p. 20007, 2011.
- [52] A. Carollo, I. Fuentes-Guridi, M. F. M. c. Santos, and V. Vedral, “Geometric phase in open systems,” *Phys. Rev. Lett.*, vol. 90, p. 160402, 16 2003.
- [53] G. De Chiara and G. M. Palma, “Berry phase for a spin $1/2$ particle in a classical fluctuating field,” *Phys. Rev. Lett.*, vol. 91, p. 090404, 9 2003.
- [54] S. Filipp, J. Klepp, Y. Hasegawa, C. Plonka-Spehr, U. Schmidt, P. Geltenbort, and H. Rauch, “Experimental demonstration of the stability of Berry’s phase for a spin- $1/2$ particle,” *Phys. Rev. Lett.*, vol. 102, p. 030404, 3 2009.
- [55] S. Berger, M. Pechal, A. A. Abdumalikov, C. Eichler, L. Steffen, A. Fedorov, A. Wallraff, and S. Filipp, “Exploring the effect of noise on the Berry phase,” *Phys. Rev. A*, vol. 87, p. 060303, 6 2013.
- [56] E. Sjöqvist, V. Azimi Mousolou, and C. M. Canali, “Conceptual aspects of geometric quantum computation,” *Quantum Information Processing*, pp. 1–17, 2016.
- [57] E. Sjöqvist, “Geometric phases in quantum information,” *International Journal of Quantum Chemistry*, vol. 115, no. 19, pp. 1311–1326, 2015.
- [58] S.-L. Zhu and Z. D. Wang, “Implementation of universal quantum gates based on nonadiabatic geometric phases,” *Phys. Rev. Lett.*, vol. 89, p. 097902, 9 2002.
- [59] C. Zu, W.-B. Wang, L. He, W.-G. Zhang, C.-Y. Dai, F. Wang, and L.-M. Duan, “Experimental realization of universal geometric quantum gates with solid-state spins,” *Nature*, vol. 514, no. 7520, pp. 72–75, 2014.
- [60] C. G. Yale, F. J. Heremans, B. B. Zhou, A. Auer, G. Burkard, and D. D. Awschalom, “Optical manipulation of the Berry phase in a solid-state spin qubit,” *Nature Photonics*, vol. 10, no. 3, pp. 184–189, 2016.
- [61] H. M. Bharath, M. Boguslawski, M. Barrios, L. Xin, and M. S. Chapman, “Singular Loops and their Non-Abelian Geometric Phases in Spin-1 Ultracold Atoms,” *ArXiv e-prints 1801.00586*, Jan. 2018.
- [62] A. K. Pati, “Relation between “phases” and “distance” in quantum evolution,” *Physics Letters A*, vol. 159, no. 3, pp. 105–112, 1991.
- [63] E. Sjöqvist, V. Azimi Mousolou, and C. M. Canali, “Conceptual aspects of geometric quantum computation,” *Quantum Information Processing*, vol. 15, pp. 3995–4011, Oct. 2016. arXiv: 1311.7470 [quant-ph].

- [64] N. Mukunda and R. Simon, “Quantum kinematic approach to the geometric phase. I. General formalism,” *Annals of Physics*, vol. 228, no. 2, pp. 205–268, 1993.
- [65] N. Mukunda and R. Simon, “Quantum kinematic approach to the geometric phase. II. The case of unitary group representations,” *Annals of Physics*, vol. 228, no. 2, pp. 269–340, 1993.
- [66] J. Anandan, “Non-adiabatic non-abelian geometric phase,” *Physics Letters A*, vol. 133, no. 4, pp. 171–175, 1988.
- [67] F. Wilczek and A. Zee, “Appearance of gauge structure in simple dynamical systems,” *Phys. Rev. Lett.*, vol. 52, pp. 2111–2114, 24 1984.
- [68] J. M. Robbins and M. V. Berry, “A geometric phase for $m=0$ spins,” *Journal of Physics A: Mathematical and General*, vol. 27, no. 12, p. L435, 1994.
- [69] F. Apery, *Models of the Real Projective Planes*. Vieweg+Teubner Verlag, 1987, ISBN: 978-3-322-89569-1.
- [70] S. S. Chern, W. H. Chen, and K. S. Lam, *Lectures on Differential Geometry*, ser. Series On University Mathematics Vol. 1. World Scientific, 1998, ISBN: 978-9810241827.
- [71] P. M. Alberti and A. Uhlmann, “On bures distance and $*$ -algebraic transition probability between inner derived positive linear forms over $w*$ -algebras,” *Acta Applicandae Mathematica*, vol. 60, no. 1, pp. 1–37, 2000.
- [72] A. Uhlmann, “Transition probability (fidelity) and its relatives,” *Foundations of Physics*, vol. 41, no. 3, pp. 288–298, 2011.
- [73] S. Kobayashi and K. Nomizu, *Foundations of Differential Geometry Vol 1*. Interscience Publishers, 1963, ISBN: 978-0471157335.
- [74] H. Geiges and C. Lange, “Seifert fibrations of lens spaces,” *ArXiv e-prints*, Aug. 2016. arXiv: 1608.06844 [math.GT].
- [75] E. Majorana, “Atomi orientati in campo magnetico variabile,” *Il Nuovo Cimento (1924-1942)*, vol. 9, no. 2, pp. 43–50, 1932.
- [76] P. Bruno, “Quantum geometric phase in majorana’s stellar representation: Mapping onto a many-body aharonov-bohm phase,” *Phys. Rev. Lett.*, vol. 108, p. 240402, 24 2012.
- [77] S. Kobayashi and K. Nomizu, *Foundations of Differential Geometry Vol 2*. Interscience Publishers, 1969, ISBN: 978-0471157335.

- [78] A. K. Pati, “Geometric aspects of noncyclic quantum evolutions,” *Phys. Rev. A*, vol. 52, pp. 2576–2584, 4 1995.
- [79] E. Bookjans, “Relative number squeezing in a spin-1 Bose Einstein condensate,” PhD thesis, The school of Physics, Georgia Institute of Technology, Jul. 2010.
- [80] F. Bloch and A. Siegert, “Magnetic resonance for nonrotating fields,” *Phys. Rev.*, vol. 57, pp. 522–527, 6 1940.
- [81] M. S. Shahriar, P. Pradhan, and J. Morzinski, “Driver-phase-correlated fluctuations in the rotation of a strongly driven quantum bit,” *Phys. Rev. A*, vol. 69, p. 032 308, 3 2004.
- [82] J. Spiegelberg and E. Sjöqvist, “Validity of the rotating-wave approximation in nonadiabatic holonomic quantum computation,” *Phys. Rev. A*, vol. 88, p. 054 301, 5 2013.
- [83] Erik Sjöqvist, “Nonadiabatic holonomic single-qubit gates in off-resonant lambda systems,” *Physics Letters A*, vol. 380, no. 1, pp. 65 –67, 2016.
- [84] F. Leroux, K. Pandey, R. Rebhi, F. Chevy, C. Miniatura, B. Grémaud, D. Wilkowski, R. Rehbi, and B. Gremaud, “Non-Abelian adiabatic geometric transformations in a cold Strontium gas,” *ArXiv e-prints*, Feb. 2018. arXiv: 1802 . 08418 [quant-ph].
- [85] D. J. Thouless, M. Kohmoto, M. P. Nightingale, and M. den Nijs, “Quantized Hall conductance in a two-dimensional periodic potential,” *Phys. Rev. Lett.*, vol. 49, pp. 405–408, 6 1982.
- [86] P. Streda, “Theory of quantised Hall conductivity in two dimensions,” *Journal of Physics C: Solid State Physics*, vol. 15, no. 22, p. L717, 1982.
- [87] K. von Klitzing, “The quantized Hall effect,” *Rev. Mod. Phys.*, vol. 58, pp. 519–531, 3 1986.
- [88] H. L. Stormer, D. C. Tsui, and A. C. Gossard, “The fractional quantum Hall effect,” *Rev. Mod. Phys.*, vol. 71, S298–S305, 2 1999.
- [89] N. K. Wilkin and J. M. F. Gunn, “Condensation of “composite bosons” in a rotating BEC,” *Phys. Rev. Lett.*, vol. 84, pp. 6–9, 1 2000.
- [90] N. R. Cooper, N. K. Wilkin, and J. M. F. Gunn, “Quantum phases of vortices in rotating Bose Einstein condensates,” *Phys. Rev. Lett.*, vol. 87, p. 120 405, 12 2001.

- [91] J. W. Reijnders, F. J. M. van Lankvelt, K. Schoutens, and N. Read, “Quantum hall states and boson triplet condensate for rotating spin-1 bosons,” *Phys. Rev. Lett.*, vol. 89, p. 120401, 12 2002.
- [92] N. Cooper, “Rapidly rotating atomic gases,” *Advances in Physics*, vol. 57, no. 6, pp. 539–616, 2008.
- [93] S. Viefers, “Quantum hall physics in rotating boseeinstein condensates,” *Journal of Physics: Condensed Matter*, vol. 20, no. 12, p. 123202, 2008.
- [94] S. Furukawa and M. Ueda, “Integer quantum Hall state in two-component bose gases in a synthetic magnetic field,” *Phys. Rev. Lett.*, vol. 111, p. 090401, 9 2013.
- [95] T. Graß, B. Juliá-Díaz, and M. Lewenstein, “Topological phases in small quantum Hall samples,” *Phys. Rev. A*, vol. 89, p. 013623, 1 2014.
- [96] V. Meyer, M. A. Rowe, D. Kielpinski, C. A. Sackett, W. M. Itano, C. Monroe, and D. J. Wineland, “Experimental demonstration of entanglement-enhanced rotation angle estimation using trapped ions,” *Phys. Rev. Lett.*, vol. 86, pp. 5870–5873, 26 2001.
- [97] Y. P. Huang and M. G. Moore, “Optimized double-well quantum interferometry with gaussian squeezed states,” *Phys. Rev. Lett.*, vol. 100, p. 250406, 25 2008.
- [98] I. D. Leroux, M. H. Schleier-Smith, “Implementation of cavity squeezing of a collective atomic spin,” *Phys. Rev. Lett.*, vol. 104, p. 073602, 7 2010.
- [99] C. Gross, T. Zibold, E. Nicklas, J. Estève, and M. K. Oberthaler, “Nonlinear atom interferometer surpasses classical precision limit,” *Nature*, vol. 464, pp. 1165–1169, Apr. 2010.
- [100] C. D. Hamley, C. S. Gerving, T. M. Hoang, E. M. Bookjans, and M. S. Chapman, “Spin-nematic squeezed vacuum in a quantum gas,” *Nature Physics*, vol. 8, pp. 305–308, Apr. 2012.
- [101] J. G. Bohnet, B. C. Sawyer, J. W. Britton, M. L. Wall, A. M. Rey, M. Foss-Feig, and J. J. Bollinger, “Quantum spin dynamics and entanglement generation with hundreds of trapped ions,” *Science*, vol. 352, no. 6291, pp. 1297–1301, 2016.
- [102] K. C. Cox, G. P. Greve, J. M. Weiner, and J. K. Thompson, “Deterministic squeezed states with collective measurements and feedback,” *Phys. Rev. Lett.*, vol. 116, p. 093602, 9 2016.

- [103] O. Hosten, N. J. Engelsen, R. Krishnakumar, and M. A. Kasevich, “Measurement noise 100 times lower than the quantum-projection limit using entangled atoms,” *Nature*, vol. 529, pp. 505–508, 2016.
- [104] M. Kitagawa and M. Ueda, “Squeezed spin states,” *Phys. Rev. A*, vol. 47, pp. 5138–5143, 6 1993.
- [105] R. H. Dicke, “Coherence in spontaneous radiation processes,” *Phys. Rev.*, vol. 93, pp. 99–110, 1 1954.
- [106] W. Chen, J. Hu, Y. Duan, B. Braverman, H. Zhang, “Carving complex many-atom entangled states by single-photon detection,” *Phys. Rev. Lett.*, vol. 115, p. 250 502, 25 2015.
- [107] R. McConnell, H. Zhang, J. Hu, M. H. Schleier-Smith, “Generating entangled spin states for quantum metrology by single-photon detection,” *Phys. Rev. A*, vol. 88, p. 063 802, 6 2013.
- [108] H. Strobel, W. Muessel, D. Linnemann, T. Zibold, D. B. Hume, L. Pezzè, A. Smerzi, and M. K. Oberthaler, “Fisher information and entanglement of non-gaussian spin states,” *Science*, vol. 345, no. 6195, pp. 424–427, 2014.
- [109] A. S. Sørensen and K. Mølmer, “Entangling atoms in bad cavities,” *Phys. Rev. A*, vol. 66, p. 022 314, 2 2002.
- [110] J. Borregaard, E. J. Davis, G. S. Bentsen, M. H. Schleier-Smith, and A. S. Sørensen, “One- and two-axis squeezing of atomic ensembles in optical cavities,” *New Journal of Physics*, vol. 19, no. 9, p. 093 021, 2017.
- [111] S. J. Masson, M. D. Barrett, and S. Parkins, “Cavity QED engineering of spin dynamics and squeezing in a spinor gas,” *Phys. Rev. Lett.*, vol. 119, p. 213 601, 21 2017.
- [112] P. Böhi, M. F. Riedel, J. Hoffrogge, J. Reichel, T. W. Hänsch, and P. Treutlein, “Coherent manipulation of Bose Einstein condensates with state-dependent microwave potentials on an atom chip,” *Nature Physics*, vol. 5, pp. 592–597, Aug. 2009.
- [113] M. Fadel, T. Zibold, B. Décamps, and P. Treutlein, “Spatial entanglement patterns and einstein-podolsky-rosen steering in Bose Einstein condensates,” *Science*, vol. 360, no. 6387, pp. 409–413, 2018.
- [114] H. Bernien, S. Schwartz, A. Keesling, H. Levine, A. Omran, H. Pichler, S. Choi, A. S. Zibrov, M. Endres, M. Greiner, V. Vuletić, and M. D. Lukin, “Probing many-body dynamics on a 51-atom quantum simulator,” *Nature*, vol. 551, pp. 579–584, Nov. 2017.

- [115] J. Zhang, G. Pagano, P. W. Hess, A. Kyprianidis, P. Becker, H. Kaplan, A. V. Gorshkov, Z.-X. Gong, and C. Monroe, “Observation of a many-body dynamical phase transition with a 53-qubit quantum simulator,” *Nature*, vol. 551, pp. 601–604, Nov. 2017.
- [116] P. Richerme, C. Senko, S. Korenblit, J. Smith, A. Lee, R. Islam, W. C. Campbell, and C. Monroe, “Quantum catalysis of magnetic phase transitions in a quantum simulator,” *Phys. Rev. Lett.*, vol. 111, p. 100 506, 10 2013.
- [117] T. M. Hoang, H. M. Bharath, M. J. Boguslawski, M. Anquez, B. A. Robbins, and M. S. Chapman, “Adiabatic quenches and characterization of amplitude excitations in a continuous quantum phase transition,” *Proceedings of the National Academy of Sciences*, vol. 113, no. 34, pp. 9475–9479, 2016. eprint: <http://www.pnas.org/content/113/34/9475.full.pdf>.
- [118] A. Altland, V. Gurarie, T. Kriecherbauer, and A. Polkovnikov, “Nonadiabaticity and large fluctuations in a many-particle landau-zener problem,” *Phys. Rev. A*, vol. 79, p. 042 703, 4 2009.
- [119] W. Müssel, “Scalable spin squeezing for quantum-enhanced magnetometry with Bose Einstein condensates,” PhD thesis, Ruperto-Carola-University of Heidelberg, 2014.
- [120] M. F. Riedel, P. Böhi, Y. Li, T. W. Hänsch, A. Sinatra, and P. Treutlein, “Atom-chip-based generation of entanglement for quantum metrology,” *Nature*, vol. 464, pp. 1170–1173, Apr. 2010.
- [121] E. J. Mueller, T.-L. Ho, M. Ueda, and G. Baym, “Fragmentation of Bose Einstein condensates,” *Phys. Rev. A*, vol. 74, p. 033 612, 3 2006.
- [122] J. Wiemer and F. Zhou, “Berry’s phases of ground states of interacting spin-one bosons: Chains of monopoles and monosegments,” *Phys. Rev. B*, vol. 70, p. 115 110, 11 2004.
- [123] A. T. Black, E. Gomez, L. D. Turner, S. Jung, and P. D. Lett, “Spinor dynamics in an antiferromagnetic spin-1 condensate,” *Phys. Rev. Lett.*, vol. 99, p. 070 403, 7 2007.
- [124] C. D. Hamley, C. S. Gerving, T. M. Hoang, E. M. Bookjans, and M. S. Chapman, “Spin-nematic squeezed vacuum in a quantum gas,” *Nature Physics*, vol. 8, pp. 305–308, Apr. 2012. arXiv: 1111.1694 [cond-mat.quant-gas].
- [125] L.-M. Duan, “Entanglement detection in the vicinity of arbitrary dicke states,” *Phys. Rev. Lett.*, vol. 107, p. 180 502, 18 2011.

- [126] G. Vitagliano, I. Apellaniz, M. Kleinmann, B. Lcke, C. Klempt, and G. Tóth, “Entanglement and extreme spin squeezing of unpolarized states,” *New Journal of Physics*, vol. 19, no. 1, p. 013 027, 2017.
- [127] K. Schmüdgen, *The Moment Problem*. Springer, 2017.
- [128] M. Horodecki, P. Horodecki, and R. Horodecki, “Separability of mixed states: Necessary and sufficient conditions,” *Physics Letters A*, vol. 223, no. 1, pp. 1–8, 1996.
- [129] O. Andersson, I. Bengtsson, M. Ericsson, and E. Sjöqvist, “Geometric phases for mixed states of the Kitaev chain,” *Philosophical Transactions of the Royal Society of London Series A*, vol. 374, p. 20 150 231, May 2016. arXiv: 1507 . 00766 [quant-ph].